STARSPOTS AND EXTRA-SOLAR PLANETS

IN LIGHTCURVES & RADIAL VELOCITY MEASUREMENTS

BREAKING NEW GROUND USING PLANETARY DATA

Dissertation
zur Erlangung des Doktorgrades
des Departments Physik
der Universität Hamburg

vorgelegt von

Klaus Felix Huber

aus Weilheim in OB

Hamburg
2010

Gutachter der Dissertation: Prof. Dr. J. H. M. M. Schmitt
Dr. A. Reiners

Gutachter der Disputation: Prof. Dr. P. Hauschildt
Prof. Dr. G. Wiedemann

Datum der Disputation: 30. Juli 2010

Vorsitzender des Prüfungsausschusses: Dr. R. Baade

Vorsitzender des Promotionsausschusses: Prof. Dr. J. Bartels

Dekan der MIN Fakultät: Prof. Dr. H. Graener

Zusammenfassung

Stellare Aktivität und extra-solare Planeten sind zwei besonders lebhafte Gebiete der modernen Astronomie. Beide Themen führen zu fundamentalen Erkenntnissen über die Natur und ihre physikalischen Abläufe – sie tragen sogar zu einer der ältesten Fragen der Menschheit bei: Sind wir allein im Universum?

Neue Instrumente mit unübertroffener Präzision und Langzeit-Beobachtungsprogramme liefern Lichtkurven und Radialgeschwindigkeitsmessungen von Tausenden von Sternsystemen und eröffnen dadurch neue Möglichkeiten für die Forschung. Moderne spektroskopische Geräte erreichen Genauigkeiten von unter 1 m/s in Radialgeschwindigkeitsmessungen und entdecken immer kleinere, nur einige Erdmassen große Planeten. Neue Satelliten, wie CoRoT und Kepler, liefern ununterbrochene, hoch-präzise Photometrie um die Bedeckung von Sternen durch Planeten zu beobachten, von denen einige nicht viel größer sind als unsere eigene Erde.

Diese Daten sind nicht nur für die Entdeckung von Planeten und die Analyse ihrer Eigenschaften nutzbar. Die Lichtkurven und Radialgeschwindigkeitsmessungen beinhalten ebenso die Eigenschaften des Sterns selbst, was eine Vielzahl von neuen Möglichkeiten birgt. Eine davon ist die Analyse von dunklen Bereichen auf der Oberfläche von Sternen, den sogenannten *Sternflecken*.

Diese Doktorarbeit beschäftigt sich mit der Analyse von Signaturen stellarer Aktivität in Daten die in erster Linie aufgenommen wurden, um Planeten zu entdecken. Die Aktivität eines Sterns wird in solchen Daten normalerweise nur als Störung betrachtet und entweder in der Datenanalyse ignoriert oder das Objekt wird als ungeeignet verworfen. In vielen Fällen sind diese beiden Vorgehensweisen nicht empfehlenswert, weshalb die grundlegende Idee dieser Doktorarbeit das Aufzeigen von anderen Herangehensweisen und Möglichkeiten ist.

Zuerst wird der Leser an die Themengebiete Sonnenflecken, Sternflecken und extra-solare Planeten herangeführt. Im zweiten Teil werden die Ergebnisse der Analyse von zwei aktiven Sternen präsentiert. Dopplerbilder des aktiven Sterns V889 Her werden benutzt, um Radialgeschwindigkeiten zu berechnen, die sich auf Grund der Fleckenverteilung ergeben. Ein Vergleich mit beobachteten Radialgeschwindigkeiten zeigt eine gute Übereinstimmung und weist auf Lebenszeiten der dominanten Oberflächenstruktur von über einen Jahr hin.

Die hoch-präzise Lichtkurve des aktiven Sterns CoRoT-2, welcher von einem bedeckenden Planeten umkreist wird, wird verwendet um die Fleckenverteilung zu rekonstruieren. Unter Anwendung der Technik des *planetary eclipse mapping* wird die Fleckenverteilung auf dem Bereich der Sternoberfläche der von dem Planeten überdeckt wird mit hoher Auflösung wiedergewonnen. Zum ersten Mal wird eine *gleichzeitige* Rekonstruktion der Rotationsmodulation und der Bedeckungsprofile durch den Planeten präsentiert, und die daraus gewonnen Helligkeitsverteilungen des überdeckten und des nicht überdeckten Teils der Sternoberfläche werden gezeigt. Mit Hilfe dieser Helligkeitsverteilungen kann die Veränderungen der Sternoberfläche über den gesamten Beobachtungszeitraum von fast einem halben Jahr im Detail verfolgt werden.

Abstract

Stellar activity and extra-solar planets are two especially vivid topics of modern astronomy. Both yield fundamental insights into nature and its physical processes – they even contribute to one of the oldest questions of mankind: Are we alone in the Universe?

New instruments with unprecedented precision and long-term monitoring provide lightcurves and radial velocity measurements of thousands of systems opening up new opportunities for researchers. Modern spectroscopic devices reach radial velocity accuracies of below 1 m/s detecting smaller and smaller planets down to a few Earth masses. New satellites as CoRoT and Kepler obtain continuous high-precision photometry to detect transiting planets as small as our own.

This data is not only valuable for the detection of planets and the analysis of their properties. Lightcurves and radial velocity measurements always contain the properties of the star itself as well, which offers a whole new range of possibilities. One of these is the analysis of dark patches on the surface of stars called *starspots*.

This thesis deals with the analysis of this 'planetary' data concerning stellar activity. The activity of a star is usually merely regarded as additional 'noise' in planet finding observations and is either ignored in the data analysis or the star is not regarded as a suitable target. In many cases both strategies are not recommendable; to demonstrate different approaches and the opportunities within these data sets is the basic idea of this PhD thesis.

First, the reader is introduced to the subjects of sunspots, starspots, and extra-solar planets. Second, the results of the analysis of two active stars are presented. Doppler images of the active star V889 Her are used to model the expected activity-induced radial velocity variations; a comparison to high-precision long-term radial velocity measurements shows good agreement and indicates lifetimes of the dominant surface feature of more than one year.

The spot distribution, and its temporal evolution, is reconstructed from the high-precision lightcurve of the active, planet-hosting star CoRoT-2. The application of *planetary eclipse mapping*, which is the reconstruction of spots from the deformation of planetary transit profiles, results in a detailed reconstruction of the eclipsed surface section of the star. For the first time a *simultaneous* reconstruction of the rotational modulation and the transit profiles is presented, leading to brightness maps for the eclipsed and the noneclipsed stellar surface. Using these maps, the evolution of the spot distribution is traced in detail for almost half a year.

in memoriam

Hans-Joachim Priebe

⋆ 08. März 1942 † 28. April 2007

Contents

I Introduction 11

1 Sunspots 13
- 1.1 Early observations 13
- 1.2 Observational characteristics 15
  - 1.2.1 Cyclic variations 15
  - 1.2.2 Differential rotation 16
  - 1.2.3 Sunspot properties 17
  - 1.2.4 Brightness of sunspots 18
- 1.3 Magnetic field 20
  - 1.3.1 The global magnetic field of the Sun 20
  - 1.3.2 Solar activity 20
  - 1.3.3 Active regions 21
  - 1.3.4 Why are spots cool? 22
- 1.4 Dynamo theory 24
  - 1.4.1 Principles of astrophysical dynamos 24
  - 1.4.2 Basics of MHD 24
  - 1.4.3 Magnetic Reynolds number 25
  - 1.4.4 Producing the toroidal magnetic field 25
  - 1.4.5 Rising flux tubes 26
  - 1.4.6 Sustaining the poloidal field 27
  - 1.4.7 The Babcock-Leighton mechanism 27

2 Starspots 29
- 2.1 Analogy to sunspots 29
  - 2.1.1 Are starspots and sunspots alike? 30
  - 2.1.2 Rapid stellar rotation 30
  - 2.1.3 Spectral type 31
- 2.2 Observation techniques 32
  - 2.2.1 Lightcurves 32
  - 2.2.2 Eclipse mapping 32
  - 2.2.3 Radial velocities 34
  - 2.2.4 Doppler Imaging (DI) 38
- 2.3 Starspot characteristics 39
  - 2.3.1 Sizes 39
  - 2.3.2 Temperatures and brightnesses 40

2.3.3 Polar spots and active belts . . . 41
2.3.4 Lifetimes . . . 41
2.3.5 Stellar differential rotation . . . 42
2.3.6 Active longitudes and flip-flops . . . 43
2.3.7 Butterfly diagrams . . . 43

3 Extra-solar planets 45
3.1 Planets around other stars . . . 45
3.2 What exactly is an exoplanet? . . . 46
3.3 Radial velocity method . . . 47
3.3.1 Detection and confirmation of exoplanets . . . 47
3.3.2 The Rossiter-McLaughlin effect . . . 49
3.4 Transiting planets . . . 50
3.5 How many planets will be found? . . . 52

II Publications 55

4 Overview 57
4.1 Doppler Imaging and RV curves of V889 Her . . . 57
4.2 Transit mapping of CoRoT-2 . . . 57
4.3 Spots in RV measurements . . . 58

5 V889 Herculis 59
Long-term stability of spotted regions and the activity-induced Rossiter-McLaughlin effect on V889 Herculis. A synergy of photometry, radial velocity measurements, and Doppler imaging. . . . 59

6 CoRoT-2 75
6.1 How stellar activity affects the size estimates of extrasolar planets . . . 75
6.2 A planetary eclipse map of CoRoT-2a. Comprehensive lightcurve modeling combining rotational-modulation and transits. . . . 82
6.3 Planetary eclipse mapping of CoRoT-2a. Evolution, differential rotation, and spot migration. . . . 90

III Conclusions 101

7 Summary and outlook 103
7.1 A new era of measurements . . . 103
7.2 Synergetic effects of combining data . . . 104
7.3 Summary . . . 105
7.4 Outlook . . . 106
7.4.1 Starspots . . . 106
7.4.2 Extra-solar planets . . . 108

Part I

Introduction

Chapter 1

Sunspots

"Rosa ursina, oder über die Sonne, die sich dank dem wunderbaren Phänomen ihrer Fackeln und Flecken veränderbar zeigt, und dazu auch im Verlauf eines Jahres längs einer festen Achse von Westen nach Osten um ihren eigenen Mittelpunkt rotiert sowie eine Umdrehung längs einer durch ihre Pole beweglichen Achse von Osten nach Westen in knapp einem Monat absolviert."

Christoph Scheiner, title of the book *Rosa Ursina* (Scheiner 1626)

1.1 Early observations

Our Sun has fascinated mankind since the dawn of history. Even before it was known what exactly the Sun is, it was clear that its light and its behavior in the sky are fundamental to Earth and all its living beings.[a]

Records of studies concerning the Sun date back to several thousand years BC, but comments on the dark structures eventually covering its surface do not date back more than about two millenia.

The oldest observations we know of were carried out by Chinese astronomers in the *Former Han Dynasty* several decades before common era. Most likely they saw a group of very large sunspots, probably covering up to a percent of the solar disk. They also might have benefited from their observation positions: China has plateaus at several thousand meters above sea level with very clear atmospheric conditions.

European references to sunspots do not exist before the Middle Ages. The Benedictine monk Adelmus observed a large spot on the surface of the Sun in the year 807 for eight days, but he misinterpreted it as a transit of Mercury (Wilson 1917). In the 12th century an English monk as well as an Arabic polymath reported on sunspots; however, they did not understand what they were seeing and misinterpreted the phenomenon.

Sunspots are very hard to observe with the naked eye. All observed sunspots must have been extremely large – probably larger than 5 ‰ of the solar disk size. Most of the large spots on the Sun's surface do not reach such dimensions but have sizes of about 1 ‰ or smaller. Thus, a more profound knowledge and understanding of sunspots was not gained before the use of telescopes in astronomy.

---

[a] Nowadays it is known that not all sorts of life depend on light. Some bacteria are capable of *chemosynthesis* using energy sources other than light. Primitive *extremophile* lifeforms can survive in places completely cut off from light. These organisms probably represent the earliest lifeforms on Earth and may be the ancestors of all other living beings.

Johannes Fabricius, and his father David, were the first to publish an observation and a description of starspots using a telescope in the year 1611 (Fabricius 1611). However, for a long time they were not credited for it. In the year 1612 Galileo Galilei and Christoph Scheiner, a German monk, argued on who detected sunspots first. Three letters of Scheiner on solar spots were published in the beginning of 1612 (Scheiner 1612); Galileo wrote several letters in the same year, but had shown sunspots to many people in Rome already in late 1611. His letters were published in early 1613 (Galilei 1613). Figures 1.1 and 1.2 show some examples of the many pictures of sunspots drawn and published by Christoph Scheiner.

One of Galileo's most important contributions to this subject was his understanding of the phenomenon. He interpreted it as spots on the surface of the Sun – which is correct. However, this was not easily accepted because most scholars at that time still believed the Sun had to be a perfect body and was not allowed to have spots. This insight into the nature of sunspots enabled observers to prove that the Sun was indeed rotating, which was suggested some years before by Johannes Kepler.

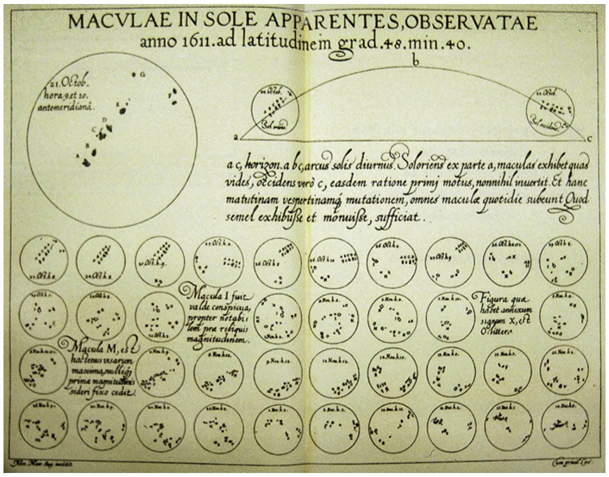
MACVLAE IN SOLE APPARENTES, OBSERVATAE
anno 1611. ad latitudinem grad. 48. min. 40.
b
a
c
a c, horizon, a b c, arcus solis diurnus. Sol oriens ex parte a, maculas exhibet quas vides, occidens verò c, easdem ratione primi motus, nonnihil inuertit. Et hanc matutinam vespertinamq mutationem, omnes maculæ quotidie subeunt. Quod semel exhibuisse et monuisse, sufficiat.

Figure 1.1: Sunspot maps drawn by Scheiner in his book *Tres Epistolae* (Scheiner 1612).

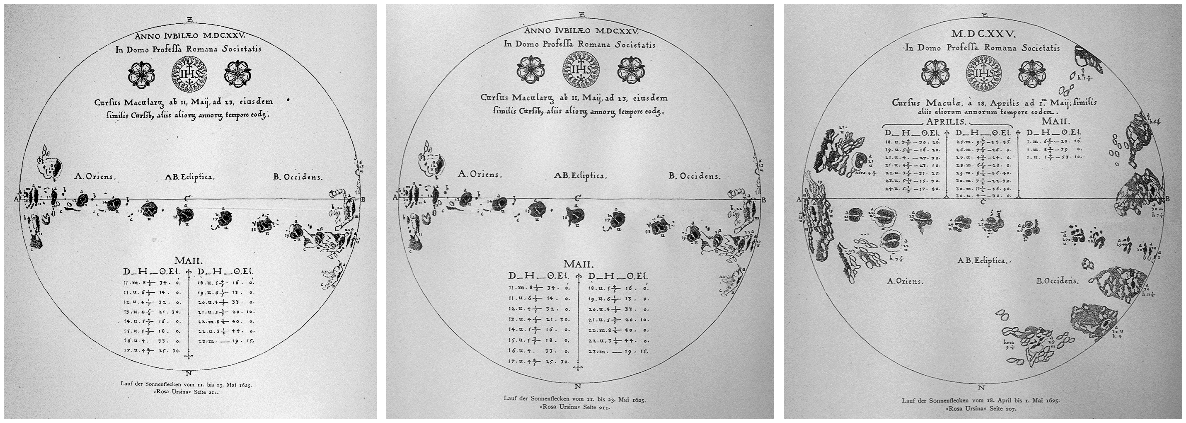
ANNO IVBILÆO M.DCXXV.
In Domo Professa Romana Societatis
A. Oriens
AB. Ecliptica
B. Occidens
MAII
M.DC.XXV.
APRILIS
N

Figure 1.2: Sunspot maps drawn by Scheiner in his book *Rosa Ursina* (Scheiner 1626).

1.2 Observational characteristics

1.2.1 Cyclic variations

In the first half of the 19th century the German astronomer Samuel H. Schwabe noticed that the number of sunspots varies periodically. This *solar cycle* or *spot cycle* shows clear maxima, with a high number of spots on the surface, and pronounced minima with very few spots – sometimes even none during periods of days or weeks.

A careful analysis of all available records, which stretch back to the 17th century, suggests an average length of about 11 years for one cycle, which is the time between two subsequent maxima or minima. This behavior is not very stable: the periods of individual cycles can vary by years and also the strengths of maxima and minima are changing. A period at the end of the 17th century is called the *Maunder Minimum* (Eddy et al. 1976), which is known for its low number of spots during more than 50 years.

Another interesting fact associated with the solar cycle is the change in spot positions. At solar minimum most of the spots emerge very close to the Sun's equator. When the number of spots increases again, most of them appear at higher latitudes, which is closer to the poles. This can be seen nicely in Fig. 1.3, which has often been referred to as the *butterfly diagram* of the Sun. It is striking that there are hardly any spots outside the latitudinal band of ± 40° around the equator.

We know now that the total solar irradiance varies along with the cycle of the Sun, although the amplitude of this variation is small ($\sim 1‰$, see Fig. 1.6). The Sun emits more energy at solar maximum, when many spots cover its surface, which is at first glance unexpected. Why should the Sun emit more light when it has the most dark spots?

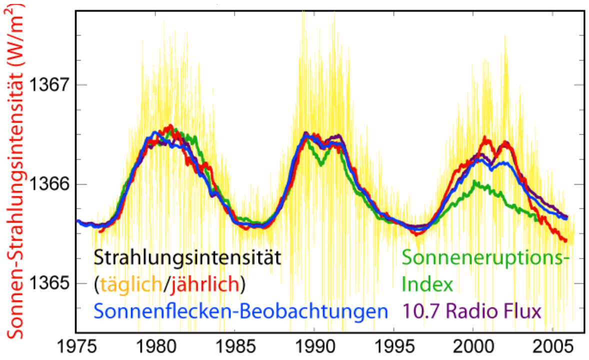

Figure 1.6: Variations of the total irradiance of the Sun (black curve). The electromagnetic radiation per unit area W/m^2 is given over years. This picture is part of the public domain.

Along with spots the surface of the Sun is covered with *faculae* – small but very bright regions on the surface. The more sunspots appear, the more bright regions can be ob-

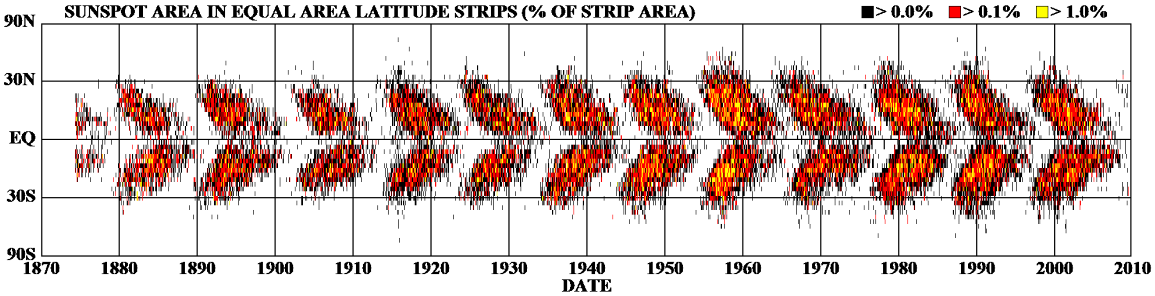

Figure 1.3: Butterfly diagram of the Sun. The vertical axis gives the latitude of the spots. Larger spots have lighter color. This picture is part of the *public domain.*

served on the surface. This is the reason for the increased total solar flux; the energy output prevented by the existence of spots is more than compensated by the appearance of bright structures. Sunspots and bright regions, especially faculae, seem to have a close connection.

1.2.2 Differential rotation

Sunspots were used to determine the solar rotation period right after the first observations with telescopes. Soon it was clear that the Sun revolved around its axis once about every month. However, careful observations showed that the Sun does not rotate like a rigid body but has a *differential rotation*. This was detected by R. C. Carrington and published in two papers (Carrington 1858, 1859).

Spots located at different latitudes have different rotation periods. Close to the equator the rotation period is approximately 25 days, at polar regions it can be as large as 36 days (Beck 2000). Thus, the solar surface rotates faster at low latitudes. These periods change to larger values if the rotation of the Sun is not measured with spots (*tracer measurements*) but with Doppler shifts of spectral lines (*spectroscopic measurements*) instead. The latter yields the rotation of the plasma at the surface whereas spots are 'anchored' to lower layers. This is direct evidence for a faster rotation inside of the Sun than on its surface.

Differential rotation is commonly described by the formula

$$\Omega_{\mathrm{rot}}(\phi) = A + B \sin^2 \phi + C \sin^4 \phi . \quad (1.1)$$

Quantity A represents the equatorial rotation rate, B and C are the differential rotation rates, and ϕ is the latitude. Equation 1.1 indicates that the law of differential rotation is best fitted using even powers of $\sin \phi$. Some measurements do not require a $\sin^4 \phi$ term, which means $C = 0$.

Beck (2000) presented an extensive overview on measurements of the solar differential rotation. The different results for tracer and spectroscopic measurements are shown in Fig. 1.5. Differential rotation significantly depends on factors as size and age of spots or scattered light corrections. Therefore it is hard to give precise values for

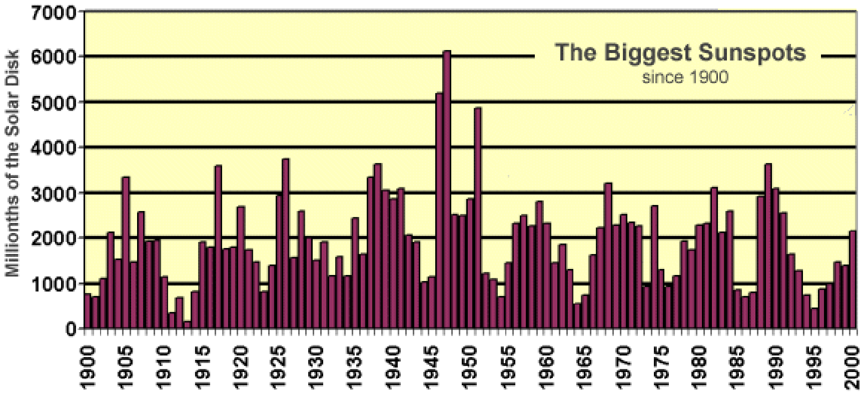

Figure 1.4: The biggest sunspots observed in the 20th century. Spot sizes are often measured by their area compared to the total area of the solar disk, which is the unit of the vertical axis. The largest spot was observed in the year 1947. This picture was taken from `http://spaceweather.com/sunspots/history.html`.

A, B, and C. Snodgrass & Ulrich (1990) determine the values

$$A = 2.85 \ , \ B = -0.34 \ , \ C = -0.47$$

in units of μrad/s from Doppler features in the photosphere, which is equivalent to equatorial (e) and polar (p) rotation periods of

$$P_{\rm e} = 25.5 \ d \ , \ P_{\rm p} = 35.7 \ d \ .$$

Zappala & Zuccarello (1991) derive different values for young and recurring spots. Averaging their results, they determine values of

$$A = 2.9 \ , \ B = -0.5$$

in units of μrad/s so that

$$P_{\rm e} = 25.1 \ d \ , \ P_{\rm p} = 30.3 \ d \ .$$

Since differential rotation plays an important role for the dynamo process of stars, for the outer convection zone, and for evolution of spot distributions, this topic is further discussed in Sect. 2.3.5.

1.2.3 Sunspot properties

The exact properties of sunspots – their size, temperature, migration, evolution, etc. – are still difficult to observe and to analyze. Observations of small or dark objects against the bright solar disk are always difficult. At the limb of the disk the projected area of sunspots is small, which makes them even harder to see.[b] Often it is complicated to discriminate between individual spots when they appear in close groups, which is the case quite frequently.

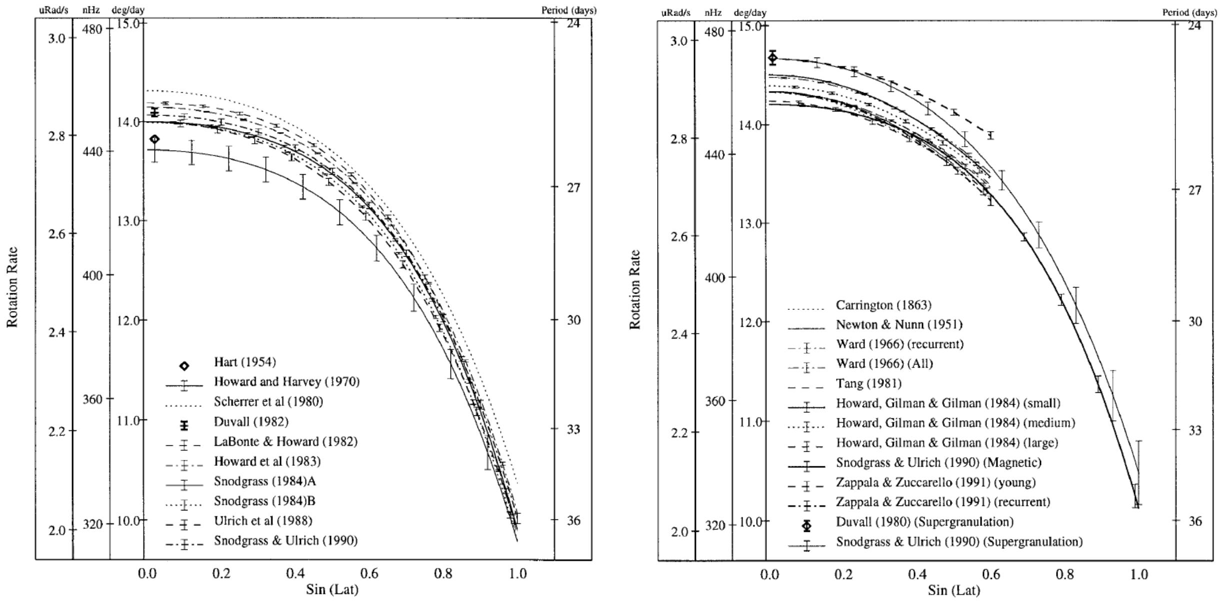

Figure 1.5: Solar differential rotation from Beck (2000). *Left panel:* Different measurements using the Doppler shift of photospheric spectral lines. *Right panel:* Different measurements using tracers (sunspots, magnetograms, supergranules).

---

[b] This problem is enhanced by the *Wilson depression*, which is e.g. illustrated in Bray & Loughhead (1964). It is a geometric effect caused by the 'deeper' location of the spot within the photosphere. For a spot on the solar limb, the penumbra on the side towards the disk center appears smaller than the penumbra located closer to the limb.

The structure of spots is far more complex than just a round, uniformly dark area. The inner core and darkest part of a sunspot is called *umbra*. The umbra is surrounded by an outer region called *penumbra*: it is brighter, can be very irregular, and is sometimes shared between individual spots.

Spots are darker than the regular photosphere – which is the ‘surface’ of the Sun emitting the visible light – because they are cooler. The *effective* temperature of the Sun is about 5 800 K (Kurucz 1992). Typically, the umbra is 1 000 – 1 900 K cooler, the penumbra only 250 – 400 K (Solanki 2003).

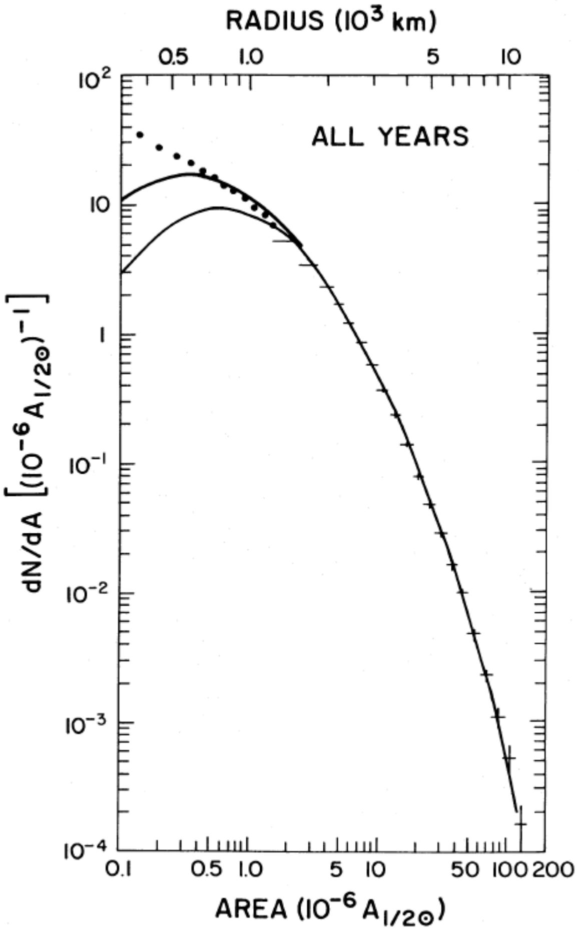

Figure 1.7: Size distribution of a total number of 24 615 sunspots taken from Bogdan et al. (1988). Smaller spots are much more frequent than larger ones

The distribution of sizes is complex. Small spots appear in much higher numbers than large ones. Figure 1.7 shows the distribution of sizes for a total number of 24 615 spots observed over a period of 75 years (Bogdan et al. 1988). The number of larger spots exponentially decreases. The smallest spots observed on the Sun are approximately 3 500 km in diameter (Bray & Loughhead 1964), which is equivalent to an area of about 0.006 ‰ of the solar disk. Smaller spots, called pores, do not have penumbrae anymore and have sizes down to the resolution limit. The largest sunspot area of roughly 6 ‰ of the solar disk was measured in 1947 and represents the most extreme case observed so far (see Fig. 1.4).

As soon as sunspots have formed, which takes only a few hours, they decay (Solanki 2003). Their lifetimes span from hours to months and depend on the size of the spot. A linear decay law, which was first suggested by Gnevyshev (1938), is apparently a good approximation, although this is still under debate. The majority of spots is small and, thus, most spots have short lifetimes. The measurement of long lifetimes ($\gtrsim$ 10 d) is difficult because continuous observations are hardly possible.

Lifetimes of sunspots can be estimated using the Gnevyshev-Waldmeier rule

$$t = \frac{A_0}{W} \tag{1.2}$$

first formulated by Waldmeier (1955); t is the lifetime, A_0 the maximum spot size, and $W = (10.89 \pm 0.18)$ (Petrovay & van Driel-Gesztelyi 1997) in units of 10^{-6} solar hemispheres per day.

1.2.4 Brightness of sunspots

The brightness of sunspots is of high significance for the main topic of this work, namely starspots. It is important to know how much energy is emitted by a sunspot compared to the undisturbed photosphere.

The *total sunspot contrast* is defined as

$$\alpha = 1 - \frac{I_{\mathrm{s}}}{I_{\mathrm{ph}}} ,$$

where I_{s} is the sunspot intensity integrated over all wavelengths and I_{ph} is the same value for the undisturbed photosphere. Beck & Chapman (1993) rewrite this formula to account for the effects of umbral A_u and penumbral areas A_p (with $A_s = A_u + A_p$).

$$\alpha = \frac{A_{\mathrm{u}}}{A_{\mathrm{s}}} \left[1 - \frac{T_{\mathrm{u}}^4}{T_{\mathrm{ph}}^4} \right] + \frac{A_{\mathrm{p}}}{A_{\mathrm{s}}} \left[1 - \frac{T_{\mathrm{p}}^4}{T_{\mathrm{ph}}^4} \right]$$

The quantities T_{u}, T_{p}, and T_{ph} are the effective temperatures of the umbra, penumbra, and photosphere. The authors find an umbra to penumbra area ratio of $A_{\mathrm{u}}/A_{\mathrm{p}} = 0.25$ resulting in $\alpha = 0.3$ (also confirmed by Chapman et al. 1994).

The brightness of the spot is defined as

$$\mathrm{b} = \frac{I_{\mathrm{s}}}{I_{\mathrm{ph}}} = \frac{T_{\mathrm{s}}^4}{T_{\mathrm{ph}}^4} = 1 - \alpha .$$

Using their result for α, the average brightness of sunspots is 0.7.[c] This means our Sun would only emit 70 % of its energy if it was entirely covered with spots. If this value was true for all spots, a decrease of the total solar flux caused by a sunspot could be used to immediately calculate its size.

Unfortunately, the quantity α is only an approximation and depends on the size of the spot and on the ratio between the umbral and penumbral area. While α can also be used to calculate the temperature of a spot, the resulting values are naturally at least as uncertain as α itself.

---

[c] In this case T_{s} is neither the umbral nor the penumbral temperature but the *average* temperature of the entire spot. Using only the umbral temperature $T_{\mathrm{s}} = 4300$ K, the brightness decreases significantly to $\mathrm{b} = 0.3$. The difference in brightness to an average spot results from the much larger fraction of the spot that is covered by the penumbra; on average only 20 % are covered by the umbra.

1.3 Magnetic field

The physical reason for the existence of spots is closely related to the Sun's magnetic field. Hale (1908) was the first to detect the strong magnetization of sunspots and determined field strengths of 2 000 to 3 000 G. The stronger the magnetic field, the cooler the spot.

1.3.1 The global magnetic field of the Sun

The Sun has a dipolar magnetic field which dramatically changes over periods of years. It is commonly accepted that the Sun's magnetic field is generated by a *dynamo effect* (see Sect. 1.4), although its exact operation is still not known. Moving hot, ionized gas within the Sun generates electric currents, which then again generate magnetic fields. The field lines are locked to the gas which is moving and flowing in various ways. Thus, the field lines get stretched, bent, twisted, and folded within the Sun, but get also dragged out onto the surface and into the space beyond. Strong magnetic fields penetrating the surface cause spots (Fig. 1.8, upper panel). Above the photosphere the situation changes: the magnetic field dominates the gas and ionized particles move along the field lines (Fig. 1.8, lower panel).

The configuration of the magnetic field, although bipolar on a global scale, is very complex in detail. Lines and loops anchored to the surface can be seen in many pictures, like, e.g., from the *Solar and Heliospheric Observatory* (SOHO). The two pictures of Fig. 1.8 vividly illustrate the field complexity; one shows the largest sunspot group observed with SOHO so far, the other shows a large magnetic loop, where field lines trap hot plasma. The plasma emits light and, thus, is well visible.

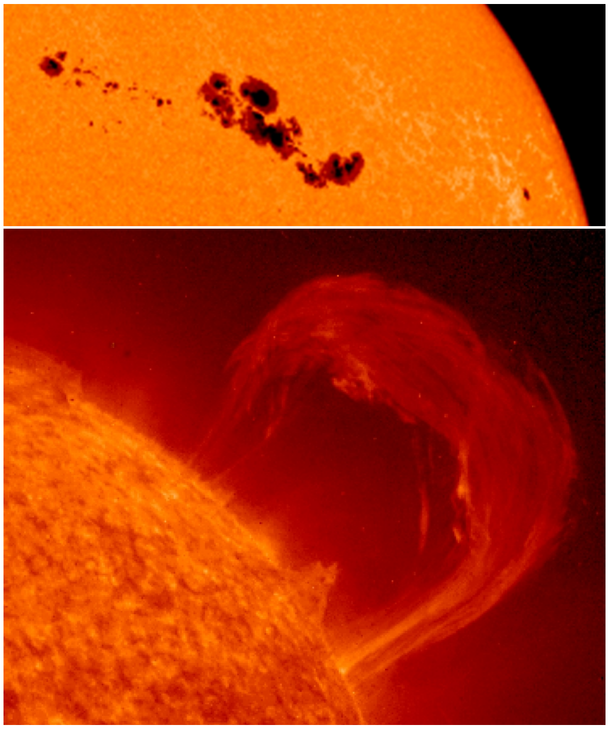

Figure 1.8: *Upper panel:* Largest group of sunspots yet observed with SOHO in March 2001. *Lower panel:* Huge loop of plasma caught in magnetic field lines. This prominence was observed at 14th September, 1999. Both pictures are taken from the SOHO homepage at `http://sohowww.nascom.nasa.gov/gallery/bestofsoho.html`.

The polarity of the magnetic poles switches with a cyclic behavior connected to the solar cycle. In approximately 22 years the poles change from one polarization to the other and back again. This is exactly twice the period measured for the sunspot cycle. Along with it, the polarity of the spots changes as well. This behavior can be seen in Fig. 1.12.

1.3.2 Solar activity

Figure 1.8 gives two examples of phenomena commonly summed up under the expression *activity*. Although a general definition of this term is not possible, both phenomena are clearly related to the magnetic field.

Solar activity is the behavior of the Sun that cannot be explained by 'classical' models – when the Sun 'misbehaves' (Linsky 2007). It is mostly connected to the magnetic field and processes therein, and to non-radiative heating processes. In analogy the term *stellar activity* is used when the assumptions of classical stellar atmospheres are not valid anymore.

In this work the term activity is mainly used for surface spots with lower temperature than the undisturbed photosphere.

1.3.3 Active regions

Sunspots are always associated with active regions, regions on the surface with high magnetic activity where spots frequently appear and decay. These regions are much larger and more persistent than individual spots. The entire active region is pierced with field lines and spots form at their densest concentrations.

Within these active regions a number of spots can appear at the same time. These *spot groups* usually belong together although often they are clearly separated. An idea to explain this is that associated magnetic field lines split up below the surface and form several small spots.

However, different spots in the same active region can have opposite magnetic polarizations. This is caused by loops of field lines going outwards and inwards through the surface. These two associated poles can be very close and are referred to as *bipolar spots*. Figure 1.9 gives an example of several bipolar spots.

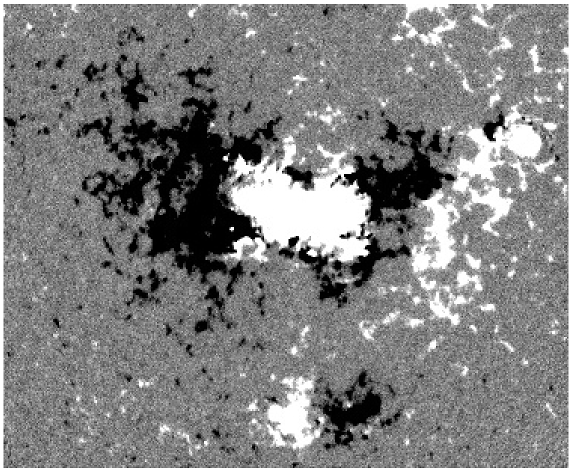

Figure 1.9: Magnetogram of the solar surface observed with the Michelson Doppler Imager on board of the SOHO satellite. The black and white structures show magnetic fields with opposite polarization. The picture is taken from the SOHO homepage at `http://sohowww.nascom.nasa.gov/gallery/bestofsoho.html`.

Joy's law

Bipolar spots usually have a leading and a following spot relative to the rotation. Hale et al. (1919) noticed that the line connecting the centers of bipolar spots is on average tilted with respect to the equator. This behavior is called *Joy's law*. Measurements of this tilt are presented in Fig. 1.10 (Howard 1991). Furthermore, this tilt increases with latitude, which can be seen in Fig. 1.11. The leading spot is usually closer to the equator than the following spot, and on the two hemispheres the bipolar spots have opposite polarities.

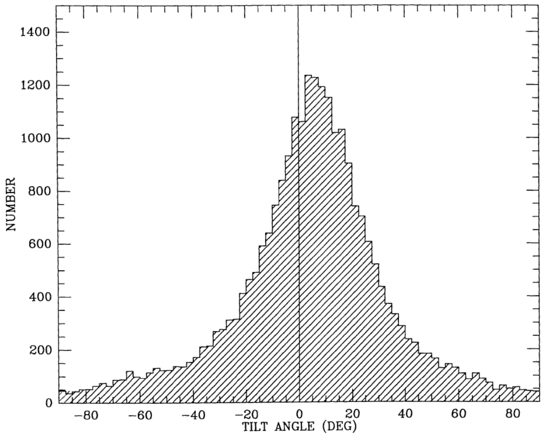

Figure 1.10: Tilt angle of bipolar spots on the Sun (Howard 1991). Shown is the angle between the line connecting the centers of the bipolar spot and the equator.

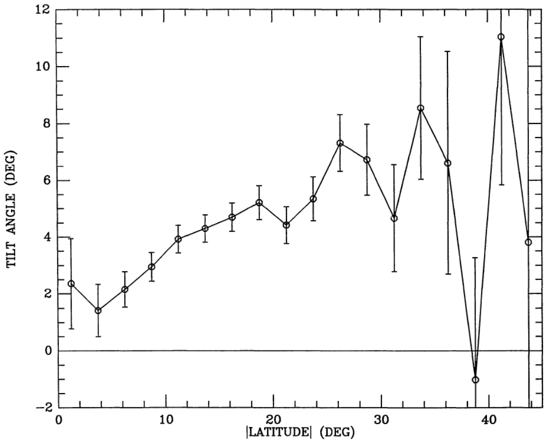

Figure 1.11: Tilt angle of bipolar spots on the Sun versus latitude (Howard 1991). Low-latitude spots have smaller tilts than spots closer to the poles.

1.3.4 Why are spots cool?

Deep inside the Sun energy is transported by radiation. In the outer region of the Sun this transportation mechanism changes to convection: hot cells of plasma are rising to the surface, cool radiatively, and sink down again. The photosphere is the top layer of the Sun's convection zone. The granulation we see, when we take a close look at the photosphere, results from these rising and falling cells of plasma. Emission from the photosphere is the light we see. Thus, this layer of the Sun's atmosphere is commonly defined as its surface.

Magnetic fields inside the Sun are bound to the charged particles of the plasma. Thus, they can retard the movement of plasma in the convection zone. Strong magnetic fields, which are found in sunspots, prevent hot plasma from rising to the surface. Because the energy transportation mechanism is blocked, this area of the photosphere cools down.

The field strength within sunspots reaches from peak values of 2 000 – 3 700 G at the core to 700 – 1 000 G at the edge (Solanki 2003). The field lines are close to vertical in the umbra but get strongly tilted in the penumbra. This is the reason for the temperature difference between umbra and penumbra: the rising of hot plasma is much stronger suppressed in the umbra because the field strength is higher.

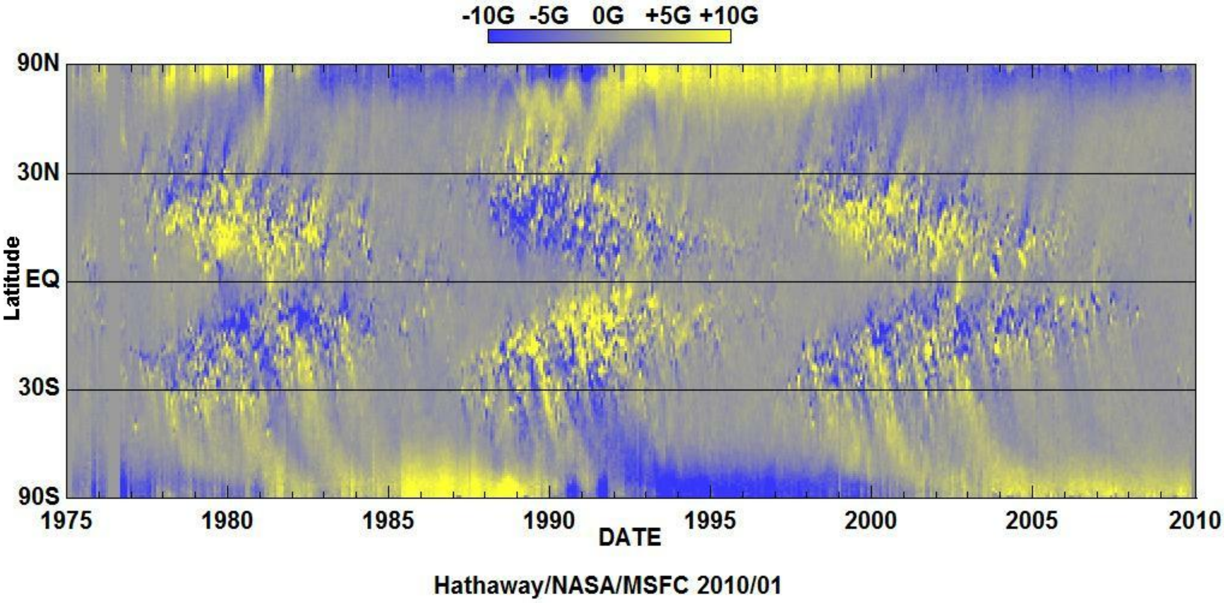

Figure 1.12: The magnetic butterfly diagram of the Sun. The field strength is color coded, blue and yellow colors indicate the two different polarities of the magnetic field. Every solar cycle the polarity of the poles switches. The polarity of neighboring spots can be opposite. This picture was taken from `http://solarscience.msfc.nasa.gov/dynamo.shtml`.

1.4 Dynamo theory

The dynamo theory explains how astronomical bodies generate their magnetic field based on *magnetohydrodynamics* (MHD). Thus, this process is often called a *hydromagnetic dynamo*. This section presents the basic ideas along with some important equations to introduce the reader to the dynamo theory. It is primarily based on Choudhuri (2007), Choudhuri (1998), and Mestel (1999). Especially Choudhuri (2007) manages to reveal the simplicity of the general ideas of the dynamo theory, which is often lost in the formalism of MHD. I will try to follow this example in my overview.

1.4.1 Principles of astrophysical dynamos

Ordinary dynamos work by Faraday's law of *electromagnetic induction*. A conducting wire is moving inside a magnetic field generating an *electromotive force* (EMF).

There are no wires in a star. Nevertheless, stars consist of plasma which is conducting matter, and stars rotate. If a certain volume of plasma is moving through a magnetic field, an EMF can be induced which can reinforce the magnetic field.

Where does the initial magnetic *seed field* come from, in which the plasma is moving? Stars are made from interstellar clouds containing magnetic fields. When these clouds gravitationally collapse, the magnetic field is dragged along with the gas into the forming star. This initial seed field is sustained – and changed – by the dynamo process.

1.4.2 Basics of MHD

Magnetohydrodynamics (MHD) combines Maxwell's equations

$$\vec{\nabla} \cdot \vec{E} = 4\pi\rho \tag{1.3}$$

$$\vec{\nabla} \cdot \vec{B} = 0 \tag{1.4}$$

$$\vec{\nabla} \times \vec{E} = -\frac{1}{c}\frac{\partial}{\partial t}\vec{B} \tag{1.5}$$

$$\vec{\nabla} \times \vec{B} = \frac{4\pi}{c}\vec{j} + \frac{1}{c}\frac{\partial}{\partial t}\vec{E} \ , \tag{1.6}$$

the continuity equation (mass conservation)

$$\frac{\partial}{\partial t}\rho + \vec{\nabla}\left(\rho\vec{v}\right) = 0 \ , \tag{1.7}$$

and the equation

$$\frac{\partial}{\partial t}\vec{v} + \left(\vec{v} \cdot \vec{\nabla}\right)\vec{v} = -\frac{1}{\rho}\vec{\nabla}\left(\vec{p} + \frac{B^2}{8\pi}\right) + \frac{\left(\vec{B} \cdot \vec{\nabla}\right)\vec{B}}{4\pi\rho} + \vec{g} \tag{1.8}$$

which is basically the Euler equation of fluid mechanics including magnetic forces and gravity. The different variables are: electric field $\vec{E}$, magnetic field $\vec{B}$, velocity field $\vec{v}$, (charge) density ρ, current density $\vec{j}$, pressure $\vec{p}$, speed of light c, and gravitational field $\vec{g}$.[d]

Equation 1.8 clearly shows the additional effects of the magnetic field for fluid dynamics: it introduces an additional pressure $B^2/8\pi$ and a 'magnetic tension' $(\vec{B} \cdot \vec{\nabla})\vec{B}/4\pi\rho$ along the field lines.

The key equation in MHD is the *induction equation*

$$\frac{\partial}{\partial t}\vec{B} = \vec{\nabla} \times \left(\vec{v} \times \vec{B}\right) + \lambda\nabla^2\vec{B} \tag{1.9}$$

---

[d] A distinction between *charge density* and *density* is not necessary here because the solar matter consists of highly ionized plasma. At approximately 1 000 km below the photosphere the temperature rises above 10 000 K and hydrogen is ionized. Thus, most of the solar matter consists of charged particles and both densities can be set equal.

deduced from Maxwell's equations and Ohm's law, which is

$$\frac{\vec{j}}{\sigma} = \vec{E}' = \vec{E} + \frac{1}{c}\vec{v} \times \vec{B} \ . \tag{1.10}$$

$\vec{E}'$ is the electric field in the co-moving frame. Using the truncated Ampère-Maxwell law

$$\vec{j} = \frac{c}{4\pi}\vec{\nabla} \times \vec{B} \ , \tag{1.11}$$

we can re-write the equation $\vec{\nabla}\times$ 1.10 as

$$\vec{\nabla} \times \left(\lambda \vec{\nabla} \times \vec{B}\right) = -\frac{\partial}{\partial t}\vec{B} + \vec{\nabla} \times \left(\vec{v} \times \vec{B}\right) \ . \tag{1.12}$$

This is exactly Eq. 1.9 if the resistivity of the magnetic diffusion

$$\lambda = \frac{c^2}{4\pi\sigma} \tag{1.13}$$

is constant. σ is the electrical conductivity. The term $\lambda\nabla^2\vec{B}$ gives the *diffusion* of the magnetic field. Equations 1.8 and 1.9 are the two basic equations of MHD.

1.4.3 Magnetic Reynolds number

Plasmas in laboratories and on astrophysical scales are quite different. This can be easily seen using the *magnetic Reynolds number R_m*. The terms on the right-hand side of Eq. 1.9 are approximately vB/l and $\lambda B/l^2$, if l is a typical length scale of the system. Their ratio is

$$R_m = \frac{vB}{l} \cdot \frac{l^2}{\lambda B} = \frac{v}{\lambda} \cdot l \ . \tag{1.14}$$

For $R_m \gg 1$ the diffusion term of Eq. 1.9 is negligible and magnetic fields are frozen to the plasma; the field is dragged along with the moving matter.[e] Alfvén (1943) first noticed this phenomenon commonly called *flux-freezing.*

In laboratories R_m is typically much smaller than one because l is very small. However, on astrophysical scales we easily find values of $R_m \gg 1$. This is one reason why bodies like the Sun can have self-sustaining magnetic fields.

1.4.4 Producing the toroidal magnetic field

Assume our model dynamo process starts with plasma moving in an initial magnetic seed field. This field is poloidal, meaning the field lines are approximately parallel running from one magnetic pole to the other. Because of the Sun's differential rotation, plasma is rotating faster at the equator than at the poles. The magnetic field lines are attached to the plasma stretching the lines and shifting their orientation parallel to the equator. This way the poloidal field is converted into a toroidal field. A sketch illustrating this process is presented in Fig. 1.13. The picture also illustrates why the toroidal field has opposite polarity in the two hemispheres.

Although there is differential rotation in the solar photosphere, helioseismology has shown that its gradient is strongest inside the Sun. The layer between the radiative core and the convective outer layer is called

---

[e] This is true for the convection zone. However, in the outer atmospheres the magnetic field dominates the plasma. Charged particles are forced to follow the field lines, which is well visible in Fig. 1.8 (lower panel). The main reason for this is the strong decrease in plasma density between the convection zone and higher atmospheric layers.

tachocline. There the toroidal field is expected to be generated. Figure 1.14 shows the interior rotation rate of the Sun derived from helioseismology.

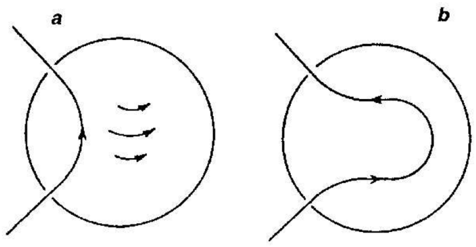

Figure 1.13: Sketch of the transformation of the poloidal magnetic field (panel a) to the toroidal field (panel b) by differential rotation (Choudhuri 2007). This mechanism is called the Ω-effect in dynamo theory.

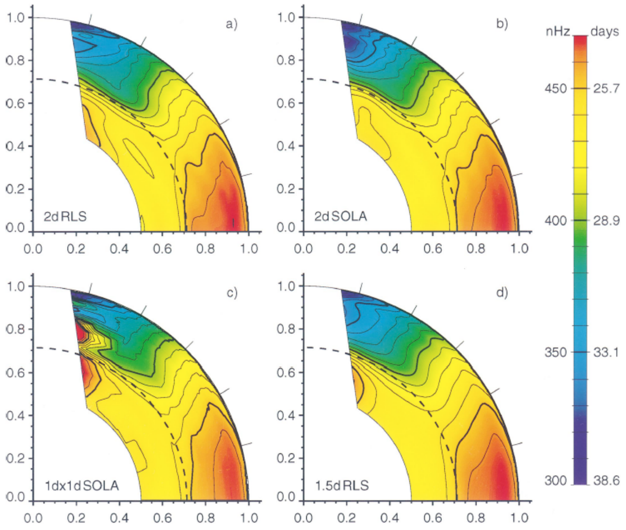

Figure 1.14: Interior rotation rate of the Sun over radius and latitude (Schou et al. 1998). Shown are solutions for four different inversion methods of the used helioseismic data. The dashed line indicates the position of the tachocline.

1.4.5 Rising flux tubes

The toroidal field is produced at the bottom of the convection zone. To understand why (bipolar) spots are visible at the photosphere, we need to have a process moving the field lines upwards to the surface *and* concentrating them in certain regions. This is realized by the interaction between convection and the magnetic field.

Magnetic buoyancy

The toroidal magnetic field beneath the convection zone starts to rise because of the pressure term $B^2/8\pi$ in Eq. 1.8. The gas pressure inside p_i and outside p_o of a flux tube must be in equilibrium

$$p_o = p_i + \frac{B^2}{8\pi} \; .$$

Consequently, $p_o \geq p_i$ leads to a rising flux tube due to buoyancy, if the pressure difference results from lower gas densities inside than outside of the flux tube. This idea was first presented in Parker (1955b). Figure 1.15 (panel a) illustrates the rise of the magnetic field lines due to buoyancy.

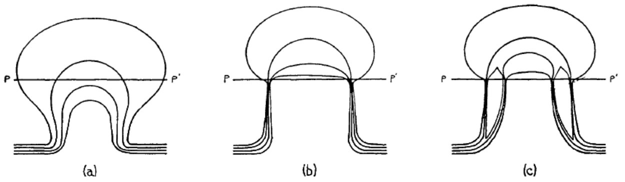

Figure 1.15: Sketch from Parker (1955b) showing the toroidal magnetic field lines rising in the convection zone and penetrating the surface. *Panel a:* Magnetic buoyancy. *Panel b:* Concentration of field lines. *Panel c:* Splitting of flux tubes.

Magnetic field strength

To estimate the strength of the magnetic field at the tachocline, the magnetic and the kinetic (convection) energy density were assumed to be approximately equal. This suggests a magnetic field strength of $B \approx 10^4$ G. However, numerical models show that this is not sufficient for magnetic flux tubes to rise due to magnetic buoyancy. Only with fields as strong as $B \approx 10^5$ G buoyancy dominates and flux tubes rise towards low latitudes. Otherwise, the Coriolis force drives the flux tubes to very high latitudes before they appear at the surface – which is obviously not observed on the Sun.

Field line concentration

At first it is not intuitively clear why the magnetic field is not evenly distributed in the convective zone. When Weiss (1981) presented numerical simulations of *magnetoconvection*, it became clear that convection cells exclude the magnetic field lines, which had been suggested before. In this process the field lines are compressed in specific regions between the larger cells where they suppress the convection. Thus, the magnetic field penetrates the convection zone along densely packed paths. These flux tubes are seen as spots on the surface of the convection zone.

An illustration of this process is given in Fig. 1.15 (panels b and c). In panel (b) a flux tube emerges from the outer layers and plunges back into it at two different positions generating spots with opposite polarities. Panel (c) shows the splitting of the flux tubes which results in active regions with several spots of different polarities.

1.4.6 Sustaining the poloidal field

The poloidal field is constantly converted into the toroidal field by differential rotation. This is called the Ω-effect. But how is the poloidal field regenerated?

The velocity field $\vec{v}$ of Eqs. 1.8 and 1.9 has to sustain the magnetic field. The question ‘Which velocity field sustains a magnetic field?’ is known as the *kinematic dynamo problem.* Cowling (1934) discovered that there is no axisymmetric solution to this problem, which was a first important step to restrict the space of possible solutions.

It was noticed by Parker (1955a) that turbulent velocity fields in the convection zone – which are non-axisymmetric – can sustain the magnetic field. Hot matter rising in the convection zone rotates because of the Coriolis force. This also twists the rising field lines frozen to the plasma. Figure 1.16 gives an illustration of the twisting of uprising field lines. This is called the α-effect.

The rising toroidal field lines get twisted and form magnetic loops along the poloidal field. In combination with turbulent diffusion, these loops form a large-scale poloidal magnetic field. This way the toroidal field is again converted back to poloidal. The entire circle of magnetic field conversion is called the $\alpha\Omega$-dynamo.

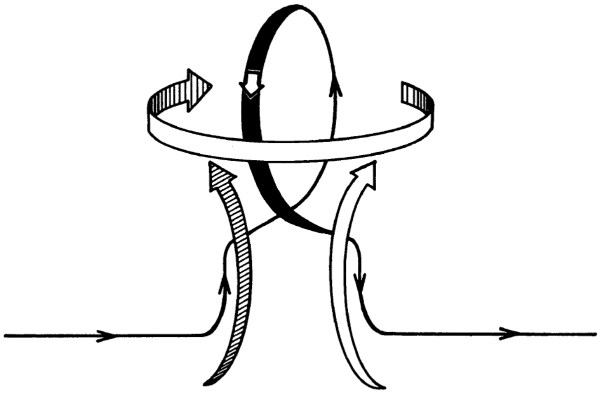

Figure 1.16: Illustration of the α-effect (Parker 1970). Uprising (toroidal) flux tubes get twisted by the Coriolis force and build up the poloidal magnetic field.

1.4.7 The Babcock-Leighton mechanism

It should be noticed that although the previously presented model for the dynamo represents a good explanation it is probably not absolutely correct. For magnetic field strengths of $B \approx 10^5$ G the Coriolis force twisting the rising flux tubes is not strong enough to produce the required poloidal field.

Babcock (1961) and Leighton (1969) introduced an alternative explanation which was adopted to explain the generation of a poloidal field despite the problems of twisting it. A detailed explanation goes beyond the scope of this work, but the essence of it is that still a poloidal field can be generated by the (turbulent) diffusion of slightly tilted bipolar spots.

Chapter 2

Starspots

> *“ The peculiar variation in the accompanying light-curve can be explained on the hypothesis that the surface of the G5 star has upon it huge light and dark patches. [...] The patches must be of such size that a projected hemisphere at times has as much as 20 percent of its area covered, while individual patches cover as much as 3 to 5 percent of the area. The data not only indicate that the patches are eclipsed by the K0 star, but that they move, and that they form and dissolve. Furthermore, they appear and disappear around the limb, with rotation of the binary. Clearly, the phenomena are exceedingly complicated, and difficult to analyze precisely, particularly in in view of the unfavorable period of rotation of the binary. ”*
>
> **Gerald E. Kron**
> **Excerpt from his paper *The probable detection of patches of varying brightness on AR Lacertae B***
> **(Kron 1947)**

2.1 Analogy to sunspots

It is evident to extrapolate from the observations of sunspots to the existence of spots on other stars, called *starspots*. The idea that variable stars could be covered with darker regions is rather old.[a] However, Gerald E. Kron was a pioneer in applying this analogy to lightcurves of stars, and interpreting their variations due to the rotation of the spotted star and the evolution of the surface distribution (Kron 1947). He analyzed data of the eclipsing binary system AR Lacertae and noticed that the variations in the lightcurve can be explained with dark and light patches on the surface of the G5 star (see quote at the beginning of this chapter). Furthermore, Kron noticed that the K0 companion eclipses these patches on its way across the disk of the G5 star and deforms the eclipse profile in the lightcurve. This technique is now referred to as *eclipse mapping*, especially for the application to planets it is sometimes also called *transit mapping* or *planetary eclipse mapping.*

---

[a] For example, already 1783 the British amateur astronomer John Goodricke proposed that brightness variability in stars, in particular the star Algol, might be cause either by bodies passing in front of the star or by darker regions periodically turned towards the Earth.

2.1.1 Are starspots and sunspots alike?

Already this example of Kron (1947) shows that starspots can be very different from sunspots. The author mentioned that occasionally up to 20 % of the stellar disk is covered with spots and individual spots cover 3 to 5 %.

This is an order of magnitude more than observed on the Sun, even for the largest sunspots ever seen. In fact, if these spots had not been as large, there would have been no chance to detect them in the first place; the precisions in photometric measurements to detect starspots the size of typical sunspots ($\lesssim$ 1 ‰) were not developed until the beginning of the 21st century.

What is the reason for this huge difference between sunspots and starspots? An honest answer to this question is: we still do not know exactly. Of course there is no reason to believe that there are no other stars showing spots similar to the Sun. However, the variety of starspots and stellar activity is enormous. Even though a star might be similar to the Sun in many respects, e.g. its stellar type, this does not mean it shows the same activity and spots.

The only thing we really know is that the properties of spots and their behavior are dominated by the magnetic field of a star. Therefore, starspots tell us a lot about stellar magnetic fields. To understand spots, we have to understand how the formation of magnetic fields takes place.

2.1.2 Rapid stellar rotation

The vast majority of stars with detected spots rotate much faster than the Sun. Although this result is heavily biased by our observation techniques – it is much easier to detect spots on rapidly rotating stars – it nonetheless shows that many fast rotators have large spots and are very active. This reflects a relation between the rotation velocity and the magnetic activity of stars that has long been studied: the *activity-rotation relation*.

Qualitatively, this relation states that the faster a star rotates, the more active it is. A higher activity means higher magnetic flux and, therefore, more and larger spots.

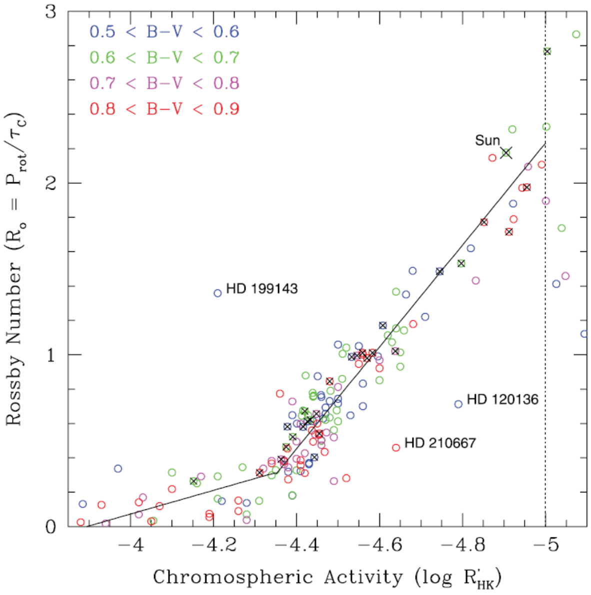

Figure 2.1: Activity-rotation relation from chromospheric emission (Mamajek & Hillenbrand 2008). A larger CaII H and K emission index R_{HK} indicates higher chromospheric activity. A smaller Rossby Number R_0 indicates shorter rotation periods of the star. The data show the clear increase of activity with faster rotation.

This relation is usually not studied using spots but other proxies of stellar activity such as chromospheric or coronal emission (Figs. 2.1 and 2.2). A detailed discussion of the activity-rotation relation is beyond the scope of this introduction; some informative publications are e.g. Noyes et al. (1984), Hempelmann et al. (1995), and Mamajek & Hillenbrand (2008). Its theoretical basis, however, is the dynamo effect. The faster the star spins, the stronger the magnetic field, and the more active the star.

Rapid rotators typically have periods of a few days. Spots usually must have lifetimes longer than the rotation period to be detected; otherwise they are hard to trace and confirm. Many lightcurves show fast variations indicating quickly evolving spot distributions where the existence of spots seems probable but can hardly be confirmed.

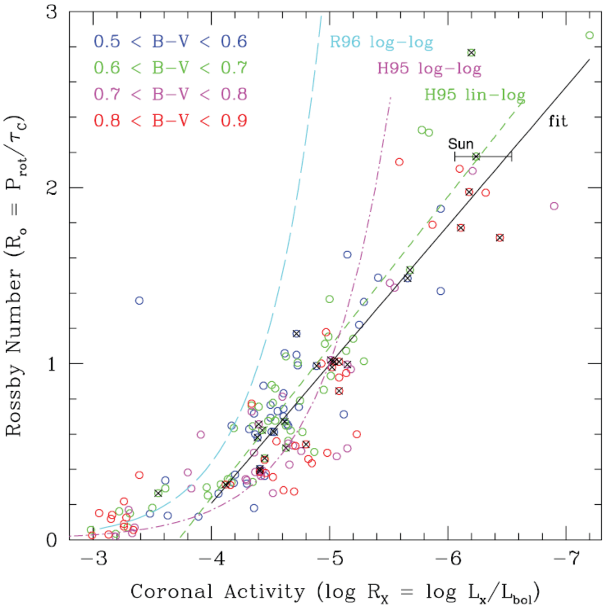

Figure 2.2: Activity-rotation relation from coronal emission (Mamajek & Hillenbrand 2008). The X-ray emission R_X indicates coronal activity. Stars with higher Rossby Numbers also show higher activity.

Very often a photometric rotation period is difficult to determine. The projected rotation velocity $v_{\rm eq}\sin(i)$ is a good indicator for rapid rotators as well; it can be extracted from the Doppler broadening of spectral lines. If this Doppler broadening clearly dominates the other processes of line broadening, which usually is the case at about $v_{\rm eq}\sin(i) \gtrsim 20$ km/s, the star can be classified as a rapid rotator. Such stars are potential candidates for *Doppler Imaging* (DI), where the spot distribution can be recovered from the deformation of line profiles in a series of spectra.

However, even if a star is a rapid rotator, it does not necessarily show spots. One of the criteria that are known to be important is the star's spectral type: spots are phenomena of late-type stars with outer convection zones.

2.1.3 Spectral type

Stars with masses of $M \lesssim 1.5\ M_\odot$ are supposed to show surface convection. This upper boundary is the mass region of main-sequence A type stars. Numerical models indicate a limit of $T_{\rm eff} \sim 8300$ K (Christensen-Dalsgaard 2000) for stars with outer convection zones, and observations seem to confirm that boundary line (see e.g. Simon et al. 2002). This means that all (middle) A type stars, and later stellar types, potentially have spots.

The convective shells of A type stars must be very shallow and it is not clear whether these stars really show spots. Until now no temperature distribution maps of a main-sequence A type star have been presented, and there are no conclusive detections of dark spots in high-precision lightcurves of this or early stellar types either. It seems that cool spots analogous to sunspots do not show up on stars earlier than F type. Although this assumption might be caused by a bias resulting from the detection techniques, there are only very few Doppler images of F-type stars. One example is the late F-type star σ^2 CrB A which is a member of a binary system (Strassmeier & Rice 2003). The case is even more complicated for studies of photometry, because many lightcurves of early-type stars show variability which is caused by pulsations rather than spots. If some of them contain features of spots as well, they are hard to detect.

2.2 Observation techniques

This section introduces different techniques which are successfully used to analyze stellar surface features and their evolution. Helpful overviews and reviews on this topic, as well as on the properties of starspots, can be found, e.g., in Berdyugina (2005) and Strassmeier (2009).

2.2.1 Lightcurves

In lightcurves spots are visible due to the rotation of the star. This rotational modulation of the brightness, when the spot moves onto the visible hemisphere on the one side and disappears on the other side, is used to study properties of stars and their surface inhomogeneities. Although this idea was already applied to lightcurves by Kron (1947), it took much more time and a lot more research (e.g. Hoffmeister 1965; Chugainov 1966; Hall 1972) until it was generally accepted that variability in lightcurves really indicates starspots.

Numerical techniques trying to reconstruct the spot distribution from the observed lightcurve are commonly referred to as *lightcurve inversion*. Pioneering work was carried out, e.g., by Bopp & Evans (1973) and Torres & Ferraz Mello (1973) who first used simple one-spot models to fit periodic brightness variations.

Although the techniques were further improved, the basic problems of lightcurve inversion do not change. The resolution of surface reconstructions is low, mainly because latitudinal positions, sizes, and shapes of spots are poorly constrained. A common approach is a two-temperature solution, where spots and photosphere have (pre-)defined temperatures/brightnesses, which is a necessary simplification because size and brightness of spots are interdependent quantities.[b] These problems are even increased by other effects as, e.g., stellar limb darkening and the existence of faculae.

The problems of lightcurve inversion are usually summed up by the term *uniqueness*. The two-dimensional information on the stellar surface needs to be extracted from one-dimensional data. However, different spot distributions can lead to the same lightcurve. Thus, the surface reconstructions are not unique solutions to the inverse problem. Although this is of course a problem which limits the amount of information contained in a lightcurve, it is still possible to learn a lot about starspots and active regions. Furthermore, lightcurves are especially useful to determine the (photometric) rotation periods of stars.

2.2.2 Eclipse mapping

Although the eclipse mapping technique uses lightcurves as well, it surpasses the ordinary lightcurve methods to analyze starspots and, thus, is of outstanding importance. Already Kron (1947) noticed the effect of dark spots in his lightcurves of eclipsing binaries as deformations of the eclipse profile. Numerical approaches to analyze lightcurves of eclipsing binaries and to reconstruct their surface distributions were presented, e.g., by Vincent et al. (1993) or Rodono et al. (1995).

Even more powerful, and applicable to single stars, is the use of *planetary eclipse mapping*. Planets crossing the stellar surface scan the underlying spot distribution which is mapped onto the transit profile in the lightcurve. An especially appealing system is the active star CoRoT-2, which is transited by a large planet, where Huber et al. (2009a) and Huber et al. (2010) performed planetary eclipse mapping (see Sect. 6.2 and 6.3).

---

[b] Large and moderately dark spots and small but utterly dark spots have very similar effects on lightcurves. In both cases the brightness minimum can be equally deep and the effect of the larger spot size on the shape of the lightcurve minimum is weak.

The deformation of transit profiles due to spots is illustrated in Fig. 2.3 for transits of CoRoT-2 b and two different spot radii $R_{\rm sp} = 8°$ and $R_{\rm sp} = 15°$. For extremely high photometric precision and dense sampling rates the radii of the spot $R_{\rm sp}$ and the planet $R_{\rm P}$ can be determined from the occultation time τ of the spot:[c]

$$R_{\rm sp} + R_{\rm P} = \pi\, a\, \frac{\tau}{P}\ .$$

Quantity P is the orbital period of the planet and a is its semi-major axis.

If the spot is larger than the planet, theoretically even the spot radius $R_{\rm sp}$ can be derived directly from the plateau at the center of occultation (see Fig. 2.3). In practice this is difficult because the spots probably have complex inner structures and/or the planet is not crossing one individual spot but spot groups.

An example for a lightcurve containing several consecutive transits of the same spot is presented in Fig. 2.4. The rotational modulation of the lightcurve caused by the spot is clearly visible in the upper panel; the lower panels show individual transits. From such a series of transits the longitudinal position and the size of a spot can be recovered extremely well. If the exact path of the planet across the disk is known, the latitudinal position of the spot can be determined with high accuracy as well.

Modeling the deformations of the transit profiles simultaneously with the rotational modulation caused by the spots yields tremendous possibilities of high-resolution surface imaging. For long-term photometry this is especially appealing because the evolution of the spot pattern – and possibly even individual spots – can be resolved in detail over long periods.

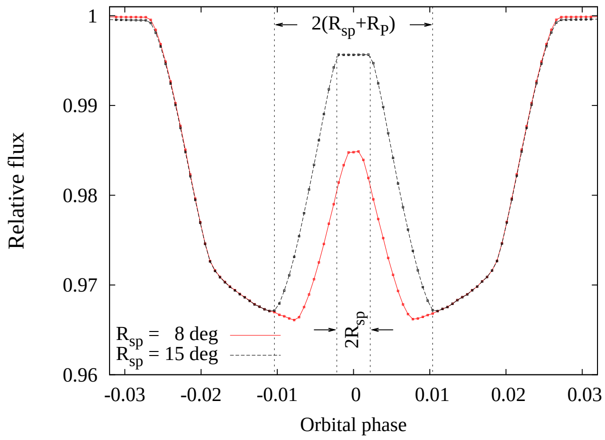

Figure 2.3: Simulated transit profiles of CoRoT-2 b deformed by the occultation of a spot. The red curve shows the signature of a spot with radius $R_{\rm sp} = 8°$, the black curve presents the calculation for $R_{\rm sp} = 15°$. Both curves are normalized to a continuum of unity. The dashed vertical lines indicate that the radii of the spot $R_{\rm sp}$ and the planet $R_{\rm P}$ can be determined from the bump in the transit profile; this is only illustrated for the black curve (large spot).

Even though the modeling of spot signatures in individual transits was already presented for some objects (Pont et al. 2007; Rabus et al. 2009; Wolter et al. 2009), Huber et al. (2009a) and Huber et al. (2010) were the first to apply a *consistent* approach reconstructing the rotational modulation and the transit deformations *simultaneously* (see Sects. 6.2 and 6.3).

---

[c] This equation is only exact for a *central* eclipse of the spot by the planet,i.e., it is not exact if the planet is only grazing the spot. If this equation results in $R_{\rm sp} + R_{\rm P} < R_{\rm P}$ the spot must have been grazed.

2.2.3 Radial velocities

Similar to lightcurves, radial velocity (RV) variations of active stars also contain spot signatures. Spots deform the spectral line profiles which causes an apparent shift of the line center very similar to the Rossiter-McLaughlin effect for transiting planets (see Sect. 3.3.2). Therefore, this effect is sometimes referred to as *activity-induced* RV variation or *activity-induced Rossiter-McLaughlin effect*.

So far the effect of stellar activity on high-precision RV measurements is usually treated as additional 'noise' (Saar & Donahue 1997; Hatzes 2002). However, since even small spots have a rather strong impact on RV curves, this effect can be used to study stellar activity. Figure 2.5 shows two curves for activity induced RV variations, one illustrating the effect of one spot with a size of 0.5 % of the stellar disk, the other one for a spot size of 0.1 %. The spot sizes are comparable to large sunspots; their amplitudes are much larger than the achievable precision of RV measurements (several m/s). This is not yet a common practice for activity research, but the applicability has been shown, e.g., in Huber et al. (2009b) (see Sect. 5). There the authors showed that Doppler images can be used to calculate RV shifts caused by

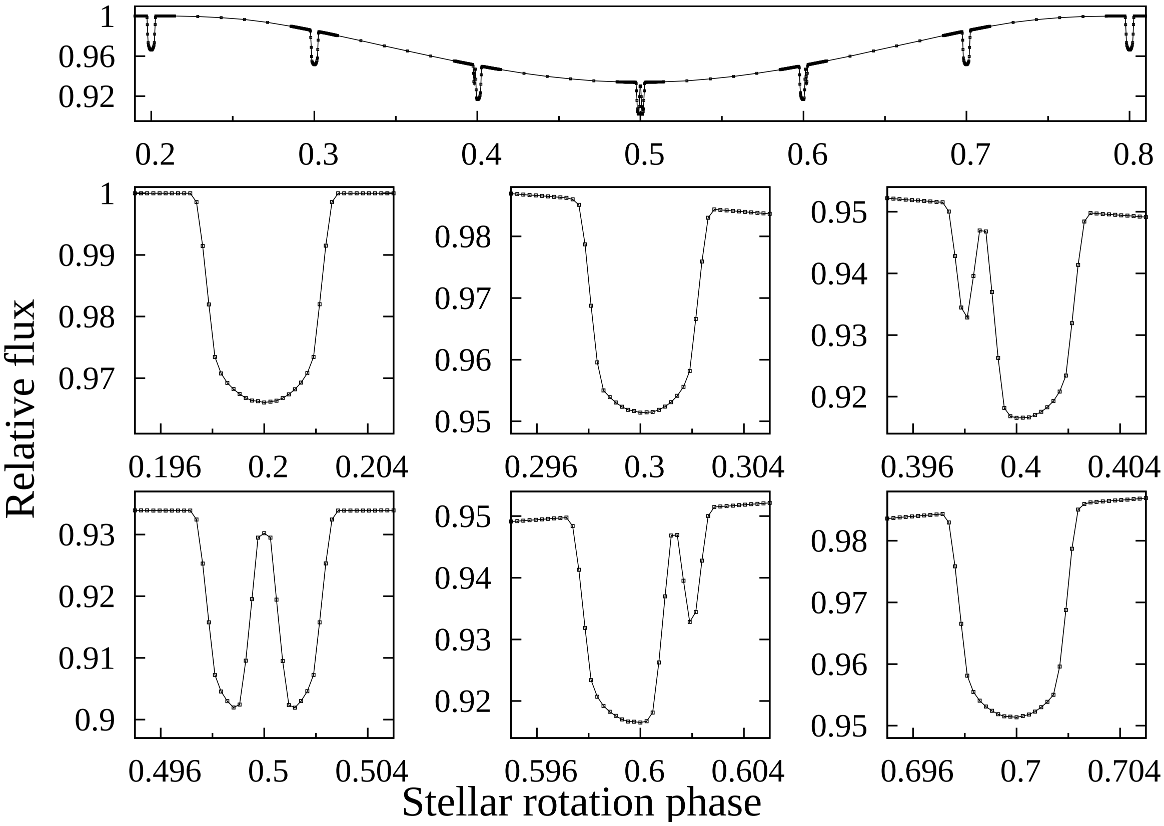

Figure 2.4: Simulated lightcurve of CoRoT-2 with one spot at 180° longitude and a radius of $R_{\text{sp}} = 15°$. To illustrate the effect of the different longitudinal positions of the spot during the stellar rotation on the transit profiles of the planet CoRoT-2 b, transits for an orbital rotation period of $P_{\text{P}} = P_{\text{Star}}/10$ are calculated. The upper panel shows the entire lightcurve, the lower panels show close-ups of six individual transits. The series of transits visualizes nicely how the deformation caused by the spot moves through the profile.

the spot distribution; the reconstructed RV curve is in good agreement with the variations found in contemporaneous long-term RV measurements.

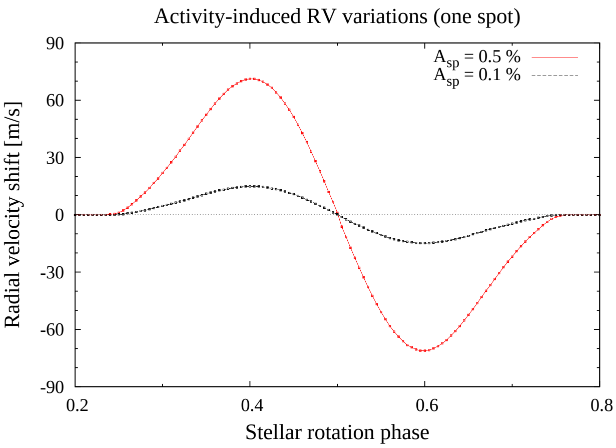

Figure 2.5: Activity-induced RV variations due to spots. The red curve illustrates one spot the size of 0.5 % of the stellar disk, the black line is for one spot size of 0.1 %. The used stellar parameters are that of CoRoT-2 ($v \sin(i) = 12$ km/s).

In Table 2.1 the effect of spots on lightcurves and RV measurements for some stars are presented. The amplitude K caused by spots in RV measurements can be comparably large even for slow rotators as the Sun. A comparison to Table 3.1 illustrates the problems for planet detection caused by stellar activity. Solar spots with sizes of 0.1 % of the disk cause RV shifts 20 times as high as the Earth. However, spots are emerging and disappearing which provides a possibility to discern them from planetary signals.

The values of Table 2.1 are plotted in Fig. 2.6. The relation between the RV amplitude K and the other parameters can be approximated by

$$K \approx \kappa \left(1 - \frac{T_\bullet^4}{T_\star^4}\right) \frac{A_\bullet}{A_\mathrm{disk}} v \sin(i) \; . \tag{2.1}$$

The coefficient $\kappa = 0.0132 \pm 0.0004$ is determined by a linear regression also shown in Fig. 2.6.

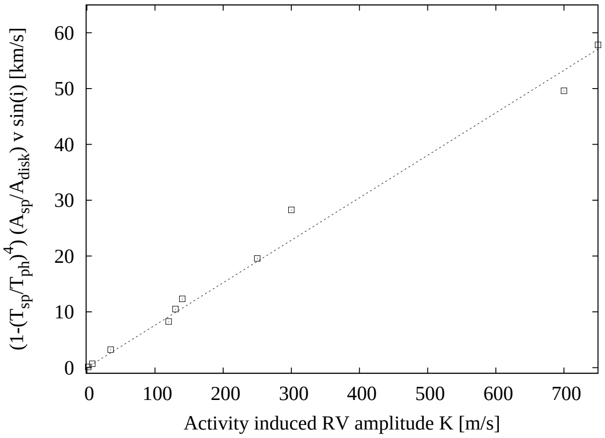

Figure 2.6: Values of Table 2.1 including a linear regression. This graph illustrates the relation between the amplitude K of the activity-induced RV variations and properties of the spot and the star; T_sp and T_ph are the temperatures of spot and undisturbed photosphere, A_sp and A_disk are the areas of spot and stellar disk, and $v \sin(i)$ is the projected rotation velocity of the star.

In analogy to lightcurve inversion, a densely sampled curve as shown in Fig. 2.5 could be used for RV curve inversion: the spot distribution is recovered by modeling the RV signal. Possible approaches could be very similar to lightcurve modeling. Spots are set on a surface and their positions and sizes are changed until the RV curve is sufficiently reconstructed. Alternatively, a gridded surface could be used as well, where the brightness of individual surface elements is changed.

The RV shift caused by the spot distribution has to be calculated. One possibility is the use of different spectra for surface elements with photospheric temperature and for those with spot temperatures. The integration over the visible stellar disk for each rotation phase results in a series of spectra

Table 2.1: Illustration of the influence of spots on lightcurves and RV measurements for some selected stars. The columns give the projected rotation velocity $v \sin(i)$, the effective temperature of the star $T_\star$ and the spot $T_\bullet$, the ratio between spot and disk area $A_\bullet/A_{\mathrm{disk}}$, the RV amplitude K caused by the spot, and the rotation period of the star P. Note that $A_\bullet/A_{\mathrm{disk}} \approx \Delta I/I$ for spots with low temperature ($T_\bullet^4/T_\star^4 \ll 1$).

Star	**v sin(i)**	**$\mathbf{T_\star}$ (K)**	**$\mathbf{T_\bullet}$ (K)**	**$\mathbf{A_\bullet/A_{disk}}$**	**K (m/s)**	**P (d)**
Sun	2 $\frac{\mathrm{km}}{\mathrm{s}}$	5800	4300	0.1 %	2	25
				0.5 %	8	
CoRoT-2	12 $\frac{\mathrm{km}}{\mathrm{s}}$	5625[a]	4200[b]	1 %	120	4.5
				6 %[c]	700	
			5200[c]	1 %	35	
τ Boo	16 $\frac{\mathrm{km}}{\mathrm{s}}$	6360[d]	4400[b]	1 %	140	3.3
EK Dra	17 $\frac{\mathrm{km}}{\mathrm{s}}$	5850[e]	4600[e]	1 %	130	2.6
LQ Hya	26 $\frac{\mathrm{km}}{\mathrm{s}}$	5175[f]	3650[f]	1 %	250	1.6
V889 Her	39 $\frac{\mathrm{km}}{\mathrm{s}}$	5800[g]	4200[g]	1 %	300[h]	1.3
AB Dor	89 $\frac{\mathrm{km}}{\mathrm{s}}$	5200[i]	4000[i]	1 %	750	0.5

[a] Bouchy et al. (2008). [b] Spot temperatures are estimated from Fig. 2.10. [c] Huber et al. (2010) estimate the largest observed *asymmetric* spot distribution of CoRoT-2 from the deepest lightcurve minimum. However, the calculated K is only true for one individual spot of this size. [d] Leigh et al. (2003). [e] Strassmeier & Rice (1998). [f] O'Neal et al. (2001). [g] Marsden et al. (2006). [h] Note that Huber et al. (2009b) measure an amplitude between 400 and 600 m/s, which would corresponds to an area of about 1.5 to 2 % for one coherent individual spot of $T_\bullet = 4200$ K. [i] Donati et al. (2003); Berdyugina (2005).

where the RV variation over stellar rotation can be determined. A simpler approach is to determine the barycenter S of a line profile and to identify the variation of S caused by a deformation of the line profile with the RV shift. Although this is not absolutely correct, S seems to be a feasible approximation for the true RV shift and was, e.g., used in Huber et al. (2009b).

There are indications that this technique probably recovers more information on the stellar surface than lightcurve inversion. Some test reconstructions of simulated lightcurves and RV curves performed during this thesis showed that at least a combination of simultaneous RV curves and lightcurves results in better reconstructions of the surface than using only one type of data. Especially the latitudinal position of spots seems to be recovered more precisely which is indicated by results of simulations for a surface with two spots presented in Fig. 2.7. A possible explanation, although not yet thoroughly examined, could be that the shape of RV curves is more sensitive on certain parameters, as e.g. spot latitude, than lightcurves.

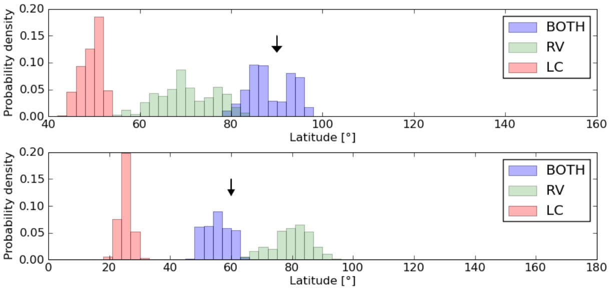

Figure 2.7: Simulation of the reconstruction of latitudinal positions of two spots (upper and lower panel). The black arrows indicate the correct value. The red bars show the reconstructed value from only lightcurve inversion, the green bars from only RV curve inversion, and the blue bars for a combined fit.

Starspots also influence the Rossiter-McLaughlin effect of planets (see Sect. 3.3.2). During the planet's transit across the disk less light is blocked if it occults a spot than if it crosses the undisturbed photosphere. These brightness inhomogeneities lead to deformations of the Rossiter-McLaughlin curve. This is illustrated in Fig. 2.8 where a transit of CoRoT-2 b is simulated with and without spots.

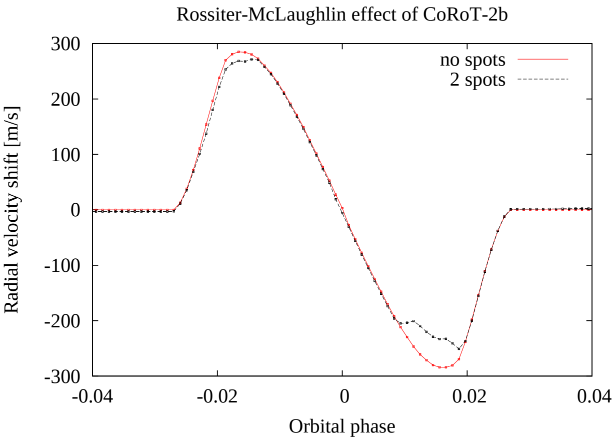

Figure 2.8: Simulation of the Rossiter-McLaughlin effect for CoRoT-2 b. The red curve illustrates the effect if no spots are on the eclipsed section, the black line shows what effect spots have on the shape of the curve. One spot with a size of 0.5 % of the disk is located at 300° longitude, the other one with 0.1 % size is placed at 30° longitude. The planet crosses the disk at stellar phase zero. An asymmetric distribution of starspots shifts the entire RV curve; thus, the black curve was corrected by adding a constant RV value of 35 m/s.

So far this effect was not used to study starspots. Considering the amplitude of the Rossiter-McLaughlin effect for CoRoT-2 b, an application for at least some planets seems absolutely possible.

2.2.4 Doppler Imaging (DI)

To this date, the most successful method to resolve stellar surfaces is the Doppler Imaging technique. The spectral lines of stars are broadened by various effects. One of them is the Doppler broadening, which usually dominates other broadening effects in stars with projected rotation velocities of $v\sin(i) \gtrsim 20$. The spots on the surface are mapped into the rotation profile of the spectral lines. Using high-resolution spectroscopy, the stellar surface distribution can be reconstructed from a time-series of spectra.

The first to develop this idea was Deutsch (1958), applying it to the mapping of chemical peculiarities on the surface of the Ap star HD 125248. Vogt & Penrod (1983) were the first to obtain a Doppler image of a star with (cool) spots using spectra of the RS CVn-type star HR 1099. Since then many stars have been imaged; a list is given in Strassmeier (2009). An intuitive illustration of the basic idea of DI is given in Fig. 2.9.

Although DI recovers much more information on the stellar surface than lightcurve inversion, it still is an ill-posed *inverse problem*; the reconstructed image is non-unique. Several different reconstruction algorithms were developed which try to implement *a priori* knowledge of the surface distribution into the reconstruction: this is called *regularization*. Using such a constraint, the ill-posed problem becomes an unique solution.

Mainly three different regularizations are used. The maximum entropy method maximizes an entropy-like measure applied to the solution and, in effect, minimizes the spot coverage of the resulting surface. Numerical codes were developed and used, e.g., by Vogt et al. (1987) and Rice et al. (1989). The Tikhonov regularization, which was applied for example by Goncharskii et al. (1977) and Piskunov et al. (1990), minimizes local gradients of the stellar surface distribution.

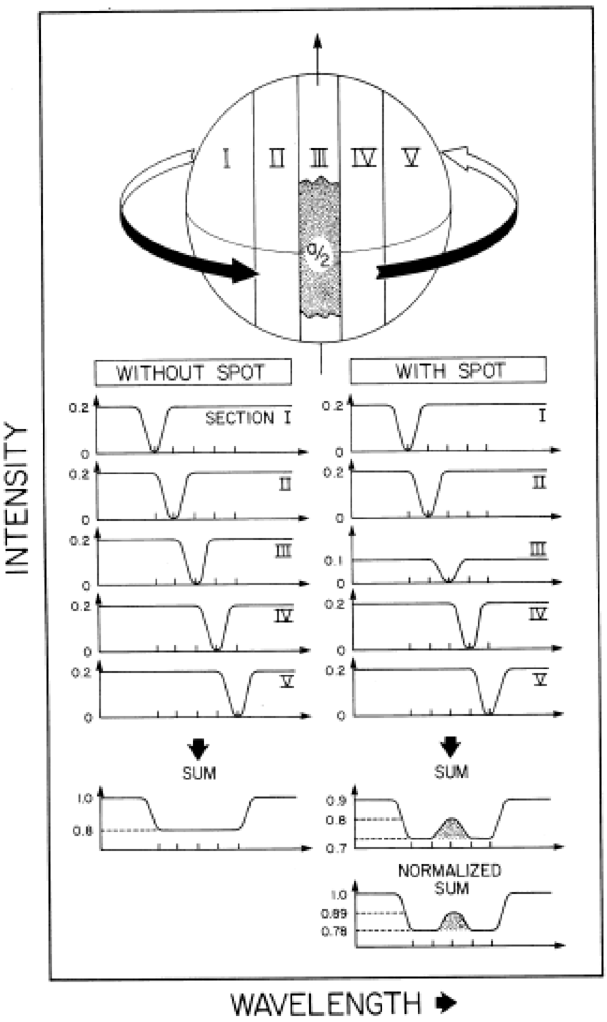

Figure 2.9: Deformation of a spectral line by a dark spot, as employed by Doppler Imaging (Vogt & Penrod 1983). The spot appears as a bump in the line profile. With rotation this bump moves through the profile.

The CLEAN-like DI (CLDI) approach was developed by Kürster (1993), motivated by a deconvolution algorithm frequently applied in radio astronomy, and used, e.g., in Kürster et al. (1994) and Wolter et al. (2005). It constantly increases the number of spotted elements on the reconstructed surface; additionally, the number of 'allowed' brightnesses/temperatures is predefined. This way it is a priori determined how many different spot temperatures/brightnesses are possible for surface structures. The numerical code of Wolter et al. (2005) was also used in Huber et al. (2009b) to Doppler image the active star V889 Her; the publication is part of this PhD thesis (see Sect. 5).

DI has the capability of recovering latitudinal information on starspots, which is one of its main advantages. The resolution depends on the phase coverage of the stellar rotation, the spectral resolution and signal-to-noise ratio of the spectra, as well as on the rotation velocity of the star. However, the observational costs for high-resolution images and long-term monitoring are high.

A closely related technique is *Zeeman-Doppler Imaging* (ZDI) using the magnetic splitting of spectra lines due to the Zeeman effect. ZDI requires polarization measurements. Because the signatures of spots are small, either the quality of the spectra has to be extremely high (S/N of a few hundred) or simultaneous fitting of multiple lines needs to be employed. This powerful technique to recover spot distributions and magnetic field vectors was pioneered by Semel (1989) and Donati et al. (1989).

2.3 Starspot characteristics

So far the spot distributions of a few hundred stars have been analyzed (Strassmeier 2009). The following section sums up some of their important characteristics.

2.3.1 Sizes

The determination of spot sizes is a crucial problem for all observation techniques. Some potential problems are:

1. The resolution of the surface is limited. The smallest resolvable spot must be as big as the surface element. A smaller spot with the same brightness increases the brightness of the surface element; however, the ‘size’ stays the same.

2. A small spot with a certain brightness located at the equator appears very similar to a larger spot at a higher latitude. A wrong reconstruction of the latitudinal position affects the size.

3. Different regularization techniques lead to – at least to some degree – different surface reconstructions. It was shown that the Tikhonov regularization generates smoother spot distributions than the maximum entropy approach (Piskunov 1991). This leads to smaller spots for the latter regularization. Predefining the spot brightness, as for example done in two-temperature maps, of course influences the sizes as well, because a wrong spot temperature must be compensated by the size.

Keeping these uncertainties in mind, the largest starspot ever reconstructed covered 22 % of a hemisphere (Strassmeier 1999).[d] The minimum sizes of starspots depend highly on resolution limits; small, isolated starspots of approximately 1 ‰ of the surface were found by Barnes (2005) and Wolter et al. (2005). These detections are biased because smaller spots are easier to resolve on rapidly rotating stars.

---

[d] This section does not discuss symmetric parts of the spot distribution as for example polar spots (see Sect. 2.3.3). Polar spots are often the largest structures on Doppler images, but their exact properties are notoriously uncertain. It is a problem of most observation techniques that they are insensitive on detecting the symmetric part of the spot distribution. This suggests that the total spot coverage of many stars is even higher, which is supported by different analysis techniques (e.g. O’Neal et al. 1996; Jeffers et al. 2006).

A simple indicator for spot sizes is the modulation amplitude of lightcurves. The largest amplitude ever observed was $\Delta V = 0.65\,\mathrm{mag}$ for the T Tauri star V410 Tau (Strassmeier et al. 1997) suggesting a starspot size of about 20 % of the entire surface. However, a simple estimation of spot coverage from lightcurve amplitudes gives only little information on spot sizes because no information on the number of individual spots is available.

It would be interesting to see how the spot size distribution of stars compares to the Sun (see Sect. 1.2.3). Although many stars have been analyzed for starspots so far, a conclusive size distribution has never been presented, mostly because the uncertainties are too high. Solanki & Unruh (2004) assume that starspot areas are distributed similar to sunspots and conclude that even for the most active stars a large fraction of spots is below the resolution limit.

2.3.2 Temperatures and brightnesses

Starspot temperature[e] and size are correlated. Using additional information, the temperature can be determined from lightcurves or spectra.

Multi-color photometry is one way of determining the temperature of starspots (e.g. Poe & Eaton 1985). Some DI codes can determine absolute spot temperatures, although the analysis is complex and includes many uncertainties. A successful alternative method is the analysis of line-depth ratios first presented by Gray & Johanson (1991). Combinations of these different approaches yield the best results for starspot temperatures so far; however, precise absolute temperatures are still rare.

Berdyugina (2005, Table 5) presents a list of stars and their temperature differences between photosphere and spotted regions. Typically, solar-like stars (G type) have spot temperatures of about 2 000 K lower than the photosphere; in late-type stars this difference reduces to about 200 K (mid M-type). Figure 2.10 shows the apparent dependence of ΔT on the photospheric temperature.

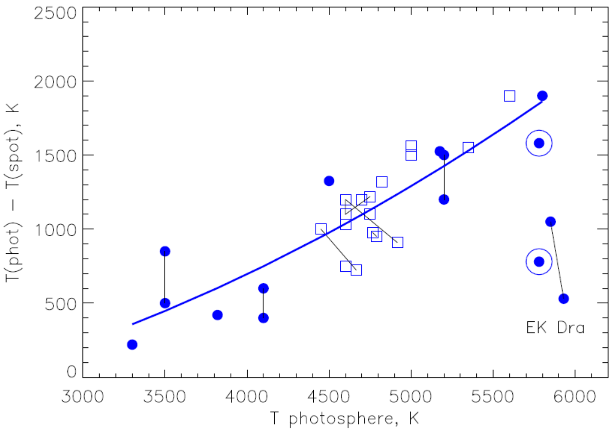

Figure 2.10: Temperature difference between starspots and the undisturbed photosphere (Berdyugina 2005). Squares symbolize active giants, circles stand for active dwarfs. Thin lines connect different measurements of the same star. The two dots within circles roughly indicate umbral and penumbral values of the Sun.

A comparison of the temperatures from Berdyugina's table to the solar spot contrast $\alpha = 0.3$ (see Sect. 1.2.4) ends up with rather similar values for solar-like stars. Some examples for G dwarfs are $\alpha \approx 0.2$ (HD 307938) or $\alpha \approx 0.35$ (HD 307938). For M-type stars the value becomes bigger and is roughly about 0.5 to 0.6.

---

[e] Temperature and brightness are basically equivalent. Physically the temperature is the value of interest, but in reconstruction techniques often the brightness (or filling factor) is used. The (relative) brightness of a spot can be converted to a temperature if the photospheric temperature is known (see Sect. 1.2.4). Filling factors can be converted to temperatures when the spot contrast is known (or estimated).

Huber et al. (2010) use planetary eclipse mapping to determine the brightness of a spot on the eclipsed section of the G7V star CoRoT-2 (see Sect. 6.3). Their result indicates a starspot brightness of $b \approx 0.76$, which translates into a temperature of ~ 400 K lower than the photosphere. Although this temperature seems to be very low, it is in good agreement with the Sun because most of the area should be covered by the penumbra; thus, this is not the effective umbra but rather the penumbra temperature.

2.3.3 Polar spots and active belts

Many Doppler images show large spots on the pole, as visible, e.g., in the reconstructions of V889 Her in Sect. 5. This 'problem' is known since the early days of DI and the reality of polar spots has been controversial for a long time. An overview on this topic can be found in Rice (2002). Since polar spots can easily be the results of artifacts of the DI process, e.g., due to incorrectly adopted line profile parameters (see e.g. Bruls et al. 1999), their reality has been intensively debated during the early history of DI. Nowadays, these features are accepted as real, primarily because careful DI also produces reconstructions of stellar surfaces without polar spots, and theoretical models suggest the existence of high-latitude and polar spots (Schüssler & Solanki 1992).

An attractive theory to explain the existence of polar spots, and their mixture of different polarities, are strong meridional flows (e.g. Schrijver & Title 2001; Holzwarth et al. 2006). A surface velocity field directed from the equator to the poles drags low-latitude spots along. They gather at high latitudes and build up the polar cap. Observational evidence for this scenario was, e.g., given by Vogt et al. (1999).

Polar spots are a good example for a symmetric spot distribution, which is hard to detect with most techniques because it does not contribute to the rotational modulation of lightcurve or spectral line profiles. Furthermore, it is difficult to discern between a polar cap and a dark belt around the star at a lower latitude. Probably a polar spot is, at least partially, a compensation for the spots distributed uniformly over the surface.

The Sun has an active belt close to the equator (±40° latitude). Other more active stars might show the same behavior with more spots located in a rather narrow belt, which would be hard to detect if a large spot fraction is 'uniformly' distributed. Huber et al. (2010) detect indications for such an active, low-latitude belt similar to the Sun. The spot coverage on the eclipsed section is (5 ± 1) % higher than on the noneclipsed part of the surface.

2.3.4 Lifetimes

The lifetimes of small, isolated starspots have not yet been reliably determined. Usually, large active regions or active longitudes are analyzed, which most likely consist of many spots. Some important points to consider are:

1. The emergence and decay of individual spots in an active region is not resolved by many observation techniques and the lifetime of an active region need not reflect the lifetime of its constituents.

2. Large spots probably do not only decay

by diffusion but are torn apart by differential rotation (Hall & Henry 1994).

3 Polar spots may present an accumulation of many spots constantly replenished by new ones (see Sect. 2.3.3). Thus, their lifetimes (or evolutionary state) is dominated by some other, probably large scale, mechanism.

4 Tidally locked binary systems have long-lived spots with much higher lifetimes than single stars.

Hatzes (1995) analyzed Doppler images and photometry for the T Tauri star V410 Tau and finds a lifetime for the dominant active region of about 20 years. Using 15 years of photometry, Strassmeier et al. (1994) observed 20 large spots with lifetimes between about 1 and 4.5 years. Hall & Henry (1994) determined lifetimes of several dozen stars from long-term photometry and arrived at the conclusion that they are proportional to their sizes. This result suggests that the decay of starspots is analogous to sunspots. More observations and techniques with better resolution of small and individual starspots will be required to show whether this relation is really correct.

2.3.5 Stellar differential rotation

Differential rotation in our Sun's outer convection zone is a requirement for the functionality of the $\alpha\Omega$-dynamo. Magnetic fields and activity are closely related; thus, differential surface rotation should play an important role for all active stars.

The differential rotation rate Ω is defined

$$\Omega = \Omega_{\mathrm{eq}} - \Delta\Omega \sin^2(\phi) , \qquad (2.2)$$

following the example of the Sun. This is similar to Eq. 1.1, where the equatorial rotation rate is $\Omega_{\mathrm{eq}} = A$, and the difference in rotation rate between the pole and the equator is $\Delta\Omega = \Omega_{\mathrm{eq}} - \Omega_{\mathrm{pole}} = -B$. The strength of the differential rotation is given by $\Delta\Omega$ which is usually given in units of rad/day. The time the equator needs to lap the pole is given by

$$P_{\mathrm{beat}} = \frac{2\pi}{\Delta\Omega} .$$

Another commonly used value is the relative differential rotation

$$\alpha = \frac{\Omega_{\mathrm{eq}} - \Omega_{\mathrm{pole}}}{\Omega_{\mathrm{eq}}} = \frac{P_{\mathrm{pole}} - P_{\mathrm{eq}}}{P_{\mathrm{pole}}} .$$

Mean values for the Sun are $\Delta\Omega = 0.055$ rad/d, $P_{\mathrm{beat}} = 115$ d, and $\alpha = 0.2$ (Berdyugina 2005).

One way to estimate differential rotation on stars is to observe the change in rotation period. The difference between the shortest and the longest period is an indicator for the average amount of rotational shear. For example, Messina & Guinan (2003) performed a study of five G0V to G5V stars and one K0V star, all showing periodic variations of the rotation period. Half of their sample shows solar-like patterns with a slowly decreasing period and a sudden increase to higher values at the start of the new cycle; the other half shows anti-solar behavior. Oláh et al. (2009) study 20 active stars and find multiple cycles for 15 of them.

Reiners & Schmitt (2003b,a) analyze the rotationally broadened line profiles of a large sample of F-, G-, and K-type stars. They find indications that differential rotation is more common for slower rotators and indications against strong differential rotation in very active stars.

For exact measurements of stellar differential rotation the latitude of starspots have to be known. This can be done comparing successive Doppler images of the same star. Barnes et al. (2005) presented a study of 10 stars with spectral types from G2 to

M2; they find a correlation of differential rotation with temperature, indicating a much stronger rotational shear for G dwarfs than for M dwarfs (see Fig. 2.11). A significant correlation of differential rotation with the rotation period was not found.

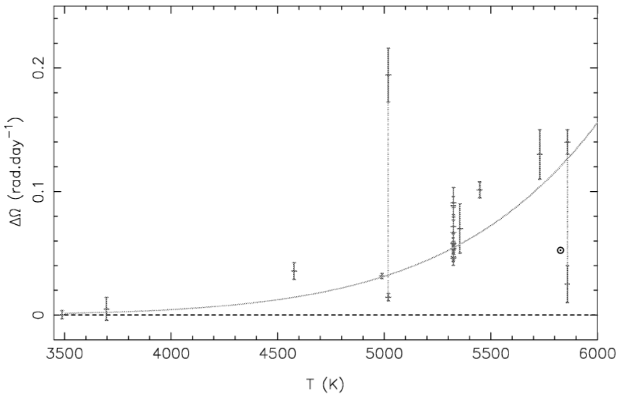

Figure 2.11: Differential rotation $\Delta\Omega$ over surface temperature for a sample of 10 stars of spectral types G2 to M2 (Barnes et al. 2005). A stronger differential rotation with increasing temperature is indicated. The Sun represented by the circle does not obey this correlation.

Huber et al. (2009a, 2010) analyze the lightcurve of CoRoT-2 for differential rotation. The advantage of this system is that the rotation period of low-latitude spots is determined extremely accurately because the planet scans starspots at latitudes between 6° and 26° (see Sects. 6.2 and 6.3). Comparing this low-latitude period to the different periods recovered from the lightcurve, the differential rotation can be estimated. Although the Sun does not follow the correlation suggested in Fig. 2.11, our analysis of the G7V-type star CoRoT-2 indicates $\Delta\Omega \gtrsim 0.1$ ($T_{\mathrm{eff}} = 5625$ K) which matches the curve nicely.

2.3.6 Active longitudes and flip-flops

Long-term photometry indicates that some stars possess active longitudes: large active regions with a preferred longitudinal position and long lifetimes. Both active longitudes are usually located at opposite hemispheres and differ in their strength of activity. Active longitudes are observed on binaries (Berdyugina & Tuominen 1998) as well as on single stars (Jetsu et al. 1991, 1993; Berdyugina et al. 2002) and frequently go along with so-called ‘flip-flops’, i.e., sudden changes of the activity level between the two longitudes. Those flip-flops are found to be periodically repeated. There are indications that in single stars the period of the spot cycle is about 3 to 4 times larger than that of the flip-flop cycle, which are ranging from about 3 years for LQ Hya to more than 6 years for FK Com (see Table 4 in Berdyugina 2005).

The surface reconstruction of the noneclipsed section of CoRoT-2 (Huber et al. 2010, Sect. 4.4) indicates a flip-flop scenario as well. In contrast to the other results, it happens on much shorter time-scales of about 40 to 50 days, which is roughly 10 times the stellar rotation period. However, the spots on the eclipsed section do not show this behavior.

2.3.7 Butterfly diagrams

The Sun shows a clear change of preferred spot latitudes during the course of its activity cycle (see Sect. 1.2.1 and the butterfly diagram in Fig. 1.3). It was long suggested that solar-like stars show a similar behavior, but this is hard to prove considering the low accuracy of reconstructed spot latitudes and the need for long-term observations of the same objects. Observations of stellar cycles would provide important information on magnetic fields, the dynamo theory, and the plasma flows on the surface. In recent years some attempts to recover butterfly diagrams were made; Berdyugina & Henry (2007) presents one for the active RS CVn-type star HR 1099 covering more than 20 years (see Fig. 2.12), Livshits et al. (2003) analyze the data of the single K dwarf star LQ Hya, and Katsova et al. (2003) give butterfly diagrams of several G- to K-dwarf stars. It should be noted that so far the precision of stellar butterfly diagrams is low and, therefore, the significance of the results is hard to evaluate.

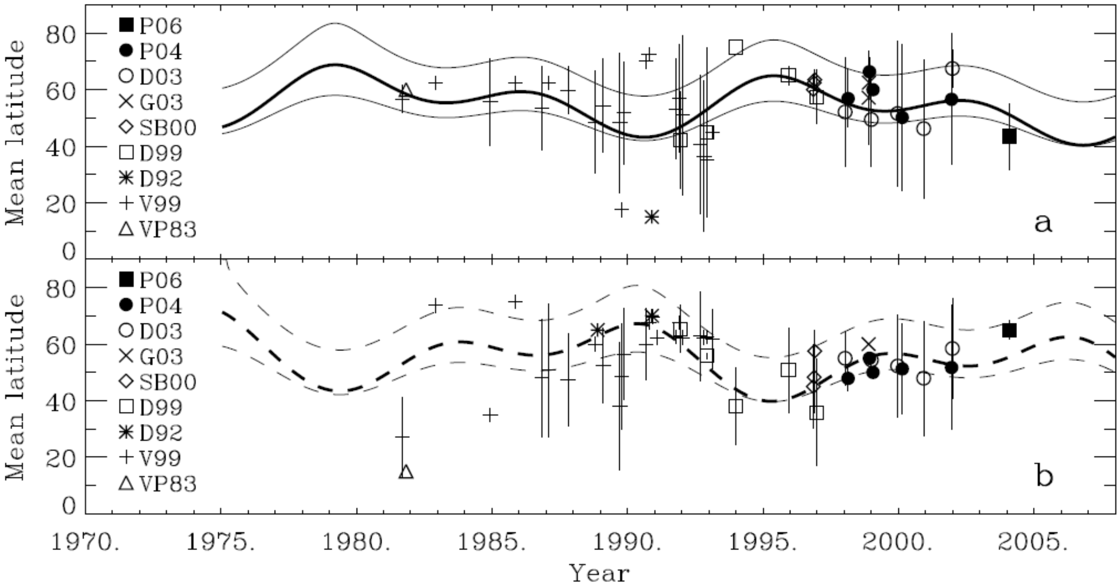

Figure 2.12: Butterfly diagram of HR 1099 (Berdyugina & Henry 2007). Shown are mean latitudes reconstructed for two large spots in separate active longitudes (panel a and b). Different symbols indicate different reconstruction techniques.

Chapter 3

Extra-solar planets

> *“ For then why may not every one of these Stars or Suns have as great a Retinue as our Sun, of Planets, with their Moons, to wait upon them? Nay there’s a manifest reason why they should. For let us fancy our selves placed at an equal distance from the Sun and fix’d Stars; we should then perceive no difference between them. For, as for all the Planets that we now see attend the Sun, we should not have the least glimpse of them, either that their Light would be too weak to affect us, or that all the Orbs in which they move would make up one lucid point with the Sun. In this station we should have no occasion to imagine any difference between the Stars, and should make no doubt if we had but the sight, and knew the nature of one of them, to make that the Standard of all the rest. We are then plac’d near one of them, namely, our Sun, and so near as to discover six other Globes moving round him, some of them having others performing them the same Office. Why then shall not we make use of the same Judgment that we would in that case; and conclude, that our Star has no better attendance than the others? So that what we allow’d the Planets, upon the account of our enjoying it, we must likewise grant to all those Planets that surround that prodigious number of Suns. They must have their Plants and Animals, nay and their rational ones too, and those as great Admirers, and as diligent Observers of the Heavens as our selves; and must consequently enjoy whatsoever is subservient to, and requisit for such Knowledge. ”*

Christiaan Huygens
Excerpt from his book *Cosmotheoros*
(Huygens 1698)

3.1 Planets around other stars

That other stars have planets orbiting around them, just as our own Sun with its eight planets, has been suggested for a long time. When interstellar clouds collapse gravitationally they build up disks; at the center of these disks stars are forming. Such a *circumstellar disk*, which is the birthplace of planets, was detected in 1984 around β Pictoris (Smith & Terrile 1984). Figure 3.1 presents a more recent picture of the system.

Observational proof of *extra-solar planets*, or exoplanets, was not available until about 20 years ago. Latham et al. (1989) detected a massive companion around HD 114762, which they categorized as a brown dwarf due to its high mass of about 11 Jupiter masses. Wolszczan & Frail (1992) discovered two planets around the pulsar PSR 1257+12 with masses well below that of Jupiter. Mayor & Queloz (1995) were the first to use the radial velocity method to detect an extra-solar planet of $\mathrm{M}\sin(i) = 0.468\ \mathrm{M}_{\mathrm{Jupiter}}$ around 51 Peg, which is a planet with about half the mass of Jupiter (see Fig. 3.2).

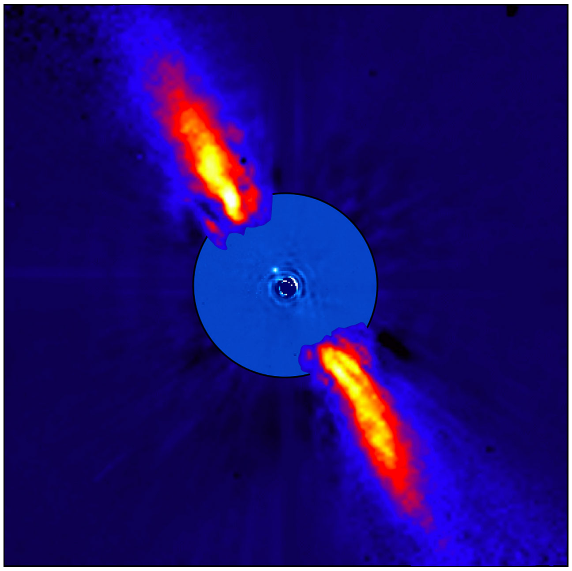

Figure 3.1: Picture of β Pictoris in near-infrared taken with the ESO 3.6 m telescope (outer part) and with the VLT (inner part). It shows an edge-on view onto the circumstellar disk and the inner planet candidate β Pic b (Lagrange et al. 2009). The picture is taken from `http://www.eso.org/public/images/eso0842a/`.

Until now (13 May, 2010) 453 extra-solar planets have been found with a variety of techniques: RV measurements, transits, timing variations, astrometry, microlensing, or even direct imaging. Even multiple planet systems are not an exception anymore. The by far most successful detection and confirmation technique is the RV method, followed by the transit method. Both techniques, and some of their results, are presented in this chapter.

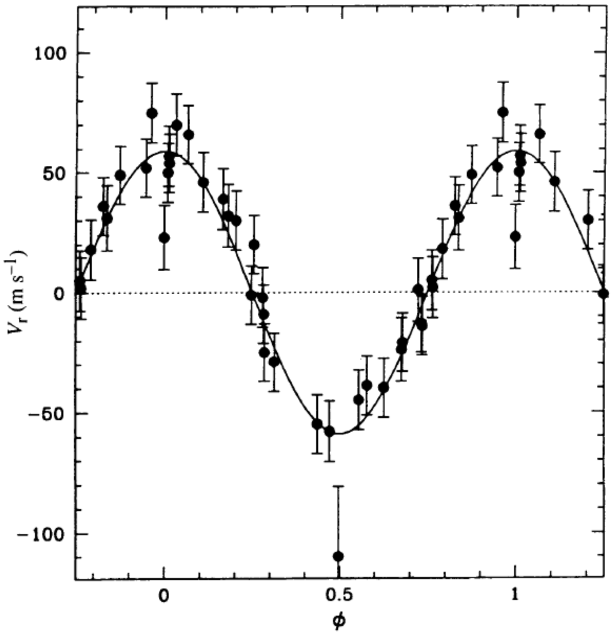

Figure 3.2: Radial velocity measurements of 51 Peg (Mayor & Queloz 1995). The dots are the measurements with errors, the continuous line is the model for a $\mathrm{M}\sin(i) = 0.468\ \mathrm{M}_{\mathrm{Jupiter}}$ companion with a period of about $P = 4.2$ days.

3.2 What exactly is an exoplanet?

A working definition for exoplanets was given by the International Astronomical Union (IAU):[a]

1 Objects with true masses below the limiting mass for thermonuclear fusion

---

[a] The definition was taken from `http://www.dtm.ciw.edu/boss/definition.html`.

of deuterium (currently calculated to be 13 Jupiter masses for objects of solar metallicity) that orbit stars or stellar remnants are ‘planets’ (no matter how they formed). The minimum mass/size required for an extra-solar object to be considered a planet should be the same as that used in our Solar System.

2. Substellar objects with true masses above the limiting mass for thermonuclear fusion of deuterium are ‘brown dwarfs’, no matter how they formed nor where they are located.

3. Free-floating objects in young star clusters with masses below the limiting mass for thermonuclear fusion of deuterium are *not* ‘planets’, but are ‘sub-brown dwarfs’ (or whatever name is most appropriate).

In other words: *‘A non-fusor in orbit around a fusor’* (Hatzes 2010).

Given in masses of Jupiter, this means:

Star:

$$M > 80\ M_{\mathrm{Jupiter}}$$

Brown dwarf:

$$13\ M_{\mathrm{Jupiter}} < M < 80\ M_{\mathrm{Jupiter}}$$

Planet:

$$M < 13\ M_{\mathrm{Jupiter}}$$

Taking a look at the mass distribution of exoplanets in Fig. 3.3 reveals the lack of brown dwarfs, which is commonly referred to as *brown dwarf desert*. This is one of the most puzzling observational results of planet search programs, since massive objects like brown dwarfs should be easy to find.

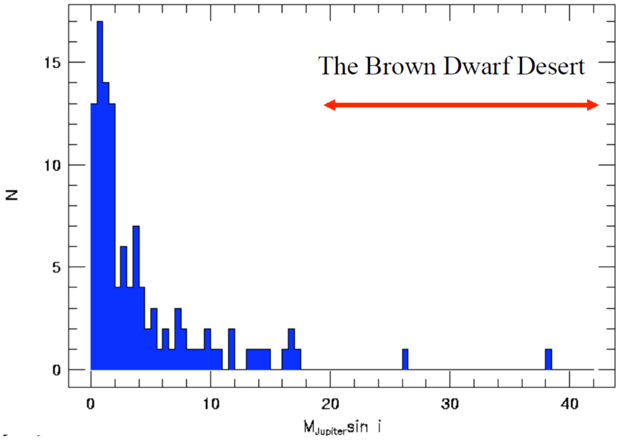

Figure 3.3: Mass distribution of extra-solar planets and brown dwarfs (Hatzes 2010). The number of detected exoplanets is much higher than that of brown dwarfs. The ‘brown dwarf desert’ is marked, indicating that these objects either are not found or exist only occasionally.

3.3 Radial velocity method

3.3.1 Detection and confirmation of exoplanets

High-precision radial velocity measurements are vital for planet detection. They opened the field of exoplanet search, make the most discoveries, can be used to determine many parameters of the system, and are necessary to confirm planetary candidates, as, e.g., found by the transit method.

The physical principle behind the RV technique is that the star and its companion orbit around the common center of mass. The movement of the star along the line of sight, although it probably is very small, can be detected by the Doppler effect. This shift of the spectrum can be determined with high precision; for suitable stars and the best technical equipment, an accuracy of below 1 m/s is possible. The amplitude of the observed RV variation (see Fig. 3.2), which is usually called K, is directly connected to the exoplanet's mass M_P, the orbital velocity V_P, and the stellar mass M_S:

$$K = \frac{M_\mathrm{P}\sin(i)}{M_\mathrm{S}} V_\mathrm{P} = \frac{M_\mathrm{P}\sin(i)}{\sqrt{M_\mathrm{S}}}\sqrt{\frac{G}{a}} \, . \tag{3.1}$$

Because the inclination i of the planetary orbit cannot be retrieved from RV measurements alone, usually the planet's mass is given as $M_\mathrm{P}\sin(i)$. Quantity G is the gravitational constant and a is the semi-major axis.

Since parameters of exoplanets are given in units of Jupiter, and the ones of their hosting stars in solar units, a conversion of Eq. 3.1 to other units is convenient:

$$K = 28.5 \cdot \frac{M_\mathrm{P}\sin(i)}{\sqrt{M_\mathrm{S}\ a}} \, . \tag{3.2}$$

Here, a has to be given in AU, M_P in Jupiter-masses, and M_S in solar masses. The result of K is in units of m/s. Table 3.1 shows some values of K for planets of the solar system and selected exoplanets.

For an overview on the technical description how high-precision RV measurements can be performed, see e.g. in Marcy & Butler (1992) or Butler et al. (1996). The basic idea is to achieve the best possible wavelength calibration where even small shifts of individual spectra can be determined. This accurate wavelength calibration is mainly realized by using superimposed absorption line spectra (e.g. Iodine) or by simultaneous calibration spectra (ThAr).

The properties of the observed star are also important for the achievable RV precision. Early-type stars have only few absorption lines; however, a high number of spectral lines to determine RV shifts is crucial for high accuracies. Rapidly rotating stars have shallow line profiles which complicates measurements as well. These two problems are the basic reason why the detection of planets around stars earlier than about F5 is difficult, at least with the RV method. Another reason is the high mass of early-type stars; the more massive a star, the more massive the companion has to be to sufficiently 'shake' the star.

For late-type stars the limiting factors are brightness and activity. Especially M type stars are extremely faint and observations of spectra with sufficient quality require the largest telescopes. Late-type stars are also very active, which introduces RV scatter limiting the precision necessary to detect planets. Possible solutions to this problem are part of this PhD thesis (see publications in Part II).

Looking at the number of exoplanets over the stellar mass in Fig. 3.4, this observational bias is clearly visible. However, for the study of stellar activity it is an important fact that most planets are found around stars with $M_\mathrm{S} < 1.5 M_\odot$. This increases the possibility that high-precision data can be used to learn more about starspots as well, maybe even about spots on solar twins.

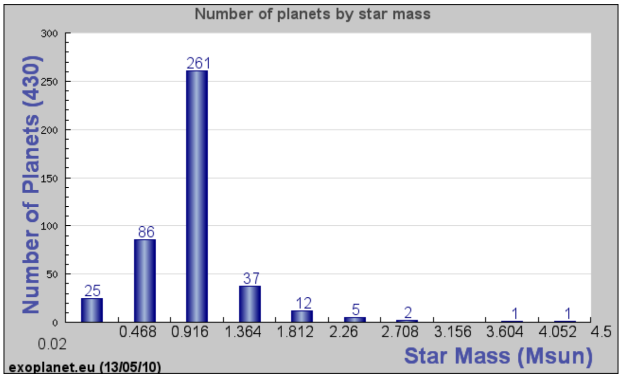

Figure 3.4: The number of extra-solar planets over stellar mass taken from the 'Extrasolar Planets Encyclopedia' (`http://exoplanet.eu`). Most planets are found around late-type stars. This distribution reveals a bias introduced by planet detection techniques (see Sect. 3.3).

3.3.2 The Rossiter-McLaughlin effect

Similar to starspots, the transit of a planet induces deformations of the spectral line profiles because parts of the stellar disk are covered. These deformations result in apparent RV shifts of the spectrum which is called the *Rossiter-McLaughlin effect* (Rossiter 1924; McLaughlin 1924). For a more detailed discussion, see Ohta et al. (2005).

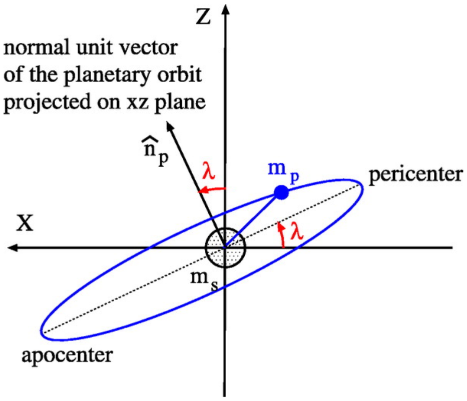

Figure 3.5: Definition of the angle λ (Ohta et al. 2005). It is the projected angle between the orbital inclination of the planet and the stellar inclination.

This effect is useful to determine the projected angle λ between the orbital inclination of the planet and the inclination of the star. The definition of this angle is illustrated in Fig. 3.5. It is an indicator whether the inclinations of star and orbit are aligned or misaligned. Furthermore, it determines the exact path of the planet across the stellar disk; an occultation parallel or tilted with respect to the equator, at higher or lower latitudes, or even only grazing transits, result in different shapes of the Rossiter-McLaughlin effect. Although it was expected that planets should always move around a star in the same direction than the star is spinning, this effect revealed that some planets indeed have opposite directions. This configuration is called *spin-orbit misalignment* and clearly detected for a small number of planets (WASP-15b and WASP-17b, Triaud et al. 2010, in preparation).

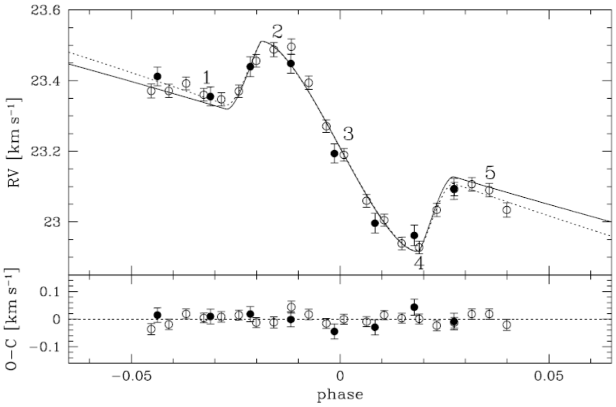

Figure 3.6: Measurement of the Rossiter-McLaughlin effect for CoRoT-2 (Bouchy et al. 2008) with the spectrographs SOPHIE (dots) and HARPS (circles). The continuous dark line is the best model indicating $\lambda = 7.2 \pm 4.5$ deg.

An example for the Rossiter-McLaughlin effect is shown in Fig. 3.6 for CoRoT-2 (Bouchy et al. 2008). The best fit to the data results in $\lambda = 7.2 \pm 4.5$ deg, which indicates that the inclinations are essentially parallel. The shape of the curve also shows that star and planet rotate in the same direction.

Such measurements are very helpful for planetary eclipse mapping (see Sect. 2.2.2). Without the results for CoRoT-2 the exact path of the planet across the stellar surface would have been uncertain. Additionally, it is important for starspot reconstructions in which direction the planet crosses the disk, at least if the star is significantly rotating during the transit.

In Sect. 2.2.3 the influence of spots on the Rossiter-McLaughlin effect is discussed; dark patches on the eclipsed section of the star lead to deformations of the shape. Since planetary parameters are derived from the exact shape of the Rossiter-McLaughlin effect, any analysis not considering starspots could result in incorrect parameters. For example, imagine that the eclipsed region on the stellar disk that is rotating away from the observer is covered with more spots than the other side. This would lead to an asymmetry of the Rossiter-McLaughlin effect which is interpreted as a tilted transit path with respect to the stellar equator. To prevent such errors, it would be helpful to simultaneously observe the transit with high-precision photometry to evaluate the influence of starspots.

3.4 Transiting planets

The first transit of an extra-solar planet was observed in 1999 for the 0.685 Jupiter-mass planet HD 209458 b by Charbonneau et al. (2000). The lightcurve is presented in Fig. 3.7. The planet orbits a G0V star and was first detected with RV measurements by Henry et al. (1999), and afterwards re-observed by Henry et al. (2000) and Queloz et al. (2000).

Figure 3.7 illustrates the transit method nicely. The brightness of a star is monitored with high-precision. When a planet is moving into the line of sight, a part of the star's light is blocked and the observed brightness decreases. After crossing the stellar disk the brightness returns to the original level.

An observation of a transit only indicates a possible planetary companion. Such *planet candidates*, as they are called, have to be confirmed. Although it is necessary to observe more than one transit to substantiate the object as a real periodically transiting companion, usually the RV method has to be applied as well. Apparent transit signals can be mimicked by several other phenomena, e.g., grazing eclipses of binaries, transits of a main-sequence star in front of a giant star, multiple systems, etc.

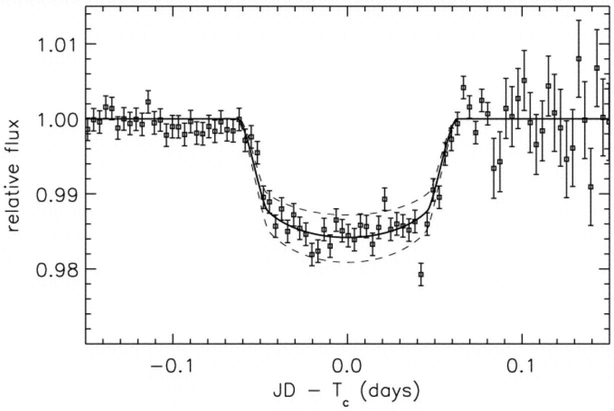

Figure 3.7: Transit of the planet HD 209458 b (Charbonneau et al. 2000). It was the first planet ever observed with the transit method. The continuous line indicates the best model referring to a planet of $M = 0.685\ M_{\mathrm{Jupiter}}$ and an orbital period of $P = 3.5$ days.

Although this technique is similar to the observation of eclipsing stars and, thus, was known for a long time already, its usefulness for planet detection had been doubted. As can be seen in Fig. 3.7, ground-based photometry is not very precise and continuous long-term observations are hardly possible. Furthermore, the planet of course has to transit the star, which means the systems has to be observed essentially edge-on.

Table 3.1 illustrates the expectations for detecting planets similar to the ones of our own system with the transit method. The drop in brightness when the object occults the star is

$$\frac{\Delta I}{I} = \left(\frac{R_\mathrm{P}}{R_\mathrm{S}}\right)^2 .$$

It equals the ratio of radii between planet and star squared; the effect of limb darkening is neglected. The probability of observing a transiting system is approximately

$$p(\mathrm{transit}) = R_\mathrm{S}/a , \tag{3.3}$$

where a is the semi-major axis of the planet. In the table, quantity N is the number of stars that has to be observed to find this planet assuming that *all* stars have such an object orbiting around them. The period P and the transit duration t are given in units of days and hours, respectively. The transit duration is calculated using

$$t = \frac{(R_\mathrm{S} + R_\mathrm{P})}{\pi \ a} P \ . \tag{3.4}$$

For convenience, this equation is better used with R_S given in units of the solar mass, R_P in units of Jupiter-masses, P given in days, a given in AU, and t resulting in units of hours:

$$t = 0.0036 \cdot \frac{(10 R_\mathrm{S} + R_\mathrm{P})}{a} P \ . \tag{3.5}$$

Even if the necessary precisions to detect the brightness drops of planets are reached, observers would have to monitor thousands of stars for hundreds of days to detect at least one transit of a planet similar to Saturn or Earth. However, when close-in Jupiter-mass planets were found, which had not been expected, detections of exoplanets with the transit method became much more likely.

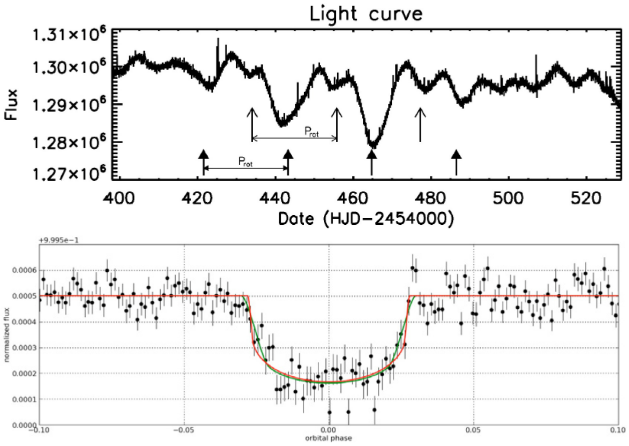

Figure 3.8: Lightcurve of the active star Corot-7 (upper panel) and the phase-folded transit of Corot-7 b (lower panel) with a drop in brightness of only about $3 \cdot 10^{-4}$ (Léger et al. 2009).

Precisions of 10^{-4} and even 10^{-5} can be reached by the space-based photometry missions CoRoT and Kepler. An example for a CoRoT lightcurve is given in Fig. 3.8 for CoRoT-7 b (Léger et al. 2009). The lightcurve of the host star shows substantial variations due to activity (upper panel); however, the transit, although only a few 10^{-4} deep, was clearly detected. Another shallow transit is presented in Fig. 3.9 observed with Kepler (Borucki et al. 2010). Especially impressive is the lightcurve of HAT-P7 observed with Kepler, which is presented in Fig. 3.10 (Borucki et al. 2009), where the reflection of the star's light from the planet is resolved, and the secondary transit (where the planet is behind the star) is visible.

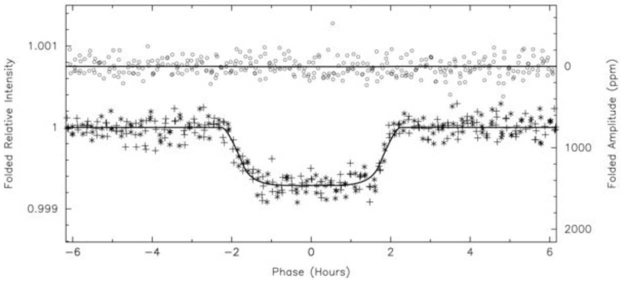

Figure 3.9: Transit of Kepler-4 b illustrating the high-precision of the Kepler photometry (Borucki et al. 2010).

Kepler was built to find an Earth-mass planet in an one-year orbit around another star; therefore, it monitors more than 100 000 stars for at least 3.5 years. Although both satellites could easily detect the drop caused by a Jupiter-like planet at 5 AU, they would have to observe the same stars for at least 12 years. However, CoRoT changes its field of view every half a year.

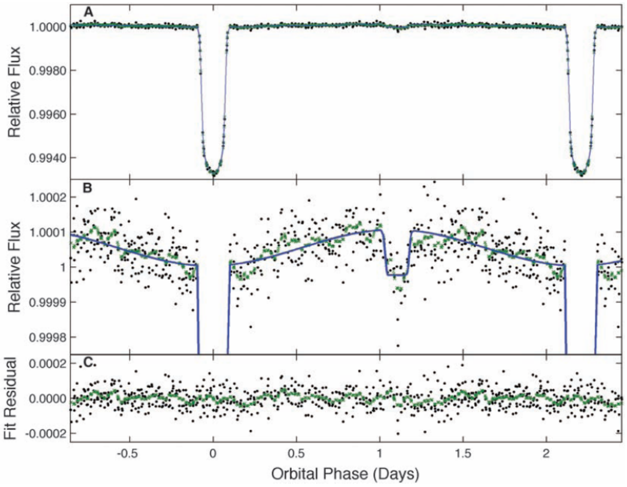

Figure 3.10: Lightcurve of the previously detected transiting planet HAT-P7 b observed with Kepler (Borucki et al. 2009). The high precision does not only allow to detect the planet's transit, but also the secondary transit and the modulation of the lightcurve due to the planet's reflection of starlight can be seen.

3.5 How many planets will be found?

An important question for researchers is: How many planets are expected to be found with the current techniques and instruments?

RV measurements indicate that roughly 10 % of all stars have giant planets (Hatzes 2010). With increasing precision this number will rise due to the detection of smaller planets. Predictions indicate that in the near future RV measurements will observe several hundreds of extra-solar planets.

Ground-based photometric observations are limited due to their comparably poor precision. Statistics show that they find on average one hot-Jupiter around 30 000 to 50 000 stars (Hatzes 2010). Space-based missions as CoRoT find about 3 to 4 hot Jupiters per field, which covers about 10 000 to 12 000 stars. On average, only one (giant) planet is found around 3 000 observed stars. Kepler seems to produce similar results, although its precision is higher and the detection of smaller planets should improve the statistics.

Until now roughly 20 planets were found with CoRoT, and about the same number is expected for the next 3 years of its operation. Optimistic prognoses expect Kepler to detect transits of more than a thousand planets with at least 50 Earth-sized planets.

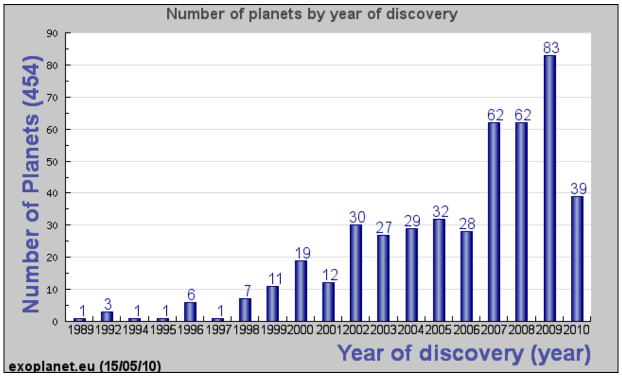

Figure 3.11: The number of of extra-solar planets plotted over the year of discovery taken from the 'Extrasolar Planets Encyclopedia' (`http://exoplanet.eu`). The detection rate of planets increases rapidly.

It is safe to say that in the next few years significantly more than thousand extra-solar planets will be known (see Fig. 3.11). Since most of them will be found around late-type stars (see Sect. 3.3), many lightcurves and RV curves will contain signatures of activity. Although probably few systems will be as advantageous as CoRoT-2 for the study of starspots, they will help to understand stellar activity better and significantly increase the statistics. However, to detect smaller and smaller planets on long-period orbits the analysis of starspots will be necessary to discern their signatures from the planetary signal; otherwise exoplanets will be lost in stellar activity even for measurements with paramount precision.

Table 3.1: Table of detection requirements and probabilities of the transit method for a selected sample of objects. Quantity $\Delta I/I$ is the drop in observed brightness during a transit, p(transit) is the probability that the orbital plane is viewed edge-on so that a transit occurs, N is the number of stars that has to be observed to find such a planet if *all* stars had one, t is the transit duration, and P is the orbital period. Additionally, the amplitude K of the planet is given that would have to be measured in radial velocities to find it. The CoRoT mission reaches precisions of about 10^{-4} in $\Delta I/I$, Kepler of about 10^{-5}. High-precision RV measurements deliver accuracies of below 1 m/s.

Planets	**ΔI/I**	**p(transit)**	**N**	**t (h)**	**P (d)**	**K (m/s)**
Mercury	$1.2 \cdot 10^{-5}$	0.012	83	8	88	0.008
Venus	$7.5 \cdot 10^{-5}$	0.0065	155	11	225	0.086
Earth	$8.2 \cdot 10^{-5}$	0.0047	214	13	365	0.09
Mars	$2.3 \cdot 10^{-5}$	0.0031	326	16	687	0.008
Jupiter	0.01	0.0009	1100	29	4380	12.5
Saturn	0.006	0.00049	2057	43	10770	2.8
Uranus	0.0013	0.00024	4110	59	30660	0.3
Neptune	0.0012	0.00016	6430	74	60225	0.3
Exoplanets	**ΔI/I**	**Prob.**	**N**	**t (h)**	**P**	**K (m/s)**
HD 209458 b	0.013	0.114	9	3.4	3.5	90
51 Peg b	0.01	0.094	11	3	4.2	59
CoRoT-2 b	0.03	0.15	7	2.2	1.74	570
CoRoT-7 b	0.0003	0.24	4	1.6	0.85	3.4
Kepler-4 b	0.0006	0.15	7	3.8	3.21	9.3
Moons	**ΔI/I**					
Moon	$6.2 \cdot 10^{-6}$					
Ganymede	$1.3 \cdot 10^{-5}$					
Titan	$1.2 \cdot 10^{-5}$					

Part II

Publications

Chapter 4

Overview

As mentioned in the previous sections, the publications of Sects. 5 and 6 deal with the reconstruction of stellar surface information based on observations originally intended for planet search. While Sect. 5 concentrates on radial velocity (RV) observations, Sect. 6 demonstrates the use of low-noise photometry for this purpose.

4.1 Doppler Imaging and RV curves of V889 Her

The publication contained in Sect. 5 (Huber et al. 2009b) presents Doppler images of the active star V889 Her. Its surface is covered with a polar spot, one dominant low-latitude active region, and several smaller features.

Interestingly, V889 Her is also a target monitored by the Tautenburg observatory to detect extra-solar planets; the resulting long-term RV measurements show large variations due to stellar activity. While these variations severely complicate the detection of planets, they enable us to *quantitatively* compare them with the expected RV variations caused by spots.

The RV variations are modulated with the rotation period of the star. Using the spot distribution of the Doppler images, the expected activity-induced RV curve is computed and compared to the measurements. A good agreement is found, indicating that the spot distribution reconstructed with DI indeed causes the observed RV variations, and that the large-scale spot distribution has a lifetime of more than one year.

4.2 Transit mapping of CoRoT-2

From the first moment the lightcurve of CoRoT-2 was published it became clear that this object is ground-breaking in several respects because the variations of a massively active star had been monitored uninterrupted for months with a data quality only obtainable from space. Furthermore, it contains transits of a large, close-in planet clearly showing deformations due to starspots. These characteristics are ideal to reconstruct stellar surface features.

As a first approach, the reconstruction of a spot from a prominent feature in only one transit was carried out, similar to the work of Pont et al. (2007) and Rabus et al. (2009) who used HST data for the stars HD 189733 and TrES-1, respectively. The results are presented in Wolter et al. (2009).[a] This paper was the starting point for many ideas, new approaches, and techniques, and led the way to the following publications.

---

[a] I participated in the development of this paper and its results contributed to my following projects. Since I am not the main author, it is not included in this PhD thesis.

The consistent reconstruction of spots from transits requires an 'undisturbed' transit profile where no deformations caused by activity are present. Taking into account the influence of spots, Czesla et al. (2009)[b] reanalyzed the transit lightcurves and determined new planetary parameters from an average transit profile where the effects of spots could largely be removed (see Sect. 6.1).

To this point, no simultaneous reconstruction of the rotational modulation and planetary transit profile deformations had ever been published. Using the cleaned transit profile determined in Czesla et al. (2009), and selecting a lightcurve interval of two stellar rotations showing only moderate changes due to surface evolution, Huber et al. (2009a) were the first to present a simultaneous and consistent reconstruction of the spot distribution from rotational modulation and transits (see Sect. 6.2). Further refining this technique, Huber et al. (2010) reconstructed the entire lightcurve of CoRoT-2 stretching over almost half a year (see Sect. 6.3). The brightness distribution and its temporal evolution are presented, and the eclipsed and noneclipsed section of the surface are compared.

4.3 Spots in RV measurements

Starspots influence the measurements of radial velocities. To simulate and analyze these effects, S. Czesla and I wrote the computer program SSP. It allows to specify the spot distribution on a stellar surface and, using different input spectra for surface elements with different temperatures, calculates the associated lightcurves and RV curves.[c]

The studies of Reiners et al. (2010)[d] required synthetic spectra of stars with different stellar types and temperatures which I provided, making use of the SSP program. PHOENIX spectra[e] of stars with photospheric temperature between 1 800 K and 5 700 K were used. These input spectra were rotationally broadened to four different rotation velocities between $v \sin(i) = 2$ and 30 km/s, including the deformation of line profiles due to a circular, cool spot. Using the resulting spectra, Reiners et al. examined the influence of spots on high-precision RV measurements and on the detection of planets around active stars.

---

[b] This publication was written in close co-operation with Stefan Czesla, and, although I am listed as second author, both of us have an equal share in its development and writing.

[c] SSP can perform several tasks. It is capable of modeling the spot distribution and its temporal evolution when certain parameters such as spot emergence and disappearance frequencies, differential rotation, or latitudinal migration are specified. It simulates planetary transits and effects caused by the underlying spot distribution. Finally, it is capable of inverting lightcurves and RV curves, reconstructing the spot distribution of the associated stellar surface.

[d] I participated in the development of this paper and give a short overview of my contributions. Since I am not the main author, it is not included in this PhD thesis.

[e] The PHOENIX stellar atmosphere code was developed by P. Hauschildt and collaborators. The used spectra were provided by A. Schweitzer. For further information, please see `http://www.hs.uni-hamburg.de/EN/For/ThA/phoenix/index.html`.

Chapter 5

V889 Herculis

Long-term stability of spotted regions and the activity-induced Rossiter-McLaughlin effect on V889 Herculis. A synergy of photometry, radial velocity measurements, and Doppler imaging.

Authors:

K. F. Huber
U. Wolter
S. Czesla
J. H. M. M. Schmitt
M. Esposito
I. Ilyin
J. N. González-Pérez

Published:

Astronomy & Astrophysics, 501, 715-728 (2009)

Reproduced with permission ©ESO

A&A 501, 715–728 (2009)
DOI: 10.1051/0004-6361/200810638
© ESO 2009

Astronomy & Astrophysics

Long-term stability of spotted regions and the activity-induced Rossiter-McLaughlin effect on V889 Herculis

A synergy of photometry, radial velocity measurements, and Doppler imaging

K. F. Huber[1], U. Wolter[1], S. Czesla[1], J. H. M. M. Schmitt[1], M. Esposito[1,2], I. Ilyin[3], and J. N. González-Pérez[1]

[1] Hamburger Sternwarte, Universität Hamburg, Gojenbergsweg 112, 21029 Hamburg, Germany
e-mail: `khuber@hs.uni-hamburg.de`
[2] Thüringer Landessternwarte Tautenburg, Sternwarte 5, 07778 Tautenburg, Germany
[3] Astrophysikalisches Institut Postdam, An der Sternwarte 16, 14482 Potsdam, Germany

Received 18 July 2008 / Accepted 6 April 2009

ABSTRACT

Context. The young active G-dwarf star V889 Herculis (HD 171488) shows pronounced spots in Doppler images as well as large variations in photometry and radial velocity (RV) measurements. However, the lifetime and evolution of its active regions are not well known.

Aims. We study the existence and stability of active regions on the star's surface using complementary data and methods. Furthermore, we analyze the correlation of spot-induced RV variations and Doppler images.

Methods. Photometry and high-resolution spectroscopy are used to examine stellar activity. A CLEAN-like Doppler imaging (DI) algorithm is used to derive surface reconstructions. We study high-precision RV curves to determine their modulation due to stellar activity in analogy to the Rossiter-McLaughlin effect. To this end we develop a measure for the shift of a line's center and compare it to RV measurements.

Results. We show that large spotted regions are present on V889 Her for more than one year, remaining similar in their large scale structure and position. This applies to several time periods of our observations, which cover more than a decade. We use DI line profile reconstructions to identify the influence of long-lasting starspots on RV measurements. In this way we verify the RV curve's agreement with our Doppler images. Based on long-term RV data we confirm V889 Her's rotation period of 1.3371 ± 0.0002 days.

Key words. techniques: radial velocities – techniques: photometric – stars: activity – stars: starspots – stars: individual: HD 171488

1. Introduction

The Sun is the only star which is sufficiently close to the Earth to resolve surface inhomogeneities in detail. Most prominent among them are sunspots. At solar maximum they cover approximately 0.3–0.4% of the total solar surface (Solanki & Unruh 2004) and individual sunspots reach diameters of roughly 2 degrees (Schrijver 2002) on average. Two examples of exceptionally large spots on the Sun were observed in March 1947 (Willis & Tulunay 1979), covering about 0.6% of the solar disk, and on March 29, 2001 (Kosovichev et al. 2001), with a size of more than 0.35% of the visible surface. The appearance and movement of sunspots is often displayed in "butterfly diagrams" which show that their positions are confined to a band of ±30–40 degrees above and below the equator (e.g. Li et al. 2001). Their lifetimes vary from a few days to several weeks ($\lesssim$ month) and appear to be related to the spot-size, larger spots persisting longer (Petrovay & van Driel-Gesztelyi 1997).

This picture seems to be different in several respects from other stars of similar spectral type, although these observations are biased towards stars with small rotation periods, which is a basic requirement of the currently available techniques to study stellar surface inhomogeneities. Contrary to the slowly rotating Sun we observe that many rapid rotators ($v \sin(i) \gtrsim 25$ km s^{-1}) possess large areas covered with features of significantly lower temperatures. One of the most extreme examples was found in the binary system VW Cep with a surface coverage of ~70% (Hendry & Mochnacki 2000). Starspots or spot groups with sizes of several dozens of degrees have been detected not only at low and intermediate latitudes, but also covering the polar regions. These polar spots form long-lasting features, sometimes persisting over years or possibly even decades (Vogt et al. 1999; Jeffers et al. 2007). The limits of current techniques often prevent us from discerning large monolithic spots from groups of individual spots within an active region. Whatever their detailed nature, these structures have much longer lifetimes than sunspots. Large spotted regions have been monitored on some stars for years showing only small changes (e.g. Korhonen et al. 2007; and Lanza et al. 2006), although individual starspots appear to evolve on timescales of several weeks (Barnes et al. 1998; Wolter et al. 2005).

Such observations gave rise to the idea of "active longitudes"; regions on the stellar surface that persist in their large scale structure (Korhonen et al. 2001). The term "active longitudes" may partially reflect a weakness of surface reconstruction methods: their ability to resolve the latitudinal position of surface features is poor, while the longitude can be determined accurately. Active longitudes show a high spot coverage stretching over a large area of the star, persisting for many months or years, which translates into several hundreds of stellar rotations. It is largely unknown whether their internal structure is variable, i.e., to what degree spots move, disappear, or form inside of

Article published by EDP Sciences

Table 1. Stellar parameters of V889 Her.

Parameter	Value
Spectral type[a]	G0V
Distance (Hipparcos)[b]	37.2 ± 1.2 pc
$M_{\mathrm{hipp,\,mean}}$[c]	$7\overset{\mathrm{m}}{.}523 \pm 0\overset{\mathrm{m}}{.}004$
$M_{\mathrm{hipp,\,max}}$[d]	$7\overset{\mathrm{m}}{.}48 \pm 0\overset{\mathrm{m}}{.}01$
$M_{\mathrm{hipp,\,min}}$[e]	$7\overset{\mathrm{m}}{.}57 \pm 0\overset{\mathrm{m}}{.}01$
V_{max}[f]	$7\overset{\mathrm{m}}{.}34$
$v\sin(i)$[f]	39.0 ± 0.5 km s^{-1}
Rotation period[f]	1.3371 ± 0.0002 d
Inclination i[f]	~55°

[a] SIMBAD Astronomical database; [b] Hipparcos Catalogue, Perryman et al. (1997); [c] mean Hipparcos magnitude and standard error; [d] maximum Hipparcos magnitude; [e] minimum Hipparcos magnitude; [f] Strassmeier et al. (2003).

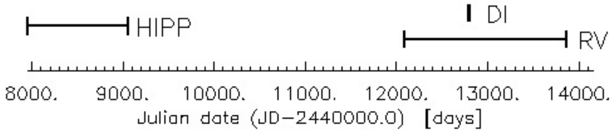

Fig. 1. Time coverage of observations used in this paper. HIPP represents the Hipparcos, DI the Doppler imaging, and RV the radial velocity data sets.

them. However, in some cases their global structure remains stable over large time periods (e.g. Berdyugina & Järvinen 2005).

In this paper we show that large spotted regions on V889's surface persist on time scales of hundreds of days. To this end we use photometric data, Doppler images, and radial velocity (RV) measurements. Section 2 summarizes characteristics of the star and its surface features. In Sect. 3 we present observational characteristics of the Hipparcos data, the Doppler imaging (DI) data, and the RV measurements. Section 4 explains the process of the lightcurve analysis, while Sects. 5 and 6 contain the analysis of the RV measurements and the DI process. Section 7 gives a discussion on all data sets and their correlation, followed by a summary of the main results in Sect. 8. Finally, the appendix covers mathematical aspects of the equation used to calculate RV shifts from line profiles, and contains all DI line profile reconstructions.

2. Object

The fast-rotating solar analog V889 Herculis (HD 171488) has been a subject of astrophysical studies for many years. Its good visibility from the northern hemisphere, large brightness, pronounced photometric variability, and high rotation velocity make it an interesting target. Its rotation period of 1.3 days is especially convenient to study the lifetimes of atmospheric structures, since observations covering four consecutive nights offer a complete coverage of all rotation phases. Therefore, it is a well-suited candidate for DI and other studies of stellar activity. Doppler images of V889 Her were published by Strassmeier et al. (2003) and Marsden et al. (2006). Some of its basic properties are summarized in Table 1.

Surface reconstructions of V889 Her from these authors reveal a large polar spot that changes in size and structure but that has always been present. Additionally, all published Doppler images show some medium- and low-latitude spots which may stretch over a few dozens of degrees and, thus, cover a significant fraction of the stellar surface. Strassmeier et al. (2003) present surface maps dominated by an asymmetric polar spot with a temperature difference of $\Delta T \approx 1600$ K to the unspotted surface at ≈5900 K. Several low-latitude spots are resolved as well with $\Delta T \approx 500$–800 K. Strassmeier et al. determined a rotation period of $P = 1.3371 \pm 0.0002$ days using long-term photometry. Marsden et al. (2006) reconstructed a polar spot of similar size down to almost +60° in latitude and two pronounced low-latitude spots at +30°. Additionally, reconstructions for the magnetic field topology were possible by Zeeman Doppler imaging (ZDI), which yielded only weak signs of a polar spot (in agreement with ZDI images of other objects, see e.g. Donati et al. 2003) and confirm the low-latitude features. Marsden et al. (2006) found a different rotation period of $P = 1.313 \pm 0.004$ days and a differential rotation of $\alpha = \Delta P/P = 0.08$, while for the Sun a value of $\alpha \approx 0.2$–0.3 was measured. ΔP denotes the difference between the equatorial and the polar rotation period.

Up to now it has not been known on what time scales spotted regions on the surface of V889 Her form and dissolve and how heavily the effects of differential rotation and meridional flows influence their development in shape and position. All surface features are presumably in constant evolution, but there are indications in previous Doppler images and reconstructions in this paper that especially large active regions besides the polar spot may have fixed positions and high stability. Evidence of such preferred longitudes was detected before in other stars (e.g. Berdyugina 2007), while Barnes et al. (1998) did not find long-lived spots on rapidly rotating G dwarfs, indicating that this is not a general characteristic for this type of star.

3. Observations

We use three different kinds of data sets to determine the stability of spotted regions on V889 Her: long-term photometric observations from the Hipparcos mission, and two different time series of high-resolution spectra used for radial velocity (RV) measurements and Doppler imaging. The short-term time series suitable for DI yield snapshots of the spot distribution, which we correlate with our long-term RV measurements covering the same time period. Figure 1 shows the time coverage of the three data sets used in this work.

3.1. Hipparcos data

The Hipparcos satellite obtained a lightcurve of V889 Her during its 3.3 year mission. The available data cover the time between March 1990 and March 1993 with about 150 unevenly sampled photometric data points (Perryman et al. 1997).

3.2. RV measurements

The RV observations were carried out at the 2 m Alfred Jensch Telescope at the Thüringer Landessternwarte in Tautenburg, Germany. It is equipped with a Coudé Echelle spectrograph, which provides a resolving power of $R = 67\,000$ and a wavelength range of 4700–7400 Å. In total, 62 radial velocity shifts were analyzed in this paper. For the purpose of a stable wavelength calibration, an iodine cell was used (Marcy & Butler 1992); for more information about the spectrograph see Hatzes et al. (2005).

Table 2. Nordic Optical Telescope data.

N^a	Observation dates	Julian date^b	Total^c	Used^d
1–4	June 09, 2003	3799.54	42	39^e
	June 12, 2003	3802.75		
9–12	June 16, 2003	3807.47	19	19
	June 20, 2003	3810.69		

^{a} Number of nights; ^{b} JD – JD$_0$ with JD$_0$ = 2 449 000.0 days; ^{c} total number of spectra available; ^{d} number of spectra used for DI; ^{e} three spectra were dismissed due to poor SNR, see Sect. 6.1.

The exposure times vary between 15 and 20 min, the typical signal-to-noise ratio is 70. The data was reduced with the Image Reduction and Analysis Facility (IRAF, Tody 1993). For the RV measurements the spectral range between 5000 Å and 6300 Å is split up into about 130 pieces ("chunks"). RV shifts are determined independently for each wavelength piece, the mean of all pieces yields the radial velocity with its error given as the standard deviation.

For the analysis, the RV curves are split into shorter subintervals. Their exact definitions and an overview of full observation are given in Fig. 6.

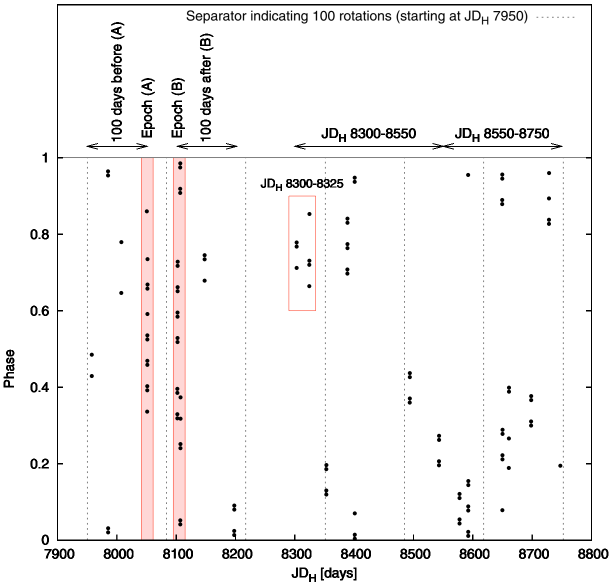

Fig. 2. Time vs. phase diagram (period = 1.3371 days) for the Hipparcos measurements (represented by points). Periods covering 100 rotations are indicated by vertical, dotted lines. Time and phase intervals of special interest are marked by arrows and boxes; see text for more details.

3.3. Doppler imaging spectra

The time series of high-resolution spectra used for Doppler imaging was observed in June 2003 at the Nordic Optical Telescope (NOT) on La Palma. A total of 61 spectra of V889 Her were obtained with the SOFIN Echelle spectrograph mounted at the Cassegrain focus of the 2.56 m telescope, covering several preselected spectral regions between 3750 Å and 11 300 Å with a width of e.g. 60 Å per region around 6000 Å. The average signal-to-noise ratio of these spectra is above 150. The chosen slit width of 65 μ provides a nominal resolving power of 76 000. The data cover 8 nights (2 blocks of 4 consecutive nights), i.e., two full rotations of the star, with a homogeneous phase coverage. Approximately 3 rotations of the star lie between the two obtained Doppler images. The average exposure time for these observations was 20 min. A short summary of the observation dates and the number of spectra is given in Table 2.

The Echelle spectra were reduced with the software package described in Ilyin (2000), performing bias subtraction, master flat field correction, scattered light modeling with bi-cubic splines, and optimum extraction of spectra including cosmic spike rejection. Blaze correction and CCD fringe removal was accomplished using flat field exposures that were reduced in a similar way. The wavelength calibration is based on two Th-Ar spectra taken before and after each object exposure.

4. Lightcurve analysis

4.1. Our modeling approach

Lightcurve modeling has a long-standing history in astronomy. An overview on its history as well as on different approaches towards a solution of this problem can for instance be found in Eker (1994).

The Hipparcos data are of limited accuracy and rather inhomogeneously sampled in time. Therefore, we revert to a simple but robust modeling approach. We subdivide the star into homogeneously spaced longitude intervals, and assume that these areas are homogeneously covered by spots. In the fitting process the relative brightness (spot coverage) of these strips is then varied until the observed lightcurve is matched optimally. We apply two different fit procedures: either we allow fits restricted by a specific assumption about the number of active regions on the stellar surface; in this case each active region is modeled by a longitudinal Gaussian brightness distribution. Or, alternatively, a "free" fit can be carried out, where all surface elements are varied independently.

Note that each individual longitude interval produces the same lightcurve profile (normalized by its intensity, i.e. spot coverage), phase shifted according to its position on the surface. The resulting lightcurve is a linear superposition of the individual contributions. When we use a relatively low number of longitude intervals (say 10), it is obvious that the contributions are linearly independent (given a non pole-on view), and the superposition is uniquely defined. Working with real data, measurement errors and phase coverage limit the uniqueness of the reconstruction; nevertheless, with a low number of longitude intervals, only neighboring intervals show considerable dependence.

In either case latitudinal information is not recovered, which – given the data quality and sampling – would have been an ambitious task.

4.2. Lifetime analysis of structures imprinted on the Hipparcos lightcurve

As demonstrated in Fig. 2, the sampling of the Hipparcos lightcurve is inhomogeneous so that the data contain a number of isolated measurements. Fortunately, there are some observation epochs with much better phase coverage. The first one (A) can be found at JD$_H$[1] ≈ 8050 where we find 12 data points observed during about a day, and the second one (B) is found about 50 days later containing 22 measurements distributed over 5 days

---

[1] JD_H = JD – 2 440 000 days.

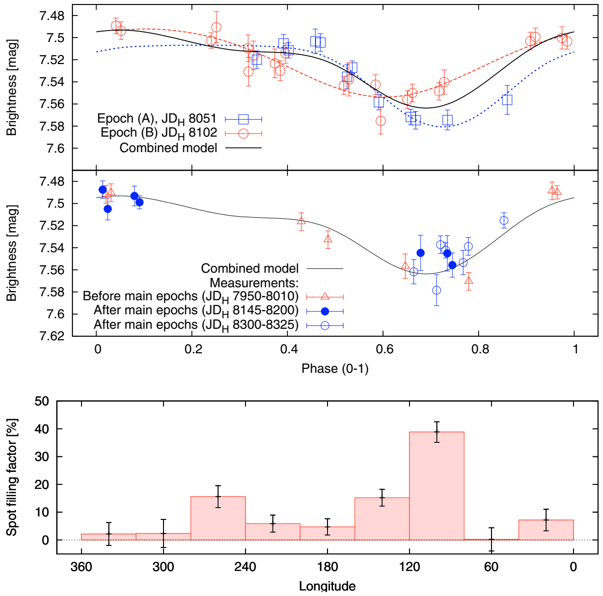

Fig. 3. *Upper panel*: the data and models for observation epoch (A) (squares) and (B) (circles). The dotted and dashed lines indicate model fits obtained for epoch (A) and (B) assuming a surface dominated by one active region. The solid line constitutes a model based on the combined data of epoch (A) and (B). *Middle panel*: the "combined" model from the upper panel as a solid line as well as additional data points observed before and after epochs (A) and (B). *Lower panel*: the spot filling factor obtained from longitude reconstruction. The spot-photosphere contrast was assumed to be 50%. (Note that the error bars do not take into account mutual dependencies of the bins.)

(cf. Fig. 2). The corresponding data points are shown in the upper panel of Fig. 3, where we also present lightcurve reconstructions obtained under the assumption of a single active region on the stellar surface. The measurements originating from epoch (A) cover only phases 0.3–0.9, whereas epoch (B) provides nearly full phase coverage. Clearly, the minimum in interval (A) is sharper than in (B) and also displaced in phase by about 0.1 corresponding to a longitude shift of ≈36° for the activity center. While this shows that there is significant evolution of the lightcurve within 50 days, the lightcurve also maintains its overall appearance showing a pronounced minimum at about 120° longitude as the most distinct feature. The differences between the two epochs can be caused by evolution of the stellar surface and/or by an inappropriate lightcurve folding due to an incorrect rotation period. According to Marsden et al. (2006), V889 Her shows strong differential rotation making its period a function of latitude; folding the data with a period inconsistent with the location of the active regions could mimic surface evolution. Note that adopting a rotation period of 1.3371 ± 0.0002 days, as given by Strassmeier et al. (2003), the relative phase error between two data points separated by 100 rotations is only ≈1.5% so that we can neglect this as an error source here.

In an effort to check how the locations of other, more distant data points compare to the lightcurves obtained during epochs (A) and (B), we combine the two data sets and fit the result using the "free" fit approach with 9 (independent) surface elements (Fig. 3, lower panel). Considering the evolution between epochs (A) and (B), the thus obtained results are time averages rather than snapshots. The fit provides evidence for a pronounced active region at a longitude of about 120° and another less pronounced structure at about 240°.

Now we check statistically whether it is justified to assume that the time averaged model at hand remains an appropriate approximation of the lightcurve over a longer time span (given a period of 1.3371 d). Within about one hundred days (≈75 rotations) before epoch (A) (measurements in $\mathrm{JD_H} = 7950–8010$) there are 3 other observation periods providing 8 additional data points and within about the same time span after epoch (B) (measurements in $\mathrm{JD_H} = 8145–8200$) another 7 measurements are distributed over two observation epochs (see Fig. 2). In the middle panel of Fig. 3 we show the same model lightcurve as before as well as the 15 additional data points (triangles and filled circles). Apparently, the model provides an acceptable description of the observations. Formally, we expect a χ^2 value of 15 ± 5.5 for 15 data points[2] drawn from the same model; the shown model yields 21.2 with about one third of it contributed by a single data point.

If the lightcurve evolves fast with respect to the time span under consideration, we expect the data points to be distributed randomly, and in the following we assume that the lightcurve amplitude observed in epochs (A) and (B) remains representative. From a Monte Carlo simulation we then estimate that the probability of obtaining a value of 21.2 or less for χ^2 from the same number of data points uniformly distributed over the lightcurve amplitude is ≈2.5%. During the simulation we do not vary the data points in phase and all data points enclosed by a single observation epoch are regarded as dependent and, therefore, are varied as a single unit.

We conclude that the Hipparcos lightcurve is compatible with a rotation period of 1.3371 d and a surface configuration dominated by an active region at a longitude of about 120° for at least 50 days and probably up to about 200 days. However, we caution that the data do not allow us to exclude other scenarios.

The middle panel of Fig. 3 includes measurements carried out during the $\mathrm{JD_H} \approx 8300–8325$ time interval (open circles in Fig. 3, also marked in Fig. 2) about 210 days after those of epoch (B). The associated data points confirm the presence of a minimum at about the same position during this period, although their phase coverage is poor. Unfortunately, phase coverage remains a problem throughout the analysis of the rest of the Hipparcos data set. Even if we combine the data obtained during the following ≈450 days ($\mathrm{JD_H} = 8300–8750$), a (connected) phase interval covering about 30% of the lightcurve remains unobserved (see Fig. 2). Furthermore, the measurements are distributed very inhomogeneously in time providing no further well covered individual epochs, forcing us to consider longer time spans.

In the upper panel of Fig. 4 we show the data pertaining to the $\mathrm{JD_H} = 8300–8550$ time interval as well as a "free" model fit obtained from them; note that this covers some data points already shown in the middle panel of Fig. 3. Additionally, we show the lightcurve obtained from combining epochs (A) and (B) (dashed line). As indicated earlier, both lightcurves bear considerable resemblance at phases ≥0.5. This no longer holds for phases ≤0.5, where the data clearly indicate the presence of a second pronounced minimum caused by an active region at a longitude of about 280°. While this stellar region considerably increased its impact on the lightcurve compared to the previous

---

[2] The χ^2 distribution with n degrees of freedom has expectation value n and variance $2n$.

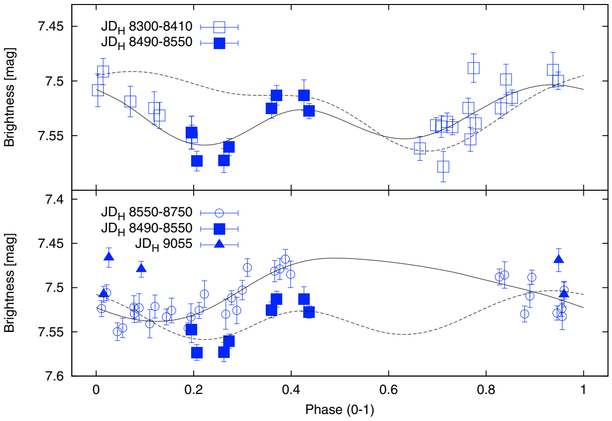

Fig. 4. *Upper panel*: measurements between $JD_H = 8300$ and 8550. The dashed lines indicate the model obtained from the combined epochs (A) and (B), the solid lines show the lightcurve obtained from the given intervals. *Lower panel*: data of the $JD_H = 8490–8750$ time interval and 5 additional points from $JD_H = 9055$.

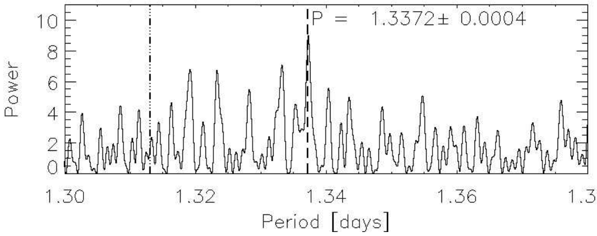

Fig. 5. Periodogram of the RV data on the interval relevant for V889 Her's rotation period. The period determined from the highest peak is given in the figure; Marsden et al.'s value of 1.313 d is marked by the dash-dotted line. See Sect. 5.2 for details.

data, the one at a longitude of ≈120° – although it still exists – is less significant and may be in the process of disintegration.

During the next ≈160 days (see Fig. 4, lower panel), there is a clear evolution in the shape of the lightcurve, potentially indicating evolution of the newly emerged active region. Unfortunately, the phase interval sampling of the lower longitude active region is very poor, so we can no longer trace its evolution. The measurements presented in this panel show a trend indicating an ≈0.05 mag brightening of V889 Her, which may be related to a periodic sinusoidal long-term trend with approximately the correct amplitude and a period of ≈2600 days detected by Strassmeier et al. (2003).

Even though a stellar surface with two dominating active regions evolving in time as indicated by the panels of Fig. 4 seems physically reasonable, we caution that the time span covered here is 450 days, which is twice as long as the time span considered in Fig. 3 and, in particular, 9 times longer than the separation between epochs (A) and (B). Therefore, a variation of the rotation period in the percent regime already has a considerable impact on the lightcurves.

Throughout the above analysis our models yield a spot coverage fraction of ≈10% assuming a spot-photosphere brightness contrast of 1/2. Only during the last observation epochs ($JD_H > 8550$) does the model provide a lower fraction of ≈6%, which may, however, also be related to the poor phase coverage obtained in this time span.

5. Radial velocity measurements

5.1. Activity-related radial velocity measurements

Stellar activity influences the strength and profiles of spectral lines and can, therefore, affect RV measurements, whose precision hinges on symmetric and narrow lines. For example, a spot located on the hemisphere of the star rotating towards the observer diminishes the amount of light contributing to the blue-shifted line wing, leading to an asymmetric line shape. This is not crucial for slowly rotating stars as long as their spectral lines are predominantly broadened by thermal and other mechanisms instead of rotation. Locally restricted surface features only become detectable in very broad lines where the spectra are sufficiently oversampled. In general, slow rotators should be less active, showing fewer and smaller spots, and rotational broadening is less important for their line profiles. For fast rotators with $v\sin(i) \gtrsim 25$ km s^{-1}, where all spectral lines are dominantly broadened by the Doppler effect, such surface features become resolvable in the stellar spectrum.

This is one reason why high accuracy RV measurements are difficult for rapidly rotating stars. Stellar activity can deform their line profiles and, using standard RV detection methods, these deformations lead to RV shifts due to asymmetric and variable line shapes. RV shifts induced by stellar activity can be of the order of several 100 m/s for stars with $v\sin(i) \gtrsim 5$ km s^{-1} (Saar & Donahue 1997; and Saar et al. 1998), and even higher for larger rotation velocities, i.e., up to a factor of a thousand higher than the state-of-the-art RV precision. While this is a problem for companion detections around highly active stars, it can be used as an additional source of information regarding the localization of atmospheric features. RV modulations due to activity can be seen as an activity-induced Rossiter-McLaughlin effect (Ohta et al. 2005) otherwise used for planet detection and characterization: an isolated spot on a stellar surface causes a variation of the RV curve very similar to the one caused by a transiting planet.

Nevertheless, it is a different situation with spots when using the Rossiter-McLaughlin effect. On the one hand it is simpler, if the spot distribution does not change too rapidly, because one usually knows the rotation period of a spotted star and has a chance to observe many spot transits on small time scales for low rotation periods. On the other hand it is more complicated because stellar spot distributions can change on short time scales and, generally, surfaces of active stars are populated by more than only one spot, which means that one measures a superposition of Rossiter-McLaughlin effects for all visible spots. As a result, RV curves modulated by stellar activity generally do not look like the curves derived from planetary transits. They may have complicated structures instead, which cannot be identified as obvious superpositions of Rossiter-McLaughlin effects. However, it is possible to detect an activity-induced effect for simple configurations of spot distributions, as demonstrated in this paper.

5.2. Rotation period

The interpretation of long-term observations requires a precise stellar rotation period. Data sets stretching over periods of months or years must be folded back at a well-known phase scale to be able to detect any long-term stability. In the case of V889 Her this is possible on the basis of extensive photometric observations yielding a rotation period of $P = 1.3371 \pm 0.0002$ days (Strassmeier et al. 2003). Note that we obtain the same value

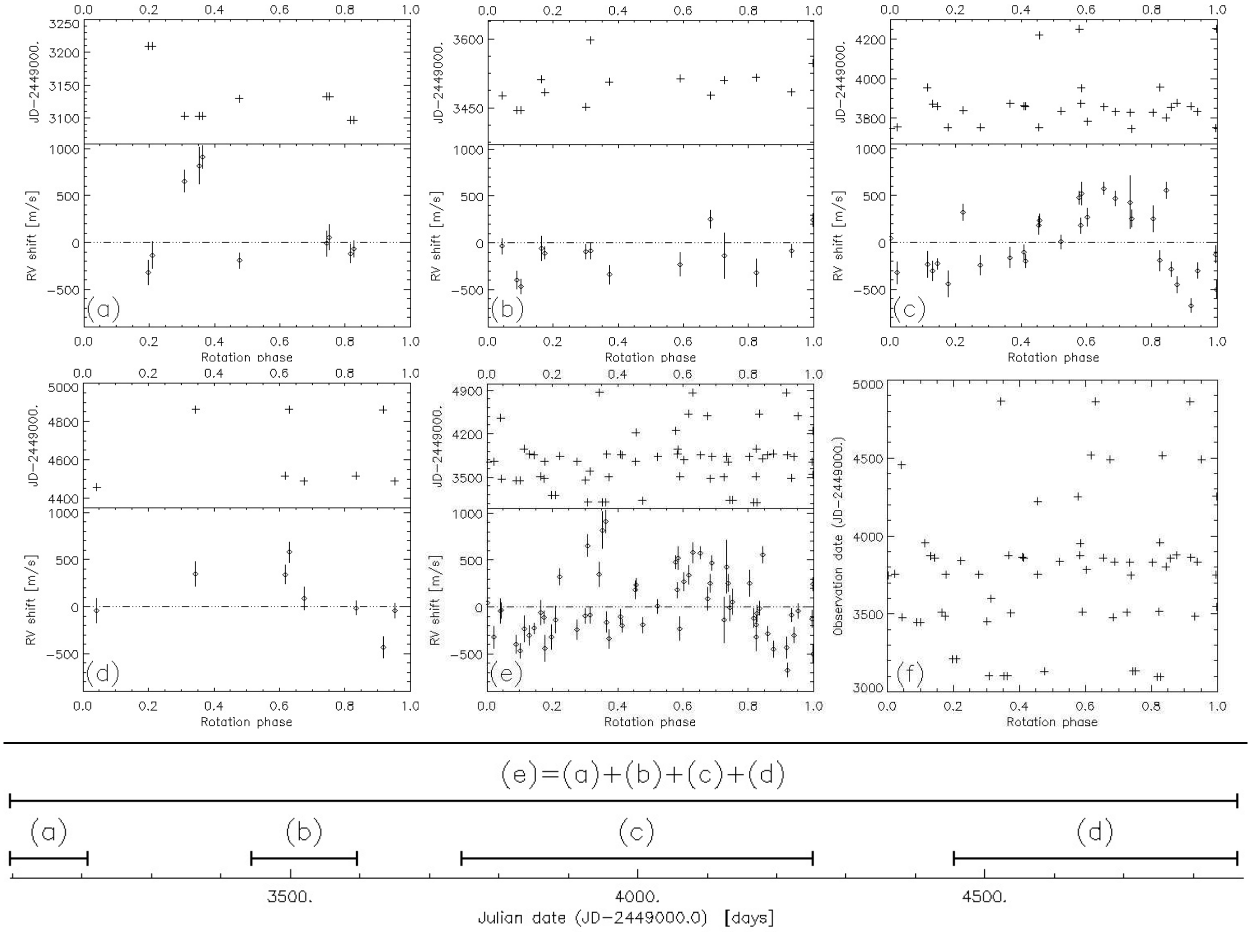

Fig. 6. Radial velocity measurements of V889 Her. The data set was separated into several parts to visualize the stability of structures in the RV curve. Each interval of a few hundred days shows characteristic influences of the star's activity on the spectra causing RV shifts. Large spotted regions are visible in the RV curves for more than a hundred days before they finally dissolve or significantly change position. Panel **f)** shows phase coverage of the entire data set.

from a periodogram of our RV measurements, presented in Fig. 5, where the most significant peak in the relevant period interval is located at $P = 1.3372 \pm 0.0004$ days.

The position of Marsden et al.'s rotation period is marked as well in Fig. 5; clearly, our RV data support the period determined by Strassmeier et al., which we use in the following. This rotation period applies to the case of rigid rotation; since no significant evidence for differential rotation was found in our data sets, we retain the simple model (see Sect. 7).

Given Strassmeier et al.'s error of the rotation period $\Delta P = 0.0002$ days and considering an acceptable phase error of $\Delta\phi = 0.05$ (translating into ≈20°), we can calculate the time span ΔJD that can be phase-folded with the required accuracy. The selected maximum phase error is consistent with longitude accuracies of $\lesssim \pm 10°$ achieved during the modeling of large active regions in the Hipparcos photometry. We use equation

$$\Delta\mathrm{JD} = \left| \left(\frac{1}{P + \Delta P} - \frac{1}{P} \right)^{-1} \cdot \Delta\phi \right|, \quad (1)$$

derived from $\phi + \Delta\phi = \Delta\mathrm{JD}/(P + \Delta P)$, to determine a maximum duration of $\Delta\mathrm{JD} \approx 450$ days for which we can trace a structure in the lightcurve with a phase accuracy better than 0.05.

We use $\mathrm{JD}_0 = 2\,449\,000.0$ to calculate the phases ϕ from

$$\phi = \frac{\mathrm{JD} - \mathrm{JD}_0}{P_{\mathrm{rot}}} \cdot \quad (2)$$

Stellar surface coordinates are defined consistently for all surface maps (see e.g. Fig. 7). Rotation phases are calculated for surfaces rotating towards decreasing longitudes, which means that a phase ϕ can be translated into a longitude l using the equation $\phi = (360° - l)/360°$.

5.3. Detection of stable active regions in the RV curves

The RV measurements of V889 Her cover a time period of almost 2000 days, which translates into approximately 1500 stellar rotations. The distribution of data points over the entire set of observations is given in Fig. 6 panel (f); in panels (a) to (e) we subdivide the data into shorter intervals. The lower panel illustrates the time coverage of each panel.

The modulation of the RV curve does not reveal any stellar companion or extrasolar planet within the limits of its accuracy. There are large quasi-periodic variations in the curve changing on large time scales of several months, which is not

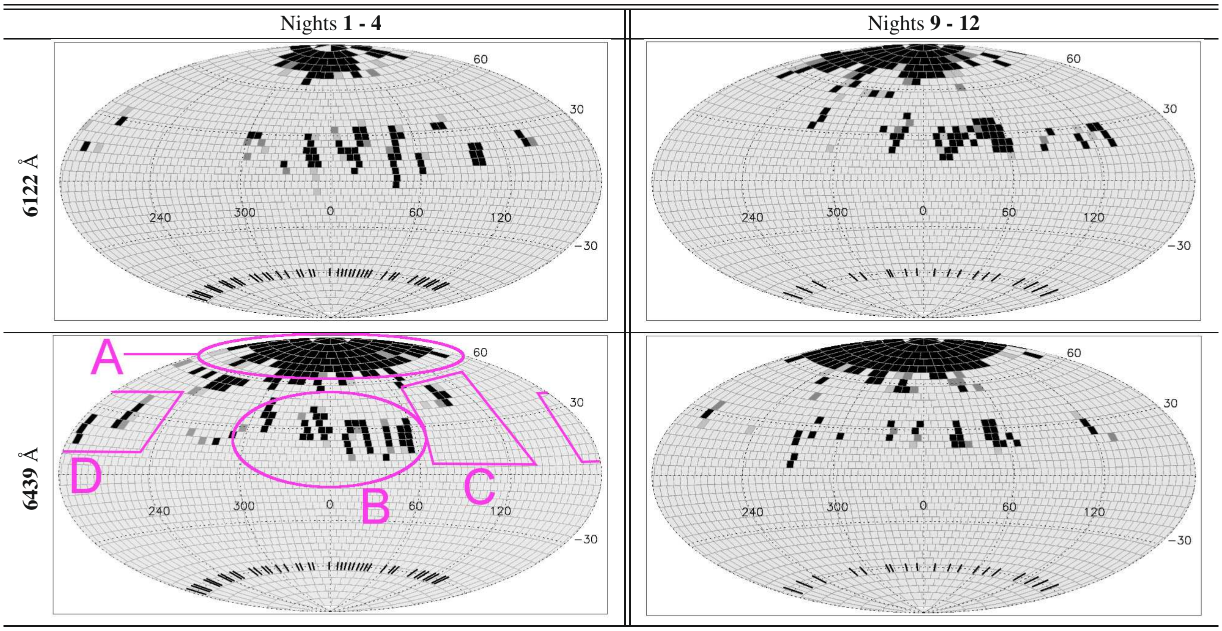

Fig. 7. Doppler images of V889 Her, each observed during three stellar rotations. The images in the left column are separated from the right ones by three rotations. Each row contains images reconstructed from the indicated spectral line. Ticks in the southern hemispheres indicate the observed phases used for the reconstruction. Letters A–D annotate spot regions that can be commonly identified in several reconstructions. See Sects. 6.1 and 6.2 for discussion.

consistent with a low-mass companion. The average accuracy per data point is about 150 m/s.

Nevertheless, we do detect periodicity in the RV curve of Fig. 6. The periodogram of the data shows a high peak at the star's rotation period (cf. Sect. 5.2), which suggests that the modulation of the curve is related to its activity. In Fig. 6 subintervals of the RV data are presented, where the global shape of the curve does not change significantly; however, between the panels substantial changes of the RV curve take place. Panel (c) contains a large fraction of all data points (almost 50%) and clearly shows a stable modulation of the RV curve with rotation for a duration of at least $\gtrsim$150 days (JD = 3750–3900); this time span may even be longer since neighboring points from JD $\approx$ 3950 and $\approx$4250 support the curve as well.

The RV modulation visible in panel (c) dominates the RV curve over the entire time interval, as visible in panel (e) where the phase-folded RV curve of all data points is presented. This is the reason why the periodogram returns the star's exact rotation period, although the spot distribution changes on long time scales. It may not be possible to obtain the rotation period from periodograms of RV curves for a faster changing spot distribution. Its effects on the RV curve will shift in phase and change in amplitude, which is not compensated by regular periodogram algorithms. If the rotation period is known and a sufficiently high phase coverage is available, the data can be subdivided into intervals with stable RV modulations associated with stable global spot distributions.

It is difficult to detect activity-induced Rossiter-McLaughlin effects (see Sect. 5.1) in the other panels of Fig. 6 due to the poorer data sampling. Panel (a) possibly contains some evidence for such a structure but further complementary data, i.e., Doppler images or lightcurves, are necessary to confirm this assumption. Panel (b) does not show any modulation implying that the spot distribution of panel (c) must have formed (or strongly intensified) after JD $\approx$ 3500. There are possibly some signatures of this modulation left in panel (d); the rather poor phase coverage makes it hard to determine to what degree the spot distribution changed.

6. Doppler imaging

Surface inhomogeneities cause deformations of spectral line profiles which can be used to reconstruct the spot distribution. This is achieved by Doppler imaging (DI, Vogt & Penrod 1983). DI is limited to fast rotating stars where the broadening of the spectral lines is dominated by rotational broadening. Given the rotation velocity and period of V889 Her, surface reconstructions of this star can be achieved (cf. Strassmeier et al. 2003; Marsden et al. 2006).

6.1. CLEAN-like Doppler imaging algorithm

For Doppler imaging we use the CLEAN-like algorithm "CLDI" (Wolter 2004; Wolter et al. 2005). Starting with a "standard" line profile adopted for the unspotted star, the program deforms the line profiles using an iteratively constructed stellar surface in order to match the shape of the spectral lines for all observed phases. This is done using "probability maps" that show regions of tentative spot locations (Kürster 1993). These maps do not give a probability in a strict statistical sense, instead they are "backprojections" of the derivations between the observed and reconstructed line profiles onto the stellar surface. Spots are set at the most intense surface element of these backprojections as long as the deviations between the observed and reconstructed line profiles keep decreasing.

Table 3. Absorption lines used for Doppler imaging.

Name	Rest wavelength[a] (Å)	Chemical element
6122	6122.22	Ca I
6439	6439.08	Ca I

[a] From VALD (Vienna Atomic Line Database).

Table 4. Reconstruction parameters adopted for DI.

Parameter	Value
Differential rotation α	0.
Limb darkening ϵ	0.6–0.8
Macro-turbulence[a]	2/12 km s^{-1}
Contrast photosphere/spot	0.5
n_T[b]	4

[a] Probably unphysical since mainly used for line profile adjustments.
[b] Number of intensity levels between darkest and brightest surface elements (“surface temperatures”).

Several parameters must be supplied a priori to the DI process: the rotation period P, the projected rotation velocity $v \sin(i)$, the stellar inclination i, and the linear limb darkening parameter ϵ (with $I_\mathrm{C}/I_\mathrm{C}^0 = 1 - \epsilon + \epsilon \cos\Theta$ where $\cos\Theta$ is the projected distance from the center of the stellar disk in units of the stellar radius, Gray 1992). Table 4 contains the values of these parameters adopted for our DI, additional stellar properties are given in Table 1, while Table 3 lists the lines used for the surface reconstructions.

The Doppler maps are reconstructed in terms of a spot filling factor between 0 (no spot) and 1 (completely spotted) where the number of possible graduations $n_T \geq 2$ must be preselected. Spotted surface elements are areas with lower continuum intensity than the unspotted stellar surface; CLDI does not explicitly determine spot temperatures. We find no differential rotation within our detection limits; reliable small-scale structures close to the pole are barely resolved, preventing the determination of a polar rotation period (see Fig. 7). Reconstructions of the star taken several rotation periods apart do not yield significant identifications of systematically shifted features (see Appendix B, Fig. B.1, for cross-correlation maps). Doppler images calculated using Marsden et al.’s differential rotation law do not improve the χ^2 value. Therefore, we refrain from modifying the rigid rotation law used in our reconstructions. The limb darkening parameter was adjusted for each line to obtain an optimal fit of the standard line profile to the observed lines, resulting in values between $\epsilon = 0.6$ and 0.8.

Based on a comparison of our reconstructions from different spectral lines (Fig. 7), we estimate their surface resolution as approximately 10° corresponding to 2×2 surface elements; a few features are more poorly localized in latitude (e.g. feature C in the left column maps of Fig. 7). Isolated surface elements are not reliably localized; they are an artifact of the CLDI algorithm due to noise and/or short-term spot evolution on small spatial scales.

The estimated reduced χ^2 values of our reconstructions, averaged over all phases, are between 0.3 and 1.5. It is not possible to provide a strictly reduced χ^2, since the number of parameters is not known in the CLEAN-like approach; however, the values are close to 1 and the reconstruction show good agreement with the line profiles (see Appendix C.1).

6.2. Doppler imaging of V889 Her

Figure 7 shows four reconstructed Doppler images of V889 Her. The left column contains the images of the first full rotation, based on spectra of four consecutive nights (“nights 1–4”), i.e. three stellar rotations. The right column shows images of the second full rotation (“nights 9–12”), also taken during three consecutive stellar rotations. Three stellar rotations remained unobserved between the images of the two columns. Table 3 contains details of the lines used for DI.

The left column maps are based on 39 observed rotation phases, quite evenly distributed apart from a gap ranging from about 130° to 180° in surface longitude, while the right column maps are based on 19 phases. The left 6439 Å-map labels the spot regions A–D, that can be commonly identified in several reconstructions. In agreement with previous reconstructions of V889 Her, all our maps show a large polar spot. Causing almost no rotational modulation, the reconstructed size of a polar spot depends sensitively on the adopted line parameters. However, keeping these uncertainties in mind, two properties of the polar spot are reliably found in our reconstructions: it extends down to a latitude of approximately +60° and it apparently exhibits a weak asymmetry, being slightly more pronounced on the 0–180° hemisphere (right half of each map in Fig. 7).

Both the dominant low-latitude feature B and its much smaller companion C persist through all 9 rotations covered by our Doppler maps. They show little distinct evolution apart from a slightly more pronounced gap in the middle of feature B during nights 9–12. The other low-latitude feature (D) disappears between the two observed sequences.

When interpreting Doppler images, one must keep in mind that spots located on the southern hemisphere are largely projected onto the northern hemisphere. Therefore, all given spot latitudes have an unspecified sign. Additionally, surface features based on poor phase coverage have a higher uncertainty and must be judged with care. The latter aspect does not apply to any of the features discussed above.

We conclude that all maps show large spotted regions on poles and low latitudes. Although these features (A–D) seem to be subject to evolution, their change in fine structure is significantly affected by reconstruction uncertainties. However, some spot groups are similar in their large scale structure, especially region B which keeps its character as the “dominant feature” during the observations; this is also visible in the lightcurves and RV-curves of Fig. 8. Within our accuracy limits we do not find evidence of differential rotation: the identified low-latitude surface features do not show a systematic shift in longitude during the observed 9 rotations. Nor does the polar spot or its lower-latitude appendices exhibit well-defined asymmetries, which would be required to measure a differing rotation period for higher latitudes. This justifies our choice of a rigid rotation for the surface reconstruction in agreement with Strassmeier et al. (2003). To obtain significant measurements of V889 Her’s differential rotation, we would need considerably less noisy line profiles to produce Doppler images of better quality.

6.3. RV shifts and lightcurves obtained by Doppler imaging

For our Doppler images we found ourselves in the unusual situation that we had contemporaneous precise and time-resolved RV measurements. In the following we describe how these can be used to obtain activity information and how they can be compared to Doppler maps.

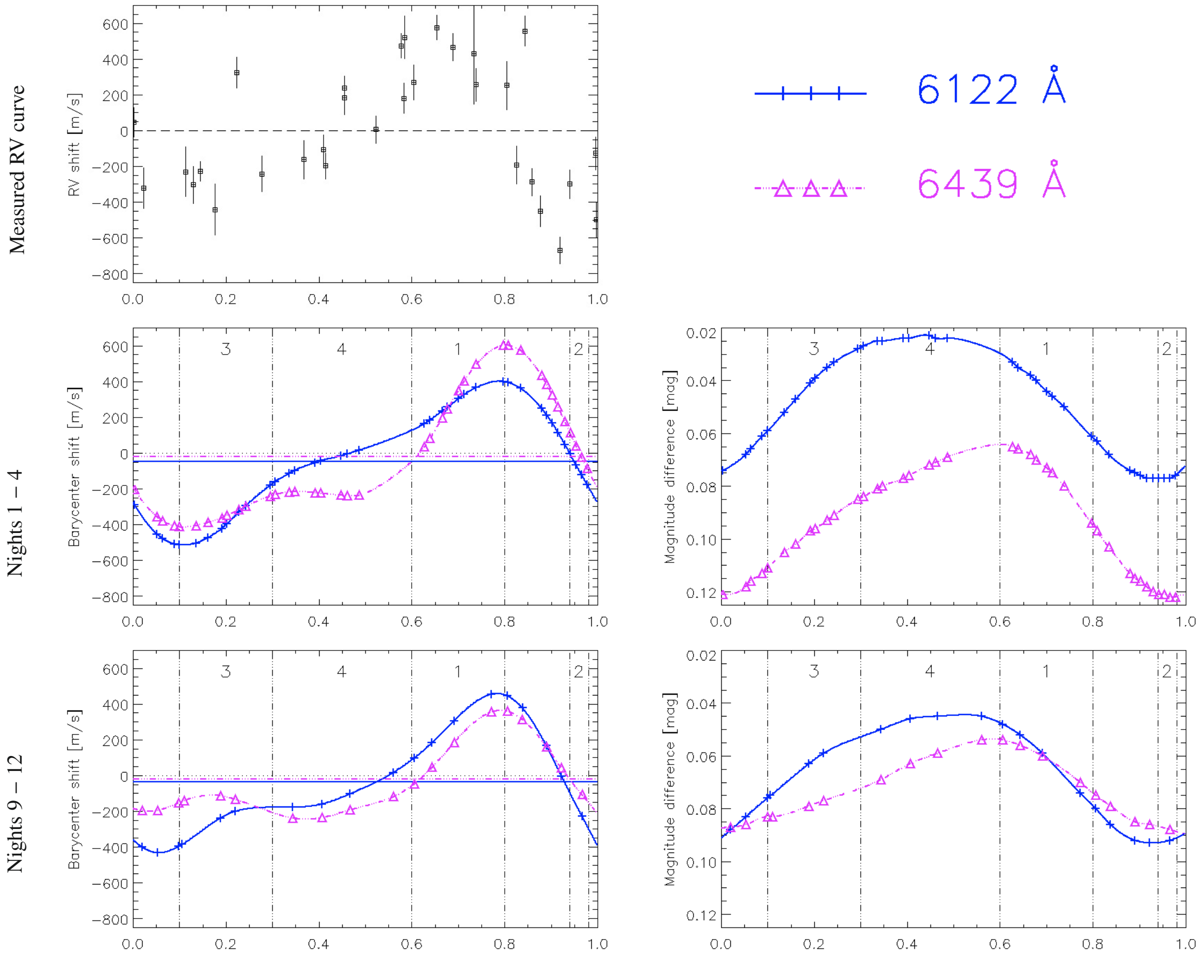

Fig. 8. Line barycenters and lightcurves of V889 Her around $\mathrm{JD}_0 + 4000$. On top the observed RV curve is presented (interval (c) of Fig. 6). *Left column*: line barycenters computed from our DI line profile reconstructions (see Sect. 6.3); they all show an activity-induced Rossiter-McLaughlin effect matching the observations well. *Right column*: lightcurves computed from our Doppler images showing a characteristic correlation with the barycenter modulations. The defined phase intervals 1–4 are used in the discussion of Sect. 6.3.2, see also Fig. 9.

6.3.1. Approach

Asymmetric deformations of a line profile lead to an apparent radial velocity shift of the line. To quantify such profile asymmetries, we define the center of a line profile as its "barycenter": if x is the radial velocity measured in units of $v \sin(i)$ and $y(x)$ is the corresponding (normalized) flux, we can write down the equation

$$S = -\sum_{i=1}^{N} \frac{x_i\, y(x_i)\, \Delta x}{W_{\mathrm{Eq}}} = -\frac{2\, x_{\max}}{N\, W_{\mathrm{Eq}}} \sum_{i=1}^{N} x_i\, y(x_i). \qquad (3)$$

S denotes the barycenter of a line profile in analogy to the barycenter of a system of masses, W_{Eq} is the spectral line's equivalent width, and Δx is the interval between x_i and x_{i+1}. Applying Eq. (3) to our reconstructed line profiles computed from our DI, we obtain a measure for the asymmetry-induced shift of the line center as a function of rotation phase. Note that this is not necessarily the same value as derived in standard RV measurements. Nevertheless, as shown in Fig. 8, in our case both approaches yield similar RV curves for the same object. This similarity encompasses the amplitude and shape of the RV curves. Equation (3) is discussed in detail in Appendix A, see also Ohta et al. (2005).

Although we do not have contemporaneous photometry, we compute lightcurves from our images for two reasons. First, as Fig. 8 illustrates, they facilitate the interpretation of the RV curves. Second, they can be compared *qualitatively* to the Hipparcos lightcurves of Figs. 3 and 4, regarding both amplitude and shape. Using the pre-defined spot continuum flux and limb darkening law, it is straightforward to compute a lightcurve from our Doppler maps. For each rotation phase, a disk-integrated flux f_i is calculated and transformed to magnitudes using $m = -2.5 \log(f_i/f_0)$ with $f_0 = 1$. This results in a magnitude difference $\Delta m = m - m_0$, where m_0 is the integrated flux over the unspotted surface. This procedure has been shown to yield accurate lightcurve fits (Wolter et al. 2008).

6.3.2. Results

We present the lightcurves and line barycenters computed from our Doppler images in Fig. 8. Here, we introduce phase intervals labeled 1 to 4. Each interval represents a characteristic position

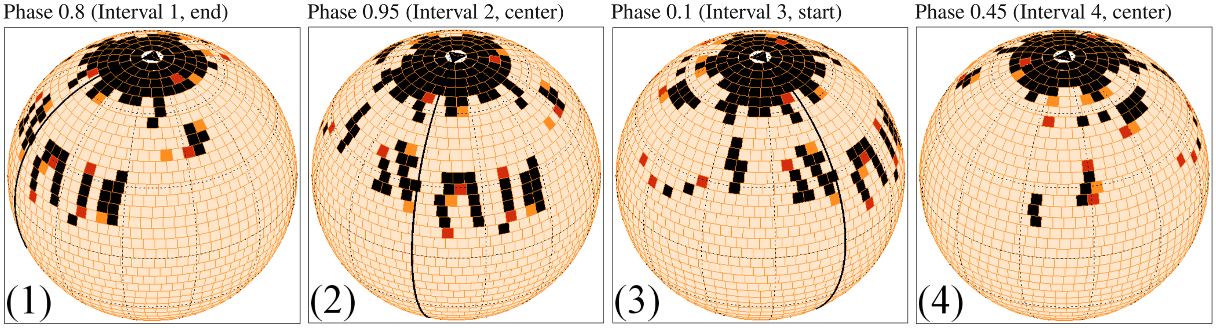

Fig. 9. Doppler image of V889 Her (nights 1–4, 6439 Å line, see Fig. 7) shown at selected phases that serve the discussion of RV curves of Fig. 8. The phase intervals 1 to 4 annotated on top of each panel are defined there. The sequence illustrates the movement of the dominant spot group (region B) across the visible disk: full visibility at the left limb (1), centered on the stellar disk (2), and movement to the right limb (3). In panel (4) the spot group is located at the back side of the star. Qualitatively, the same sequence can be followed in all our Doppler images.

of the dominant spot group on the visible stellar disk. The appearance of the visible disk during these phase intervals is illustrated in Fig. 9.

The RV curve of V889 Her, whose observation time interval encompasses that of our Doppler images, is placed at the top of Fig. 8. It was observed for approximately 500 days, although most data points come from a limited interval of about 150 days (interval (c) of Fig. 6). It shows variations of the measured RV that appear largely stable over the selected time interval with a peak-to-peak amplitude of about 1000 m/s.

All RV curves on the left side of Fig. 8 have a similar shape. Their structure is similar to the one expected from an activity-induced Rossiter-McLaughlin effect (see Sects. 5.1 and 5.3).

Interval 1, starting at about phase 0.6, marks the main increase in S. During this interval the spot region B (containing the dominant feature) appears at the limb of the visible stellar disk. This leads to a decreased absorption in the blue line wing, causing an apparent RV shift towards longer wavelengths. This shift increases while the entire spotted region rotates on the disk, which is illustrated in panel (1) of Fig. 9, then decreases again and finally drops to zero in interval 2, when the spot region B is centered on the stellar disk (panel (2)).

After interval 2, the spot region B moves towards the other edge of the stellar disk and influences the star's redshifted light. The normalized absorption at higher wavelengths is reduced, leading to an apparent RV shift towards lower wavelengths. This shift reaches its maximum when region B is located at the "red" edge of the stellar disk. When spot region B finally moves off the visible disk, the line barycenter returns to zero.

The previous discussion only covered the influence of the large spot feature located at B, which dominates the shape of the RV curves. However, other spotted regions influence the RV curve as well, as can be seen in interval 4; the associated disk appearance is found in panel (4) of Fig. 9. During this phase interval, the dominant feature B is on the back side of the star and does not influence our RV curve. Here, spot group D (cf. Fig. 7) dominates the behavior of the line barycenter as its influence is not masked by the much stronger contribution of spot group B.

Thus, the observed radial velocities (RV curve) and the line barycenters (S curve) show a far-reaching agreement in shape. There is an apparent phase shift of about 0.1 in which the RV curve lags behind the S curves, most pronounced in the position of the maximum. This apparent shift could be due to small-scale variations of the spot pattern during the roughly 100–200 rotations covered by this interval of the RV curve. Alternatively, this shift could be caused by small or low-contrast spot groups not reliably reconstructed in our Doppler maps. Apart from this, the RV and S curves have comparable amplitudes.

In addition to the line barycenters, the right column of Fig. 8 contains the lightcurves computed from our Doppler maps. The rotational evolution discussed above for the RV curves can be followed in the lightcurves; zero passages of the former coincide with extrema of the latter. A more symmetric lightcurve is associated with a spot distribution in longitude that is also more symmetric. Such a spot distribution, in turn, leads to a more symmetric RV curve. This can, for example, be seen when comparing the 6122 Å RV and lightcurves of nights 1–4 and 9–12, respectively.

7. Discussion

Lightcurves, Doppler images and RV measurements represent complementary data sets for the analysis of large-scale surface structures and their temporal evolution. Signatures of activity can be compared and confirmed between them. In accordance with previous authors, our observations show a significant fraction of V889 Her's surface covered with spots. These are primarily concentrated in large regions near the poles and within two active regions at lower latitudes.

The analysis of the Hipparcos photometry (taken between 1990 and 1993) indicates that these active regions were confined to longitudes between 200° to 300° and 80° to 150° for more than two years. Compared to our Doppler images and RV measurements, which show the spot distribution almost 10 years later, we find a qualitatively similar distribution shifted by at least several dozens of degrees in longitude. The center of the dominant feature is located at about 20° longitude. The second active region apparently had much less influence on the RV data; in the Doppler images, where only small signatures of other large spotted regions can be seen, it is located between 150° and 250° longitude. From a global point of view, this is similar to the photometric results.

Concerning the inner structure and shape of active regions, which have a maximum diameter of about 30° to 60°, Doppler images yield information that our lightcurve models cannot contain. The DI surface maps show asymmetrical and inhomogeneous active regions. These should not be confused with the active regions reconstructed in the lightcurve models where primarily information on longitudinal position, and no structure, is obtained. Additionally the latter contain only information averaged over dozens of rotations. This means that the size of an active region represents the temporally averaged area of the star with high activity; its "center" indicates the position with highest activity on average. The quality of our fit clearly indicates that the temporal changes are only minor compared to the depths of the minima, and we show that our models present statistically credible reconstructions of the photometry, even though the poor phase sampling and the long time base of the Hipparcos observations complicate the interpretation of this data set.

Surface reconstructions of V889 Her have been derived by Strassmeier et al. (2003) and Marsden et al. (2006). Their main characteristics do not significantly differ from our Doppler images, showing large polar spots down to almost 60° latitude and a few smaller spots at about 30° latitude. The sizes are comparable as well and lie between about 20° and 30°; the dominant feature of our reconstructions may have a size of almost 60° in diameter (at least in the longitudinal direction), although a possible multi-component structure cannot be ruled out. A closer look reveals some similarity to our lightcurve models. The reconstructions of both authors show dominant surface features at about 300° longitude which roughly agrees with the location of one of our active regions. Unfortunately this is very likely only a coincidence since the long time between the different observations leads to phase errors of about 0.1 to 0.3 due to the rotation period error (see Sect. 5.2). This makes it hard to directly compare the spot positions in different surface maps.

While Marsden et al. (2006) observe differential rotation on this star, in our data sets we do not find any evidence in favor of or against it. The quality of our Doppler imaging data and reconstructions does not allow us to significantly constrain differential rotation, mostly because of their lack of well-defined and asymmetric high-latitude spots. The interpretation of the lightcurves does not require the introduction of differential rotation, although it does not exclude it as well; statistically, a rigid rotation model is sufficient. However, if the strong differential rotation measured by Marsden et al. (2006) also applies to the time span of our RV and photometric data sets, this implies that the dominant spots are confined to a rather narrow latitude band close to about 30° latitude.

To compare the modulation of high-precision RV measurements to spot distributions, we present a method to determine RV shifts from DI line profile reconstructions. In this process the shifted line center of an asymmetric profile is compared to the RV shift derived in standard RV measurement techniques, in our case from iodine cell spectra. Our results show a striking agreement of this method with the conventional RV measurements, not only qualitatively but quantitatively as well. This provides strong empirical evidence that both methods produce equal results. Their differences primarily derive from reconstruction errors of the DI line profiles. An example of a complicated spot distribution causing the superposition of activity-induced Rossiter-McLaughlin effects is presented in this paper. This is only possible due to the availability of Doppler images and contemporaneous high-precision RV measurements.

8. Summary

Using the example of the solar-type, fast rotating star V889 Her, we show that high-accuracy RV measurements can be used to study stellar activity, in particular large-scale spot distributions.

The modulation of V889 Her's RV curve with a period of $P = 1.3372 \pm 0.0004$ days confirms Strassmeier et al.'s rotation period of $P = 1.3371 \pm 0.0002$ days. Our data are consistent with no differential rotation; if present, the spots must be confined to a limited range of latitudes. A large subinterval of the data yields a stable and characteristic RV curve due to an activity-induced Rossiter-McLaughlin effect.

This curve is compared to contemporaneous Doppler images. RV shifts derived from different surface reconstructions match the RV observations, confirming that the observed RV modulation is caused by large-scale and long-term stable spotted regions. This also shows that RV shifts can reliably be determined from line profiles reconstructed in the DI process.

Furthermore we confirm the long-term stability of large-scale surface structures on V889 Her by means of the Hipparcos photometry. Pronounced lightcurve minima preserve their position almost unchanged throughout most of the Hipparcos observations. They are associated with two large active regions located at approximately constant longitude but slowly changing size and latitude.

From our analysis we derive different time scales for structures of different sizes. The evolution of 'small scale' structures inside active regions is not resolved in our data, although the Doppler images indicate that spots of smaller sizes down to approximately 15° occur. In some cases, the size and longitude of active regions remain unchanged for up to 300 days. The global configuration of a polar spot and two large, clearly separated spot groups apparently existed for more than two years; these two spot groups even remained at largely constant longitudes.

Judging from the Doppler images of this paper and those of other authors (Strassmeier et al. 2003, Marsden et al. 2006), the polar spot is likely to be the most persistent surface feature with a lifetime of at least several years. This is also confirmed by the practically constant maximum brightness observed in the Hipparcos photometry.

Acknowledgements. We thank the NOT staff for their excellent support. Many thanks to the services of the *Vienna Atomic Line Database* (VALD). This research has made use of the SIMBAD database, operated at CDS, Strasbourg, France; we appreciate their services very much. K.H. and M.E. are members of the DFG Graduiertenkolleg 1351 *Extrasolar Planets and their Host Stars*. U.W. and S.C. acknowledge DLR support (50OR0105).

Appendix A: Analytic proof of Eq. (3)

In Sect. 6.3 we introduce Eq. (3) for the barycenter of a spectral line, in analogy to the barycenter determination of a system of masses $x_s = (\sum_i x_i\, m_i)/M$, where $M = \sum_i m_i$. We start with the continuous representation of Eq. (3), which reads

$$S = \frac{1}{W_{\rm Eq}} \int_{-x_{\max}}^{+x_{\max}} x \left[1 - y(x - x_{\rm c})\right] {\rm d}x = x_{\rm c}, \tag{A.1}$$

with x denoting the radial velocity axis and $y(x)$ representing the normalized intensity ($0 \leq y \leq 1$). $x_{\rm c}$ is the center position of the line, which we show is equal to the barycenter S. Note that the equivalent width, $W_{\rm Eq} = \int (1 - y(x_i))\,{\rm d}x$, appears by analogy to the total mass, M, here, and we presume it to be constant. The line shape described by $y(x)$ can be arbitrary as long as the integral $\int (1 - y(x_i))\,{\rm d}x$ exists; however, the radial velocity axis must be chosen so that $\int x\,(1 - y(x))\,{\rm d}x = 0$.

Now we aim at proving the correctness of the last equality in Eq. (A.1). Note that with this definition $(1 - y(x))/W_{\rm Eq}$ becomes a distribution function; from the mathematical point of view the integration boundaries may easily be extended to cover an arbitrarily large range, however, in the analysis of real data we usually favor tight boundaries to avoid contamination. Therefore, we explicitly consider them here and, further, restrict ourselves to small shifts, $x_c \ll x_{max}$.

Recasting Eq. (A.1) we obtain

$$S = -\frac{1}{W_{Eq}} \int_{-x_{max}}^{+x_{max}} x\, y(x - x_c)\, dx$$

with the substitution $a = x - x_c$

$$\begin{aligned} S &= -\frac{1}{W_{Eq}} \int_{-x_{max}-x_c}^{+x_{max}-x_c} (a + x_c)\, y(a)\, da \\ &= -\frac{1}{W_{Eq}} \int_{-x_{max}-x_c}^{+x_{max}-x_c} \Big[a\, y(a) \;+\; x_c\, y(a) \Big]\, da. \end{aligned} \qquad (A.2)$$

Above, x_c represents an arbitrarily signed shift of the line's center, which in the following we define as positive without loss of generality.

We discuss the two terms of Eq. (A.2) separately. The first can be treated as follows:

$$-\frac{1}{W_{Eq}} \int_{-x_{max}-x_c}^{+x_{max}-x_c} a\, y(a)\, da \;= \\ -\frac{1}{W_{Eq}} \left(\underbrace{\int_{-x_{max}-x_c}^{-x_{max}+x_c} a\, y(a)\, da}_{\approx\, -2x_c x_{max}} + \underbrace{\int_{-x_{max}+x_c}^{+x_{max}-x_c} a\, y(a)\, da}_{=\,0} \right).$$

In the approximation of the first integral we applied the relation $y(a) \approx 1$, which is valid within the integration interval (x_{max} must be chosen accordingly), and the second integral is zero by definition.

We resume with the second term of Eq. (A.2):

$$\begin{aligned} -\frac{1}{W_{Eq}} \int_{-x_{max}-x_c}^{+x_{max}-x_c} x_c\, y(a)\, da &= -\frac{x_c}{W_{Eq}} \left(2x_{max} - W_{Eq} \right) \\ &= -\frac{2\, x_{max}\, x_c}{W_{Eq}} + x_c. \end{aligned}$$

For the last calculations we use

$$W_{Eq} \approx \int_{-x_{max}-x_c}^{+x_{max}-x_c} \left(1 - y(a) \right) da \;=\; 2x_{max} - \int_{-x_{max}-x_c}^{+x_{max}-x_c} y(a)\, da.$$

Inserting the result into Eq. (A.2), the equation

$$S \;=\; \frac{2\, x_c\, x_{max}}{W_{Eq}} - \frac{2\, x_c\, x_{max}}{W_{Eq}} + x_c \;=\; x_c \;\; \text{q.e.d.} \qquad (A.3)$$

emerges, which is exactly the equality we strove to prove.

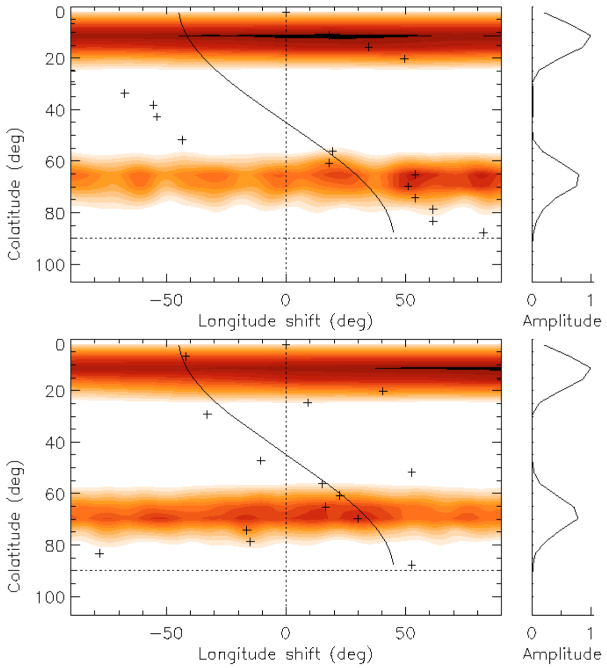

Fig. B.1. Cross-correlation maps comparing the Doppler images of Fig. 7 (*upper panel*) and reconstructions using Marsden et al.'s differential rotation law (*lower panel*). See text for detailed information.

Appendix B: Cross-correlation of Doppler images

Figure B.1 (upper panel) shows the cross-correlation map comparing the Doppler images of Fig. 7, i.e. the reconstructions for nights 1–4 and 9–12 using line 6122 and rigid rotation. For each co-latitude the map shows the cross-correlation, normalized to the overall maximum, obtained when shifting the spots of map 9–12 by the given longitude angle. Darker orange shades indicate larger correlation values. Crosses mark the correlation maximum for each co-latitude; their values are shown in the right-hand graph, also illustrating the assignment of orange hues. For comparison, the smooth, sine-like curve shows the surface shear resulting from Marsden et al.'s differential rotation law.

Figure B.1 (lower panel) shows the same for Doppler images reconstructed adopting Marsden et al.'s differential rotation law. The correlation maps do not support or disprove any specific rotation law.

Appendix C: DI line profile reconstructions

We give the DI line profile reconstructions of all Doppler images presented in Sect. 6.2. Figure C.1 contains the profiles of the 6439 Å (top panels) and the 6122 Å(bottom panels) Ca I lines, 39 phases for nights 1–4 (left column) and 19 phases for nights 9–2 (right column). All lines are continuum normalized but shifted in flux by 0.05 (stacked plot). Rotation phases increase from top to bottom; they are given at the right border. The observed line profiles are shown as vertical lines indicating their observation errors; the DI reconstructions (blue) are overplotted with a straight line. Both are plotted over rotation velocity v_{rad} in units of $v \sin(i)$.

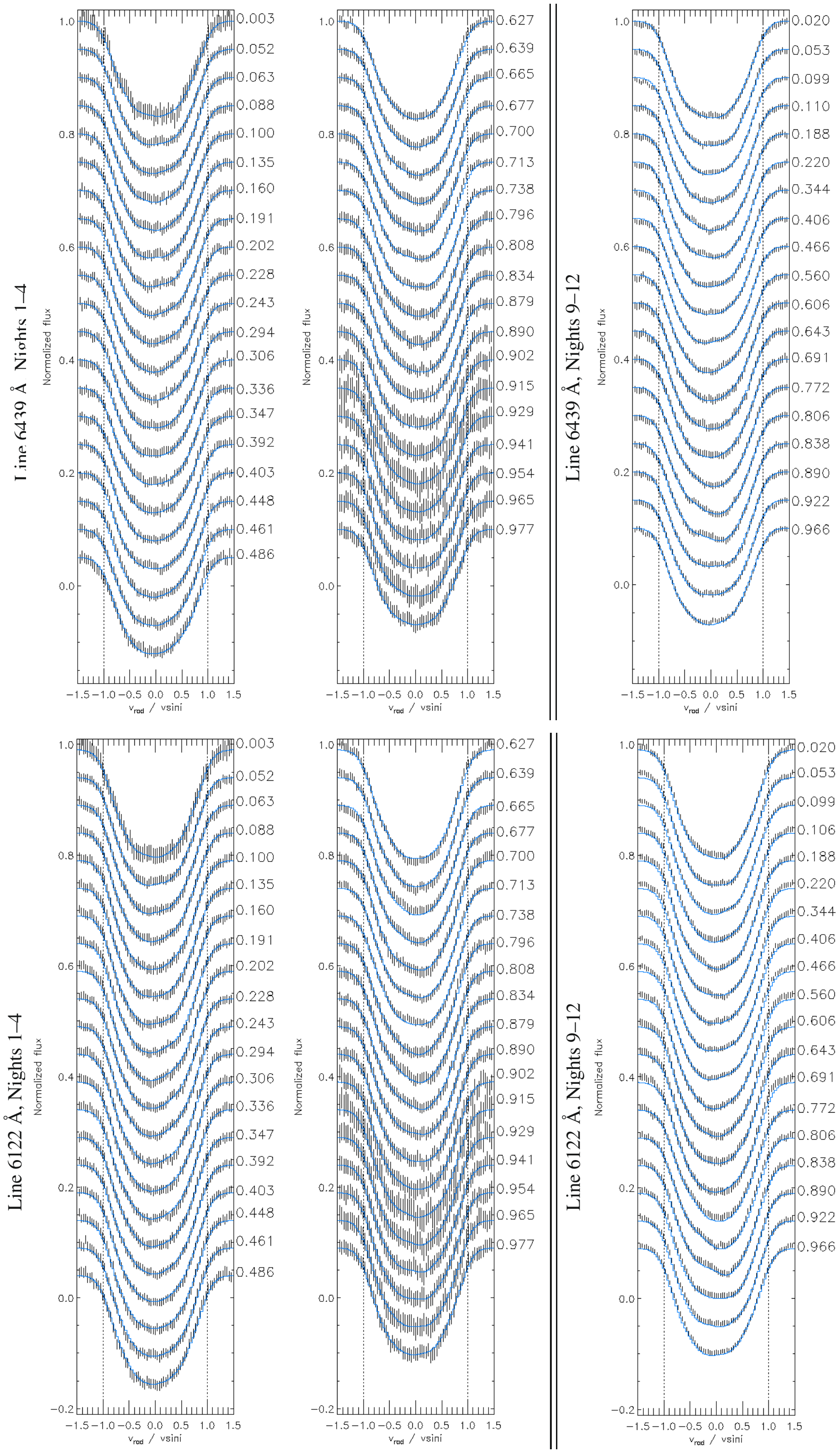

Fig. C.1. Stack plot of all DI line profile reconstructions. *The left column* shows the 39 phases of nights 1–4, *the right column* the 19 phases of the nights 9–12 observations. *The two upper panels* show line 6439 Å, *the two lower panels* show 6122 Å. See Appendix C for more details.

References

Barnes, J. R., Collier Cameron, A., Unruh, Y. C., Donati, J. F., & Hussain, G. A. J. 1998, MNRAS, 299, 904
Berdyugina, S. V. 2007, Mem. Soc. Astron. Ital., 78, 242
Berdyugina, S. V., & Järvinen, S. P. 2005, Astron. Nachr., 326, 283
Donati, J.-F., Cameron, A. C., Semel, M., et al. 2003, MNRAS, 345, 1145
Eker, Z. 1994, ApJ, 420, 373
Gray, D. F. 1992, The observation and analysis o stellar photospheres, 2nd edn., Cambridge Astrophysics Series (New York: Cambridge University Press)
Hatzes, A. P., Guenther, E. W., Endl, M., et al. 2005, A&A, 437, 743
Hendry, P. D., & Mochnacki, S. W. 2000, ApJ, 531, 467
Ilyin, I. V. 2000, Ph.D. Thesis, AA, Astronomy Division Department of Physical Sciences P.O. Box 3000, 90014 University of Oulu, Finland
Jeffers, S. V., Donati, J.-F., & Collier Cameron, A. 2007, MNRAS, 375, 567
Korhonen, H., Berdyugina, S. V., Strassmeier, K. G., & Tuominen, I. 2001, A&A, 379, L30
Korhonen, H., Berdyugina, S. V., Hackman, T., et al. 2007, A&A, 476, 881
Kosovichev, A. G., Bush, R. I., Duvall, T. L., & Scherrer, P. H. 2001, AGU Fall Meeting Abstracts, C730
Kürster, M. 1993, A&A, 274, 851
Lanza, A. F., Piluso, N., Rodonò, M., Messina, S., & Cutispoto, G. 2006, A&A, 455, 595
Li, K. J., Yun, H. S., & Gu, X. M. 2001, AJ, 122, 2115
Marcy, G. W., & Butler, R. P. 1992, PASP, 104, 270
Marsden, S. C., Donati, J.-F., Semel, M., Petit, P., & Carter, B. D. 2006, MNRAS, 370, 468
Ohta, Y., Taruya, A., & Suto, Y. 2005, ApJ, 622, 1118
Perryman, M. A. C., Lindegren, L., Kovalevsky, J., et al. 1997, A&A, 323, L49
Petrovay, K., & van Driel-Gesztelyi, L. 1997, in 1st Advances in Solar Physics Euroconference, Advances in Physics of Sunspots, ed. B. Schmieder, J. C. del Toro Iniesta, & M. Vazquez, ASP Conf. Ser., 118, 145
Saar, S. H., Butler, R. P., & Marcy, G. W. 1998, in Cool Stars, Stellar Systems, and the Sun, ed. R. A. Donahue, & J. A. Bookbinder, ASP Conf. Ser., 154, 1895
Saar, S. H., & Donahue, R. A. 1997, ApJ, 485, 319
Schrijver, C. J. 2002, Astron. Nachr., 323, 157
Solanki, S. K., & Unruh, Y. C. 2004, MNRAS, 348, 307
Strassmeier, K. G., Pichler, T., Weber, M., & Granzer, T. 2003, A&A, 411, 595
Tody, D. 1993, in Astronomical Data Analysis Software and Systems II, ed. R. J. Hanisch, R. J. V. Brissenden, & J. Barnes, ASP Conf. Ser., 52, 173
Vogt, S. S., & Penrod, G. D. 1983, PASP, 95, 565
Vogt, S. S., Hatzes, A. P., Misch, A. A., & Kürster, M. 1999, ApJS, 121, 547
Willis, D. M., & Tulunay, Y. K. 1979, Sol. Phys., 64, 237
Wolter, U. 2004, Ph.D. Thesis, Hamburg
Wolter, U., Schmitt, J. H. M. M., & van Wyk, F. 2005, A&A, 435, 261
Wolter, U., Robrade, J., Schmitt, J. H. M. M., & Ness, J. U. 2008, A&A, 478, L11

Chapter 6

CoRoT-2

6.1 How stellar activity affects the size estimates of extrasolar planets

Authors:

S. Czesla
K. F. Huber
U. Wolter
S. Schröter
J. H. M. M. Schmitt

Published:

Astronomy & Astrophysics, 505, 1277-1282 (2009)

Reproduced with permission ©ESO

A&A 505, 1277–1282 (2009)
DOI: 10.1051/0004-6361/200912454
© ESO 2009

Astronomy & Astrophysics

How stellar activity affects the size estimates of extrasolar planets

S. Czesla, K. F. Huber, U. Wolter, S. Schröter, and J. H. M. M. Schmitt

Hamburger Sternwarte, Universität Hamburg, Gojenbergsweg 112, 21029 Hamburg, Germany
e-mail: `stefan.czesla@hs.uni-hamburg.de`

Received 8 May 2009 / Accepted 1 July 2009

ABSTRACT

Light curves have long been used to study stellar activity and have more recently become a major tool in the field of exoplanet research. We discuss the various ways in which stellar activity can influence transit light curves, and study the effects using the outstanding photometric data of the CoRoT-2 exoplanet system. We report a relation between the "global" light curve and the transit profiles, which turn out to be shallower during high spot coverage on the stellar surface. Furthermore, our analysis reveals a color dependence of the transit light curve compatible with a wavelength-dependent limb darkening law as observed on the Sun. Taking into account activity-related effects, we redetermine the orbit inclination and planetary radius and find the planet to be ≈3% larger than reported previously. Our findings also show that exoplanet research cannot generally ignore the effects of stellar activity.

Key words. techniques: photometric – stars: activity – starspots – stars: individual: CoRoT-2a – planetary systems

1. Introduction

The brightness distribution on the surface of active stars is both spatially inhomogeneous and temporally variable. The state and evolution of the stellar surface structures can be traced by the rotational and secular modulation of the observed photometric light curve. In the field of planet research, light curves including planetary transits are of particular interest, since they hold a wealth of information about both the planet and its host star.

The outstanding quality of the space-based photometry provided by the CoRoT mission (e.g., Auvergne et al. 2009) provides stellar light curves of unprecedented precision, temporal cadence and coverage. While primarily designed as a planet finder, the CoRoT data are also extremely interesting in the context of stellar activity. Lanza et al. (2009) demonstrated the information content to be extracted from these light curves in the specific case of CoRoT-2a. This star is solar-like in mass and radius, but rotates faster at a speed of $v\sin(i) = 11.85 \pm 0.50\ \mathrm{km\,s^{-1}}$ (Bouchy et al. 2008). Its rotation period of ≈4.52 days was deduced from slowly evolving active regions, which dominate the photometric variations. Thus, CoRoT-2a is a very active star by all standards. Even more remarkably, CoRoT-2a is orbited by a giant planet (Alonso et al. 2008), which basically acts as a shutter scanning the surface of CoRoT-2a along a well defined latitudinal band.

The transiting planetary companion provides a key to understanding the surface structure of its host star. While previous analyses have either ignored the transits (Lanza et al. 2009) or the "global" light curve (Wolter et al. 2009), we show that there is a relation between the transit shape and the global light curve, which cannot generally be neglected in extrasolar planet research.

2. Observations and data reduction

Alonso et al. (2008) discovered the planet CoRoT-2b using the photometric CoRoT data (see Table 1). Its host star has a spectral type of G7V with an optical (stellar) companion too close to be resolved by CoRoT. According to Alonso et al. (2008), this secondary contributes a constant (5.6 ± 0.3)% of the total CoRoT-measured flux. CoRoT-2b's orbital period of ≈1.74 days is about one third of CoRoT-2a's rotation period, and the almost continuous CoRoT data span 142 days, sampling about 30 stellar rotations and more than 80 transits. The light curve shows clear evidence of strong activity: there is substantial modulation of the shape on timescales of several days, and the transit profiles are considerably deformed as a consequence of surface inhomogeneities (Wolter et al. 2009).

Our data reduction starts with the results provided by the CoRoT N2 pipeline (`N2_VER` 1.2). CoRoT provides three-band photometry (nominally red, green, and blue), which we extend by a virtual fourth band resulting from the combination (addition) of the other bands. This "white" band is, henceforth, treated as an independent channel, and our analysis will mainly refer to this band. It provides the highest count rates and, more

Table 1. Stellar/planetary parameters of CoRoT-2a/b.

Star[a]	Value ± Error	Ref.[b]
P_s	(4.522 ± 0.024) d	L09
Spectral type	G7V	B08
Planet[c]	Value ± Error	Ref.
P_p	(1.7429964 ± 0.0000017) d	A08
T_c [BJD]	(2454237.53362 ± 0.00014) d	A08
i	(87.84 ± 0.10)°	A08
R_p/R_s	(0.1667 ± 0.0006)	A08
a/R_s	(6.70 ± 0.03)	A08
u_a, u_b	(0.41 ± 0.03), (0.06 ± 0.03)	A08

[a] P_s – stellar rotation period; [b] taken from Lanza et al. (2009) [L09], Alonso et al. (2008) [A08], or Bouchy et al. (2008) [B08]; [c] P_p – orbital period, T_c – central time of first transit, i – orbital inclination, R_p, R_s – planetary and stellar radii, a – semi major axis of planetary orbit, u_a, u_b – linear and quadratic limb darkening coefficients.

Article published by EDP Sciences

importantly, is less susceptible to instrumental effects such as long-term trends and "jumps" present in the individual color channels.

In all bands, we reject those data points flagged as "bad" by the standard CoRoT pipeline (mostly related to the South Atlantic anomaly). The last step leaves obvious outliers in the light curves. To remove them, we estimate the standard deviation of the data point distribution in short (≈3000 s) slices and reject the points more than 3σ off a (local) linear model. Inevitably, we also remove a fraction of physical data (statistical outliers) in this step, but we estimate that loss to be less than a percent of the total number of data points, which we consider acceptable.

In all bands apart from the white, we find photometric discontinuities (jumps), which are caused by particle impact on the CoRoT detector. In the case of CoRoT-2a, the jumps are of minor amplitude compared to the overall count rate level, and we correct them by adjusting the part of the light curve following the jump to the preceding level.

Finally, we correct the CoRoT photometry for systematic, instrumental trends visible in all bands apart from white. To approximate the instrumental trend, we fit the (entire) light curve with a second order polynomial, q, and apply the equation

$$c_{\mathrm{corr},i} = c_{\mathrm{o},i} \cdot \frac{\overline{c}}{q_i}, \qquad (1)$$

where $c_{\mathrm{o},i}$ is the ith observed data point, q_i is the associated value of the best-fit second order polynomial, $\overline{c}$ represents the mean of all observed count rates in the band, and $c_{\mathrm{corr},i}$ the corrected photometry.

The resulting light curve still shows a periodic signal clearly related to the orbital motion of the CoRoT satellite. This is again a minor effect in the white band, and we neglect this in the context of the following analysis.

In a last step, we subtract 5.6% of the median light curve level to account for the companion contribution. We use the same rule for all bands, which is only an approximation because, as Alonso et al. (2008) point out, the companion has a later type (probably K or M) and, therefore, a different spectrum from CoRoT-2a.

3. Analysis

3.1. Transit profiles and stellar activity

A planet crossing the stellar disk imprints a characteristic transit feature on the light curve of the star (e.g., Pont et al. 2007; Wolter et al. 2009). The exact profile is determined by planetary parameters as well as the structure of the stellar surface. A model that describes the transit profile must account for both. One of the key parameters of the surface model is the limb darkening law. The presence of limb darkening seriously complicates transit modeling, because it can considerably affect the transit profile, while it is difficult to recover its characteristics from light curve analyses (e.g., Winn 2009).

Stellar activity adds yet another dimension of complexity to the problem, because a (potentially evolving) surface brightness distribution also affects the transit profiles. The local brightness on the surface can either be decreased by dark spots or increased by bright faculae compared to the undisturbed photosphere. Spots (or faculae) located within the eclipsed section of the stellar surface lead to a decrease (increase) in the transit depth, and the true profile depends on the distribution of those structures across the planetary path. Spots and faculae located on the non-eclipsed section of the surface do not directly affect the transit profile but change the overall level of the light curve. As transit light curves are, however, usually normalized with respect to the count rate level immediately before and after the transit, the non-eclipsed spot contribution enters (or can enter) the resulting curve as a time-dependent modulation of the normalized transit depth.

3.2. Transit light-curve normalization

As mentioned above, the normalization may affect the shape of the transit profiles. We now discuss two normalization approaches and compare their effect on the transit profiles. We define f_i to be the measured flux in time bin i, n_i an estimate of the count rate level without the transit (henceforth referred to as the "local continuum"), and p a measure of the unspotted photospheric level in the light curve, i.e., the count rate obtained in the respective band, when the star shows a purely photospheric surface. Usually, the quantity

$$y_i = f_i/n_i \qquad (2)$$

is referred to as the "normalized flux".

If we normalize the flux according to Eq. (2), we may produce variations in the transit light-curve depth in response to non-uniform surface flux distributions as encountered on active stars. To demonstrate this, we assume that a planet transits its host star twice. During the first transit, the stellar surface remains free of spots, but during the second transit there is a large active region on any part of the star not covered by the planetary disk (but visible). Consequently, the local continuum estimate, n_i, for the second transit is lower, and the normalized transit appears deeper, although it is exactly the same transit in absolute (non-normalized) numbers.

To overcome this shortcoming, we define the alternative normalization to be

$$z_i = \frac{f_i - n_i}{p} + 1. \qquad (3)$$

In both cases, the transit light curve is normalized with respect to the local continuum either by division or subtraction. The conceptual difference lies in the treatment of the local continuum level and how it enters the normalized transit light curve. Using Eq. (3), the observed transit is shifted, normalized by a constant, and shifted again. While the scaling in this case remains the same for all transits, the scaling applied in Eq. (2) is a function of the local continuum.

Following the above example, we assume that the same transit can be normalized by using Eqs. (2) and (3). To evaluate the differences between the approaches, we consider the expression

$$\frac{z_i}{y_i} = \frac{(f_i - n_i)/p + 1}{f_i/n_i} \geq 1\,. \qquad (4)$$

For $n_i = p$, Eq. (4) holds as a strict equality, i.e., both normalizations yield identical results. The inequality equates to true, if $p > n_i$ and $n_i > f_i$. The first condition reflects that the local continuum estimate should not exceed the photospheric light-curve level, and the second one says that the light-curve level is below the local continuum. The second condition is naturally fulfilled during a transit, and the first is also met as long as faculae do not dominate over the dark spots during the transit. In the case of CoRoT-2a, Lanza et al. (2009) find no evidence of a significant flux contribution due to faculae, so that we conclude that the normalized transit obtained using Eq. (3) is always shallower than that resulting from Eq. (2), unless $n_i = p$, in which case the outcomes are equal.

3.2.1. Quantifying the normalization induced difference in transit depth

We now study a single transit and consider data points covered by index set j, for which the term $n_j - f_j$ reaches a maximal value of T_0 at some index value $j = T$. At this position, the normalization obtained from Eq. (3) is given by $z_T = (f_T - n_T)/p + 1 = -T_0/p + 1$, whereas Eq. (2) yields $y_T = f_T/n_T = (n_T - T_0)/n_T$. These values are now used to compare the transit depths provided by the two normalizations. We note that we assume that the normalized depth is maximal at index T; this is always true for Eq. (3), but not necessarily for Eq. (2), a point that we assume to be a minor issue. We again find that $z_T = y_T$ if $n_T = p$. If, however, the local continuum estimate is given by $n_T \approx \alpha p$ ($\alpha \leq 1$), the results differ by

$$z_T - y_T = T_0 p^{-1} \left(\alpha^{-1} - 1\right) . \tag{5}$$

Using the extreme values observed for CoRoT-2a ($\alpha \approx 0.96$ and $T_0 \approx 0.03 \times p$), the right-hand side of Eq. (5) yields $\approx 1.3 \times 10^{-3}$ for the difference in transit depth, caused exclusively by applying two different normalization prescriptions.

3.2.2. Which normalization should be used?

For planetary research it is important to "clean" the transit light curves of stellar activity before deriving the "undisturbed" profile associated with the planet *only*. Since transit light curves normalized using Eq. (3) are all scaled using the same factor, they preserve their shape and depth (at least relative to each other) and can, therefore, be combined consistently, which is not necessarily the case when Eq. (2) is used. This does not mean that the obtained transit depth is necessarily the "true" depth, because Eq. (3) includes the photospheric brightness level, p, as a time-independent scaling factor. At least in the context of the light-curve analysis, p cannot be determined with certainty since the star may not show an undisturbed surface during the observation, which may actually never be shown.

A problem evident in CoRoT light-curve analyses is the existence of long-term instrumental gradients in the data (cf. Sect. 2). By modeling these trends with a "sliding" response, R_d, of the detector, so that the relation between "true" photometry, c_i, and observation, $c_{\mathrm{o},i}$, is given by $c_{i,\mathrm{o}} = c_i \cdot R_{\mathrm{d},i}$, we find that Eq. (1) yields

$$c_{\mathrm{corr},i} = c_i \cdot \left(R_{\mathrm{d},i} \frac{\overline{c}}{q_i}\right) . \tag{6}$$

Obviously, the true photometry is recovered when the embraced term equates to one. However, the scaling of $\overline{c}$ in Eq. (1) is arbitrary, so that this is not necessarily the case. As long as q_i, however, appropriately represents the shape of $R_{\mathrm{d},i}$, the term provides a global scaling, which cancels out in both of the Eqs. (2) and (3).

For our transit analysis, we argue in favor of the normalization along Eq. (3). We estimate the photospheric level from the highest count rate during the most prominent global maximum (at JD $\approx$ 2 454 373.3) in each individual band. These estimates are based on the reduced light curves; in particular, we have accounted for both the instrumental trend and the stellar companion. Throughout our analysis, we use the values p_white = 703 000, p_red = 489 000, p_green = 88 500, and p_blue = 124 500 (in units of e^-/32s). Since even at that time, spots are likely to have been present on the stellar disk, these estimates might represent lower limits to the true value of p.

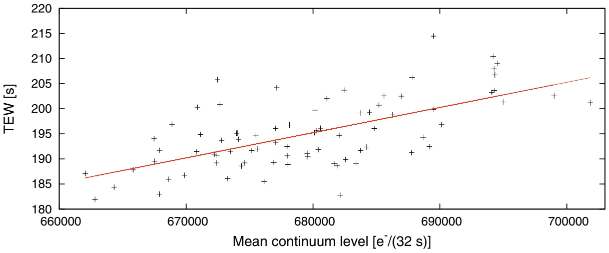

Fig. 1. Transit equivalent width (TEW) versus transit continuum level as well as the best-fit linear model.

3.3. Transit profiles in CoRoT-2a

The global light curve of CoRoT-2a shows pronounced maxima and minima and a temporally variable amplitude of the global modulation (Alonso et al. 2008). It is natural to expect the spot coverage on the eclipsed section of the stellar surface to be smallest where the global light curve is found at a high level, and transit events occurring during those phases should, thus, be least contaminated with the effects of stellar activity. The opposite should be true for transits during low light-curve levels.

To quantify the impact of activity on the transit profile, we define the transit equivalent width (TEW) of transit n

$$TEW_n = \int_{t_I}^{t_{IV}} \left(1 - z_n(t)\right)\mathrm{d}t \approx \sum_i (1 - z_{n,i})\delta t_i, \tag{7}$$

where t_I and t_{IV} must be chosen so that they enclose the entire transit. Extending the integration boundaries beyond the true extent of the transit does not change the expectation value of Eq. (7), but only introduces an extra amount of error. The nominal unit of the TEW is time.

3.3.1. The relation between transit equivalent width and global light-curve modulation

As outlined above, we expect activity to have greater impact when the overall light-curve level is low. When this is true, it should be reflected by a relation between the transit equivalent width and the transit continuum level (the overall light-curve level at transit time).

In Fig. 1, we show the distribution of TEWs as a function of the local continuum level for all 79 transits observed with a 32 s sampling. There is a clear tendency for larger TEWs to be associated with higher continuum levels, thus, providing obvious evidence of activity-shaped transit light curves. In the same figure, we also show the best-fit linear model relation, which has a gradient of d(TEW)/d(CL) = $(5 \pm 1.5) \times 10^{-4}$ s/(e^-32 s).

To corroborate the reality of the above stated correlation, we calculated the correlation coefficient, R. Its value of $R = 0.642$ confirms the visual impression of a large scatter in the distribution of data points (cf., Fig. 1). We estimate the statistical error for a single data point to be $\approx$0.1%, so that the scatter cannot be explained by measurement errors. To check whether the continuum level and the TEW are independent variables, we employ a t-test and find the null hypothesis (independent quantities) to be rejected with an error probability of 1.8×10^{-10}, so that the correlation between the TEWs and the continuum level must be regarded as highly significant.

As a cross-check of the interpretation of this finding, we also investigated the distribution of TEWs against time, which shows no such linear relation ($R = 0.110$). Therefore, we argue that the

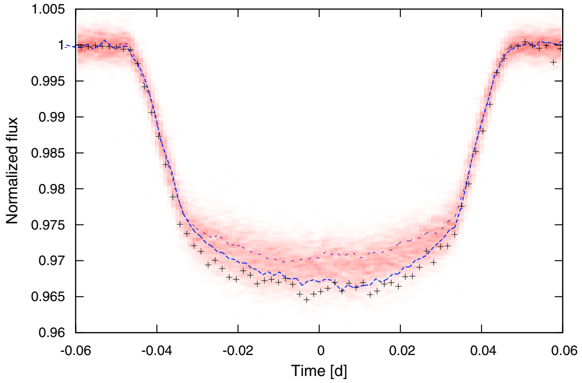

Fig. 2. Average transit light curves obtained by combining the ten profiles exhibiting the highest (thick dashes) and lowest (thin dashes) continuum levels. The crosses indicate our lower envelope estimate and the color gradient (red) illustrates the distribution of data points for all available transits.

effect is not instrumental or caused by our data reduction, but physical.

3.4. Comparing high and low continuum level transits

Since activity is evident in the profiles of the transit light curves, we further investigate its effect by comparing the most and least affected transit light curves. Therefore, we average the ten transits with the highest continuum levels (No. 3, 16, 42, 47, 50, 55, 68, 73, 76, and 81) and compare the result to an average of the ten transits with the lowest continuum level (No. 15, 23, 35, 40, 43, 69, 72, 75, 77, and 80). In Fig. 2, we show the two averages as well as our computed lower envelope (see Sect. 3.5) superimposed on the entire set of folded photometry data points. The distribution of the entire set is denoted by a color gradient (red) with stronger color indicating a stronger concentration of data points. The curve obtained from the transits at a "low continuum state" is clearly shallower, as was already indicated by the TEW distribution presented in Fig. 1.

The difference in TEW amounts to ≈15.5 s in this extreme case. We checked the significance of this number with a Monte Carlo approach. On the basis of 20 randomly chosen transits, we constructed two averaged light curves using 10 transits for each and calculated the difference in TEW. Among 1000 trials, we did not find a single pair with a difference beyond 12 s, so that the result is not likely to be caused by an accidental coincidence.

3.5. Obtaining a lower envelope to the transit profiles

As was demonstrated in the preceding section, activity shapes the transit light curves, and we cannot exclude that every transit is affected so that a priori no individual profile can be used as a template representing the "undisturbed" light curve. The distortion of the individual profiles is, however, not completely random, but the sign of the induced deviation is known as long as we assume that the dark structures dominate over bright faculae, which seems justified for CoRoT-2a (Lanza et al. 2009). In this case, activity always tends to raise the light-curve level and, thus, decreases the transit depth. Therefore, the most suitable model of the undisturbed profile can be estimated to be a lower envelope to the observed transit profiles.

We take a set of N_T transit observations and fold the associated photometry at a single transit interval, providing us with the set $LC_{T,i}$ of transit data points. If the lower envelope were already among the set of observed transits, it would in principle look like every other light curve. In particular, it shows the same amount of intrinsic scattering (not including activity), characterized by the variance σ_0^2.

We estimate the variance to be

$$\sigma_0^2 \approx \frac{1}{N} \sum_j^N (LC_{T,j} - \mu_j)^2, \tag{8}$$

where μ_j is the (unknown) expectation value and N is the number of data points. The aim of the following effort is to identify the lowest conceivable curve sharing the same variance. To achieve this, we divide the transit span into a number of subintervals, each containing a subsample, s, of LC_T. The distribution of data points in s is now approximated by a "local model", $lm(\gamma)$, with a free normalization γ; lm can for instance be a constant or a gradient. Given lm, we adapt the normalization to solve the equation

$$\left| \left(\frac{\sum_s (LC_s - lm(\gamma))^2 \cdot H(lm(\gamma) - LC_s)}{\sum_s H(lm(\gamma) - LC_s)} - \sigma_0^2 \right) \right| = 0, \tag{9}$$

where H denotes the Heaviside function ($H(x) = 1$ for $x > 0$, and $H(x) = 0$ otherwise). In this way, we search for the local model compatible with the known variance of the lower envelope. The ratio on the left-hand side of Eq. (9) represents a variance estimator exclusively based on data points below the local model. It increases (strictly) monotonically except for the values of γ, where the local model "crosses" a data point and the denominator increases by one instantaneously. Therefore, there may be more than one solution to Eq. (9). From the mathematical point of view, all solutions are equivalent, but for a conservative estimate of the lower envelope the largest one should be used.

In Fig. 2, we show the lower envelope, which is in far closer agreement with the average of the high continuum transit profiles than with its low continuum counterpart. The derivation of the lower envelope is based on Eq. (9). To obtain an estimate of σ_0^2, we fitted a 500 s long span within the transit flanks (3500 ± 250 s from the transit center), where activity has little effect, with a straight line and calculated the variance with respect to this model. The resulting value (using normalized flux) of $\sigma_0^2 = 1.6 \times 10^{-6}$ was adopted in the calculation. Furthermore, we chose a bin width of 150 s, and the "local model" was defined as a regression line within a ±100 s time span around the bin center. Additionally, we postulated that at least 8 (out of ≈350) data points per bin should be located below the envelope, which improved the stability of the method to the effect of outliers but has otherwise little impact.

3.6. Transit profiles in different color channels

CoRoT observes in three different bands termed "red", "green", and "blue". In the following, we present a qualitative analysis of the transit profiles in the separate bands. In the case of CoRoT-2a, approximately 70% of the flux is observed in the red band, and the remaining 30% is more or less equally distributed among the green and blue channels. To compare the profiles, we average all available transits in each band individually and normalize the results with respect to their TEW, i.e., after this step they all have the same TEW. The resulting profiles represent the curves that would be obtained if the stellar flux integrated along the planetary path was the same in all bands.

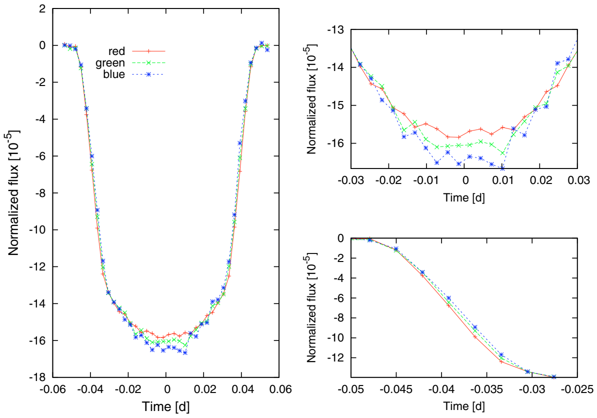

Fig. 3. *Left panel*: normalized transit in the three CoRoT bands red, green, and blue obtained by averaging all available data. *Upper right*: close-up of the transit center. Lower right: close-up of the ingress flank of the transit.

In Fig. 3, we show the transit light curves normalized in this way (TEW=1) obtained in the three bands.

The normalized transits show a difference in both their flank profile and their depth. The blue and green transit profiles are both narrower than the red one, and deeper at the center. This behavior is most pronounced in the blue band, so that the green transit light curve virtually always lies in-between the curves obtained in red and blue.

The behavior described above can be explained by a color-dependent limb darkening law, with stronger limb darkening at shorter wavelengths as predicted by atmospheric models (Claret 2004) and observed on the Sun (Pierce & Slaughter 1977). We checked that analytical transit models (Pál 2008) generated for a set of limb darkening coefficients, indeed, reproduce the observed behavior when normalized with respect to their TEW.

Normalizing the averaged transits not with respect to TEW but using Eq. (3) yields approximately the same depth in all bands, while the difference in the flanks becomes more pronounced. The reason for this could be an incorrect relative normalization, which can e.g., occur if the eclipsed section of the star is (on average) redder than the remainder of the surface because of pronounced activity or gravity darkening, or it may be a relic of an inappropriate treatment of the companion's flux contribution. Whatever the explanation, it is clear from Fig. 3 that the flanks and centers in the individual bands cannot be reconciled simultaneously by a renormalization. Therefore, our analysis shows that the transit light curves are color dependent.

4. Stellar activity and planetary parameters

The preceding discussion shows that stellar activity has a considerable influence on the profile of the transit light curves, and the derivation of the planetary parameters will therefore also be affected. We now determine the radius and the orbit inclination of CoRoT-2b taking activity into account, and discuss the remaining uncertainties in the modeling.

4.1. Deriving the planetary radius and inclination from the lower envelope profile

In the analysis presented by Alonso et al. (2008), the fit to the planetary parameters is based on the average of 78 transit light curves (see Table 1 for an excerpt of their results). While this yields a good approximation, the results still include a contribution of stellar activity, and an undisturbed transit is needed to calculate "clean" planetary parameters.

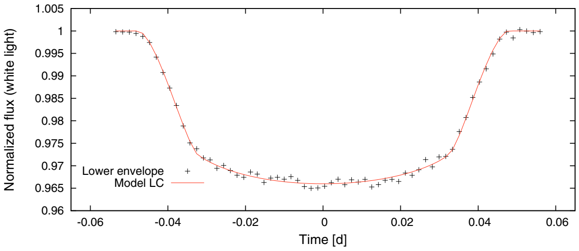

Fig. 4. Lower envelope of all normalized transit light curves (already shown in Fig. 2) and our model fit.

We follow a simplified approach to estimate the impact of activity on the planetary parameters. In particular, we use the lower envelope derived in Sect. 3.4 as the most suitable available model for the undisturbed transit. Starting from the results reported by Alonso et al. (2008), we reiterate the fit of the planetary parameters. In our approach, we fix the parameters of transit timing, i.e., the semi-major axis and stellar radius, and the limb darkening coefficients at the values given by Alonso et al. (2008) (cf. Table 1). The two free parameters are the planetary radius and its inclination.

We note that limb darkening coefficients recovered by light curve analyses are not reliable, especially when more than one coefficient is fitted (e.g., Winn 2009). However, since an accurate calibration of the CoRoT color bands is not yet available and the coefficients determined by Alonso et al. (2008) roughly correspond to numbers predicted by stellar atmosphere models[1], we decided to use the Alonso et al. values, which also simplifies the comparison of the results.

For the fit, we use the analytical models given by Pál (2008) in combination with a Nelder-Mead simplex algorithm (e.g., Press et al. 1992).

The result of our modeling is illustrated in Fig. 4. The most probable radius ratio is $R_p/R_s = 0.172 \pm 0.001$ at an inclination of 87.7° ± 0.2°. The quoted errors are statistical errors and only valid in the context of the model. These numbers should be compared with the values $R_p/R_s = 0.1667 \pm 0.0006$ and 87.84° ± 0.1° (cf., Table 1) derived without taking activity effects into account. The best-fit model inclination is compatible with the value determined by Alonso et al. (2008), but "our" planet is larger by ≈3%. The planet's size depends mainly on the transit depth, which is, indeed, affected at about this level by both normalization (Sect. 3.2.1) and stellar activity (Sect. 3.4).

Clearly, the derived change in R_p/R_s of 0.005 is much larger than the statistical error obtained from light-curve fitting, and, therefore, the neglect of activity leads to systematic errors in excess of statistical errors. While the overall effect in planet radius is ≈3%, the error in density becomes ≈10%. These errors are certainly tolerable for modeling planetary mass-radius relationships, but they are unacceptable for precision measurements of possible orbit changes in these systems.

---

[1] For $T_{\rm eff} = 5600$ K and $\log(g) = 4.5$, the PHOENIX models given by Claret (2004) yield quadratic limb darkening coefficients of $u_a = 0.46$ and $u_b = 0.25$ in the Sloan-r' band.

4.1.1. Planetary parameters and photospheric level

As already indicated the normalization according to Eq. (3) relies on a “photospheric light-curve level”, p, which enters as a global scaling factor and, therefore, also impedes the constraint of the planet’s properties.

In a simple case, the star appears as a sphere with a purely photospheric surface, and the observed transit depth, f_0, can be identified with the square of the ratio of the planetary to the stellar radius

$$f = \frac{\max(n_i - f_i)}{p} = \left(\frac{R_\mathrm{p}}{R_*}\right)^2 L_\mathrm{d}, \tag{10}$$

where L_d is a correction factor that accounts for limb darkening. However, when the observed star is active and the light curve is variable, there is no guarantee that the maximum point in the observed photometry is an appropriate representation of the photospheric stellar luminosity. Persistent inhomogeneities, such as polar spots and long-lived spot contributions, modulate the light curve, so that the pure photosphere might only be visible anytime the star is not observed or possibly never.

Assume our estimate, p_m, of the photospheric level underestimates the true value, p, by a factor of $0 < c \leq 1$ so that $p_\mathrm{m} = p \cdot c$ and $f_{le,i}$ denotes the lower envelope transit light curve. The measured transit depth, f_m, then becomes

$$f_\mathrm{m} = \frac{\max(n_i - f_{le,i})}{p_\mathrm{m}} = \left(\frac{R_\mathrm{p}}{R_*}\right)^2 \frac{L_\mathrm{d}}{c}, \tag{11}$$

and another scaling factor must be applied to the radius ratio. While p_m is a measured quantity, c is unknown, and if we neglect it in the physical interpretation, i.e., the right-hand side of Eq. (11), the ratio of planetary to stellar radius will be overestimated by a factor of $1/\sqrt{c}$.

The value of c cannot be quantified in the context of this work; only an estimate can be provided. Doppler imaging studies have found that polar spots are common and persistent structures in young, active stars (e.g., Huber et al. 2009). Assuming that polar spots also exist on Corot-2a and that they reach to a latitude of 70°, they occupy roughly 2% of the visible stellar disk. Adopting a spot contrast of 50%, c becomes 0.99 in this case, and the planet size would be overestimated by 0.5%. Since the poles of CoRoT-2a are seen under a large viewing angle, their impact would, thus, be appreciably smaller than the amplitude of the global brightness modulation (ca. 4%). Nonetheless, in terms of sign, this effect counteracts the transit depth decrease caused by activity, and if the polar spots are larger or symmetric structures at lower latitudes contribute, it may even balance it.

5. Discussion and conclusion

Stellar activity is clearly seen in the CoRoT measured transit light curves of CoRoT-2a, and an appropriate normalization is necessary to derive the true transit light curve profile accurately.

The transit profiles observed in CoRoT-2a are affected by activity, as is obvious in many transits where active regions cause distinct “bumps” in the light curve (e.g., Wolter et al. 2009). Furthermore, our analysis indicates that not only profiles with bumps but presumably all transit profiles are influenced by stellar activity. This is evident in the relationship between the transit equivalent width and the level of the global light curve: transits observed during periods where the star appears relatively bright are deeper than those observed during faint phases. We demonstrated that this correlation is extremely significant, but also that the data points show a large scatter around an assumed linear model relation. If the star were to modulate its surface brightness globally and homogeneously, this relation would be perfectly linear except for measurement errors. Therefore, we interpret the observed scatter as a consequence of surface evolution. When the global light curve is minimal, we also find more spots on the eclipsed portion of the surface, but only on average, and for an individual transit, this may not be the case. Thus, the surface configuration is clearly not the same for every minimum observed.

In addition, we demonstrated that the transit profiles exhibit a color dependence compatible with a color-dependent limb darkening law as expected from stellar atmospheric models and the analogy with the solar case.

All these influences can potentially interfere with the determination of the planetary parameters. Using our lower (white light) transit envelope, we determined new values for the planet-to-star radius ratio and the orbital inclination. While the latter remains compatible with previously reported results, the planet radius turns out to be larger (compared to the star) by about 3%. Although our approach takes into account many activity-related effects, a number of uncertainties remain. For example, the photospheric light curve level needed for transit normalization cannot be determined with certainty from our analysis and the same applies to the limb darkening law. We are therefore more certain than for the planetary parameters themselves, in our conclusion that the errors in their determination are much larger than the statistical ones.

While CoRoT-2a is certainly an extreme example of an active star, stellar activity is a common phenomenon especially on young stars. Therefore, in general, stellar activity cannot be neglected in planetary research, if the accuracy of the results should exceed the percent level.

Acknowledgements. S.C. and U.W. acknowledge DLR support (50OR0105). K.H. is a member of the DFG Graduiertenkolleg 1351 *Extrasolar Planets and their Host Stars*. S.S. acknowledges DLR support (50OR0703).

References

Alonso, R., Auvergne, M., Baglin, A., et al. 2008, A&A, 482, L21
Auvergne, M., Bodin, P., Boisnard, L., et al. 2009, ArXiv e-prints
Bouchy, F., Queloz, D., Deleuil, M., et al. 2008, A&A, 482, L25
Claret, A. 2004, A&A, 428, 1001
Huber, K. F., Wolter, U., Czesla, S., et al. 2009, A&A, accepted
Lanza, A. F., Pagano, I., Leto, G., et al. 2009, A&A, 493, 193
Pál, A. 2008, MNRAS, 390, 281
Pierce, A. K., & Slaughter, C. D. 1977, Sol. Phys., 51, 25
Pont, F., Gilliland, R. L., Moutou, C., et al. 2007, A&A, 476, 1347
Press, W. H., Teukolsky, S. A., Vetterling, W. T., et al. 1992, Numerical recipes in C. The art of scientific computing, ed. W. H. Press, S. A. Teukolsky, W. T. Vetterling, & B. P. Flannery
Winn, J. N. 2009, in IAU Symposium, 253, IAU Symp., 99
Wolter, U., Schmitt, J. H. M. M., Huber, K. F., et al. 2009, A&A, accepted

6.2 A planetary eclipse map of CoRoT-2a. Comprehensive lightcurve modeling combining rotational-modulation and transits.

Authors:

K. F. Huber

S. Czesla

U. Wolter

J. H. M. M. Schmitt

Published:

Astronomy & Astrophysics, 508, 901-907 (2009)

Reproduced with permission ©ESO

A&A 508, 901–907 (2009)
DOI: 10.1051/0004-6361/200912867
© ESO 2009

Astronomy & Astrophysics

A planetary eclipse map of CoRoT-2a

Comprehensive lightcurve modeling combining rotational-modulation and transits

K. F. Huber, S. Czesla, U. Wolter, and J. H. M. M. Schmitt

Hamburger Sternwarte, Universität Hamburg, Gojenbergsweg 112, 21029 Hamburg, Germany
e-mail: `khuber@hs.uni-hamburg.de`

Received 10 July 2009 / Accepted 12 September 2009

ABSTRACT

We analyze the surface structure of the planet host star CoRoT-2a using a consistent model for both the "global" (i.e., rotationally modulated) lightcurve and the transit lightcurves, using data provided by the CoRoT mission. After selecting a time interval covering two stellar rotations and six transits of the planetary companion CoRoT-2b, we have adopted a "strip" model of the surface to reproduce the photometric modulation inside and outside the transits simultaneously. Our reconstructions show that it is possible to achieve appropriate fits for the entire subinterval using a low-resolution surface model with 36 strips. The surface reconstructions indicate that the brightness on the eclipsed section of the stellar surface is (6 ± 1)% lower than the average brightness of the remaining surface. This result suggests a concentration of stellar activity in a band around the stellar equator similar to the behavior observed on the Sun.

Key words. techniques: photometric – stars: activity – planetary systems – starspots – stars: individual: CoRoT-2a

1. Introduction

Astronomers have long been interested in the surface structure of active stars and their evolution; yet, the surfaces of stars other than the Sun can hardly be resolved directly, so that indirect techniques must be used to obtain an image of the surface. One such technique is Doppler imaging (Vogt & Penrod 1983), which requires a dense series of high-resolution spectra and stellar rotation velocities of $v \sin(i) \gtrsim 20~\mathrm{km\,s^{-1}}$ (compared to $v_{\mathrm{eq}} \approx 2~\mathrm{km\,s^{-1}}$ for the Sun). Alternatively, lightcurves also yield information on stellar surface structures and can usually be obtained at low observational cost. However, photometry provides less information and the problem of lightcurve inversion is known to be notoriously ill-posed.

Since the launch of CoRoT in 2006, an increasing amount of high-quality space-based photometry has become available. Without the limitations the atmosphere and the day-night cycle impose on ground-based observatories, CoRoT is able to provide photometry with unprecedented temporal coverage and cadence, which is enormously interesting in the context of stellar activity and surface reconstruction.

In the course of the CoRoT planet-hunting project, the giant planet CoRoT-2b (Alonso et al. 2008) was detected. The host star of this planet, CoRoT-2a, is solar-like in mass and radius, but rotates approximately four times faster than the Sun and is considerably more active. The planet orbits its host star approximately three times per stellar rotation and, during its passage across the stellar disk, acts as a shutter scanning the surface of the star along a well-defined latitudinal band. Because the "local" surface structure is imprinted on the transit profiles (Wolter et al. 2009; Czesla et al. 2009), they can be used to partially resolve the ambiguity of the lightcurve inversion problem.

While Lanza et al. (2009) used the "global" lightcurve of the host star to reconstruct its surface inhomogeneities, without considering the transits, Wolter et al. (2009) concentrated on a single transit lightcurve to reconstruct a fraction of the surface, neglecting the "global" lightcurve. In this work, we combine and refine these approaches to present a reconstruction that simultaneously describes both the overall lightcurve and the transits during two stellar rotations.

2. Observations and data reduction

Alonso et al. (2008) discovered the planet CoRoT-2b using photometric data provided by the CoRoT mission (for a detailed description, see Auvergne et al. 2009). The planet was detected in the field observed during the first *long run* carried out between May 16 and Oct. 15, 2007. The default sampling rate of CoRoT photometry is $1/512~\mathrm{s^{-1}}$. The CoRoT-2 lightcurve was observed at this rate only for the first five days, after which the transits were detected and the satellite switched to alarm mode, continuing to take data every 32 s. The light collected by the CoRoT telescope is dispersed using a prism and recorded by a CCD chip. Individual sources are separated by a photometric mask, which also defines three broadband channels (nominally red, green, and blue). Currently, there is no appropriate calibration available for these channels, so that it is unfeasible to use the color information in this work. The signal obtained by summing up the individual channels, often referred to as "white light", corresponds to an optical measurement with a filter transmission maximum in the red wavelength region (Auvergne et al. 2009). Accordingly, Lanza et al. (2009) assume an isophotal wavelength of 700 nm for their passband. The CoRoT data undergo a standard pipeline processing, during which data points are flagged that are significantly affected by known events, as for example the South Atlantic Anomaly (SAA), so that they can be removed from the lightcurve.

Article published by EDP Sciences

Table 1. Stellar/planetary parameters of CoRoT-2a/b.

Star[a]	Value ± Error	Ref.[b]
P_s	(4.522 ± 0.024) d	L09
P_s^*	4.57 d	
Spectral type	G7V	B08
Planet[c]	Value ± Error	Ref.
P_p	$(1.7429964 \pm 0.0000017)$ d	A08
T_c [BJD]	$(2\,454\,237.53362 \pm 0.00014)$ d	A08
i	$(87.7 \pm 0.2)°$	C09
$R_\mathrm{p}/R_\mathrm{s}$	(0.172 ± 0.001)	C09
a/R_s	(6.70 ± 0.03)	A08
u_a, u_b	(0.41 ± 0.03), (0.06 ± 0.03)	A08

[a] P_s – stellar rotation period, P_s^* – stellar rotation period used for the observation interval analyzed in this paper (see Sect. 3.4). [b] Taken from Lanza et al. (2009) [L09], Alonso et al. (2008) [A08], Bouchy et al. (2008) [B08], or Czesla et al. (2009) [C09]. [c] P_p – orbital period, T_c – central time of first transit, i – orbital inclination, $R_\mathrm{p}, R_\mathrm{s}$ – planetary and stellar radii, a – semi major axis of planetary orbit, u_a, u_b – linear and quadratic limb darkening coefficients.

The host star CoRoT-2 has a spectral type of G7V with an optical companion at a distance of approximately 4.3″ (2MASS, Skrutskie et al. 2006), too close to be resolved by CoRoT. According to Alonso et al. (2008) the secondary contributes a constant fraction of $(5.6 \pm 0.3)\%$ to the total CoRoT-measured flux. In Table 1 we list the system parameters of CoRoT-2a/b, which are used throughout our analysis. CoRoT-2b's orbital period of ≈1.74 days is about a third of CoRoT-2a's rotation period; hence, the almost continuous CoRoT data sample of 142 days covers about 30 stellar rotations and more than 80 transits. The lightcurve shows signatures of strong stellar activity and substantial rotational modulation (Lanza et al. 2009). We use the same CoRoT raw data reduction procedures as described in Czesla et al. (2009, Sect. 2).

3. Analysis

3.1. Modeling approach

The measurements of the Rossiter-McLaughlin effect by Bouchy et al. (2008) suggest that the rotation axis of the host star and the planet's orbit normal are approximately co-aligned ($\lambda = 7.4 \pm 4.5°$). The sign λ represents the misalignment angle projected on the plane of the sky, and its value strongly favors aligned orbital and rotational axes, even though it does not prove it. More support for a co-aligned geometry comes from the following argument. Comparing the measured $v \sin(i) = 11.85\ \mathrm{km\,s^{-1}}$ with a calculated equatorial velocity of $v_\mathrm{eq} = 2\pi R_\mathrm{s}/P_\mathrm{s} \approx 10\ \mathrm{km\,s^{-1}}$ derived with the theoretically obtained value $R_\mathrm{s} = 0.9 \cdot R_\odot$ (Alonso et al. 2008) also favors $\sin(i) \approx 1$.

As a result, the planet always eclipses the same low-latitude band between 6 and 26 degrees. The transits separate the stellar surface into two observationally distinct regions, i.e., a region eclipsed by CoRoT-2b and another region that is not. In the case of CoRoT-2a, the eclipsed section covers ≈21% of the stellar disk corresponding to ≈17.3% of its surface. The time-resolved planet migration across the visible stellar disk sequentially covers and uncovers surface fractions, so that the brightness profile of the underlying stellar surface is imprinted on the transit lightcurve.

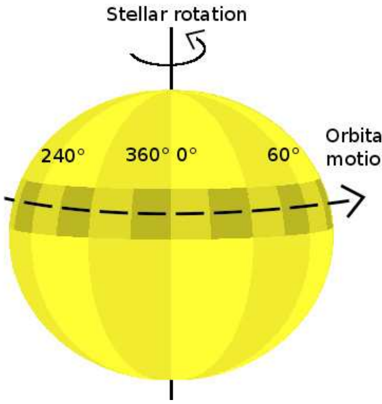

Fig. 1. Our model geometry using 12 longitudinal strips for the noneclipsed and 24 strips for the eclipsed section, respectively.

For our modeling, we separate the surface into the eclipsed and the noneclipsed section, which are both further subdivided into equally sized, longitudinal bins or "strips" as demonstrated in Fig. 1. Let N_e be the number of bins in the eclipsed section and N_n be the number of noneclipsed strips. As is apparent from Fig. 1, N_e and N_n need not be the same. Altogether, we have $N_\mathrm{tot} = N_\mathrm{e} + N_\mathrm{n}$ bins enumerated by some index j. A brightness b_j is assigned to each of these surface bins, with which it contributes to the total (surface) flux of the star. Then let V_{ji} denote the visibility of the jth bin at time t_i. The visibility is modified in response to both a change in the viewing geometry caused by the stellar rotation and a transit of the planet. The modeled flux $f_{\mathrm{mod},i}$ at time t_i is then given by the expression

$$f_{\mathrm{mod},i} = \sum_{j=1}^{N_\mathrm{tot}} V_{ji} b_j. \tag{1}$$

We determine the unknown brightnesses, b_j, by comparing $f_{\mathrm{mod},i}$ to a set of M_C CoRoT flux measurements using a specifically weighted version of the χ^2-statistics:

$$\chi_\mathrm{m}^2 = \sum_{i=1}^{M_\mathrm{C}} \frac{(f_{\mathrm{mod},i} - f_{\mathrm{obs},i})^2}{\sigma_i^2} \cdot w_i, \tag{2}$$

where χ_m^2 differs from χ^2 by a weighting factor, w_i, which we choose to be 10 for lightcurve points in transits and 1 otherwise. In this way, the global lightcurve and the transits are given about the same priority in the minimization process. Error bars for the individual photometric measurements were estimated from the datapoint distribution in the lightcurve, and the same value of $\sigma = 1000\ \mathrm{e}^-/32\ \mathrm{s}$ ($= 1.4 \times 10^{-3}$ after lightcurve normalization) was used for all points.

In our modeling we currently exclude surface structures with a limb-angle dependent contrast. This particularly refers to solar-like faculae, for which Lanza et al. (2009) find no evidence in their analysis. The planet CoRoT-2b is modeled as a dark sphere without any thermal or reflected emission. This approximation is justified by the findings of Alonso et al. (2009), who report a detection of the secondary transit with a depth of $(0.006 \pm 0.002)\%$, which is negligible in our analysis.

The actual fit is carried out using a (nongradient) Nelder-Mead simplex algorithm (e.g. Press et al. 1992). All strips are mutually independent, and as we define only a rather coarse strip subdivision for the noneclipsed section of the surface and since the eclipsed section is thoroughly covered by the transits, no further regularization is necessary.

3.2. Fit parameter space – parametrization, restrictions, and interpretation

Our fit space has a total of $N_{\mathrm{tot}} = N_{\mathrm{e}} + N_{\mathrm{n}}$ dimensions, and the associated parameters are the brightnesses, $b_{j=1\ldots N_{\mathrm{tot}}}$. The most obvious choice of fit parameters are the brightnesses themselves. Nevertheless, using a slightly different definition in our algorithm provides some advantages. Instead of using the brightness of the global strips in our fits, we replace them with a weighted sum of the brightnesses of the eclipsed and the noneclipsed strips covering the same longitudes. This quantity z is a measure of the total flux emitted from all strips enclosed within a certain longitude range and, therefore, represents the level of the global lightcurve independent of how the brightness is distributed among the individual strips contributing to the sum. Without any transit observations, the distribution of flux among the individual contributors could hardly be restricted further, because latitudinal information could not be recovered. Thus, we use the tuple $(b_{l=1\ldots N_{\mathrm{e}}}, z_{k=1\ldots N_{\mathrm{n}}})$ for our reconstructions, where z is defined by

$$z_k = b_{N_{\mathrm{e}}+k} + \frac{1}{c \cdot q} \sum_{s=q_0}^{s<q_0+q} b_{\mathrm{s}}. \tag{3}$$

In Eq. (3), $b_{N_{\mathrm{e}}+k}$ denotes the brightness of the kth global strip, q is defined by $N_{\mathrm{e}}/N_{\mathrm{n}}$ (the factor by which the eclipsed section is oversampled compared to the noneclipsed section), the index range $q_0 \leq s < q_0 + q$ enumerates all eclipsed strips covering the same longitudes as the global strip referred to by $b_{N_{\mathrm{e}}+k}$, and c is a scaling factor accounting for the size difference between the eclipsed and the noneclipsed sections.

The practical advantage of using z instead of the brightness values themselves lies in the parameter interdependence. If we assume a fit algorithm adjusts the structure of a transit lightcurve using the eclipsed strips, every modification of their brightness causes a modification of the global lightcurve level, which might possibly be compensated by an appropriate adjustment of the global strip's brightness. Such an adjustment is inherent in the definition of z, so that $b_{l=1\ldots N_{\mathrm{e}}}$ and $z_{k=1\ldots N_{\mathrm{n}}}$ become largely independent quantities. In our fits we use $c = 5$, which roughly corresponds to the ratio of disk area covered by global and eclipsed strips.

To normalize the observed CoRoT-2a lightcurve, we divided all measurements by the highest flux value in our lightcurve so that $0 < (\mathrm{normalizedflux}) \leq 1$. The matrix V_{ji} in Eq. (1) is normalized according to

$$\sum_{j=1}^{N_{\mathrm{tot}}} V_{ji} = 1 \text{ for all } i,$$

which yields $f_{\mathrm{mod},i} = 1$ for $b_j = 1$, i.e., a constant model lightcurve at level 1. In a first, tentative interpretation, a surface element with the brightness 1 corresponds to a photospheric element free of any spots. Nonetheless, this is only correct as long as we assume that the largest observed flux in the lightcurve indeed represents the "spot-cleaned" photospheric luminosity. As CoRoT-2a is, however, a very active star, it seems probable that polar spots persist on its surface. Moreover, it seems likely that lower latitude structures cover a fraction of the stellar surface even if the lightcurve is at maximum. For this reason, individual surface elements (strips) may be brighter than the "average surface" during the maximum observed flux. While such information could not be recovered if no transits were observed, individual surface regions eclipsed by the planet can conceivably be brighter than the "global" photosphere seen during lightcurve maximum. Therefore, we do not exclude strips with brightness values above 1 in our fits; i.e., we do not fix the photospheric brightness. This results in brightnesses above 1 for individual strips (e.g. Fig. 5). The only parameter space restriction applied during our fits is that the brightness must be positive.

3.3. Which part of the lightcurve should be used?

To derive a meaningful model, we need to select a time span, which is both long enough to provide an appropriate coverage of the surface, and short enough to minimize the effects of surface evolution. The latter, while doubtlessly present, appears slow compared to the stellar rotation period. Lanza et al. (2009) give typical lifetimes of 55 d (≈12 rotations) for active regions and 20−30 d for some individual spots. In our analysis, we use the time span ranging from phase 1.85 through 3.85 (BJD = 2 454 245.988 to BJD = 2 454 255.128, BJD = Barycentric Julian Date), which covers 6 transits and shows only small variations in the global lightcurve. The data are re-binned using a binsize of 128 s for the transit covered periods and 2016 s for the remaining lightcurve.

Our binning approach has to take into account interruptions of the lightcurve due to data drop outs (for instance caused by the South Atlantic Anomaly) and, of course, has to account for the change in bin size when a transit period begins or ends. Moreover, the CoRoT-2 lightcurve is sampled at two different rates ($1/512\ \mathrm{s}^{-1}$ and $1/32\ \mathrm{s}^{-1}$), which does not, however, cause any problem during the time span under consideration here. To obtain the binned curve, we averaged all flux values comprised of a bin and place the resulting value at the barycenter of the contributing time stamps. To compute the error, we divided the standard deviation for individual points by the square root of the number of averaged points. With this approach we (typically) obtain an error of 7×10^{-4} for in-transit points and 1.8×10^{-4} for out-of-transit points.

In Fig. 2 we demonstrate the coverage of the eclipsed surface section by these 6 transits within the selected phase interval. A single rotation phase including three transits only provides a very inhomogeneous "scan" of the eclipsed surface because of limb darkening, projection geometry, and the distribution of transit intervals (cf. Fig. 2). As a transit occurs every ≈0.4 stellar rotations, a homogeneous coverage of one full rotation is achieved using five transits. Nonetheless, we decided to use an integer number of stellar rotations and used six transits with the last one showing virtually the same part of the eclipsed surface as the first.

3.4. Surface evolution, rotation period, and model limits

Although the lightcurve of CoRoT-2a shows remarkably periodic minima and maxima, the rotation period of the star is not known exactly. Using a Lomb-Scargle periodogram, Lanza et al. (2009) find a rotation period of (4.52 ± 0.14) d for the star, which is further refined in the course of their surface modeling. Assuming that the longitudinal migration of the active longitudes should be minimal, Lanza et al. pin down the stellar rotation period to 4.5221 d. While this rotation period minimizes the

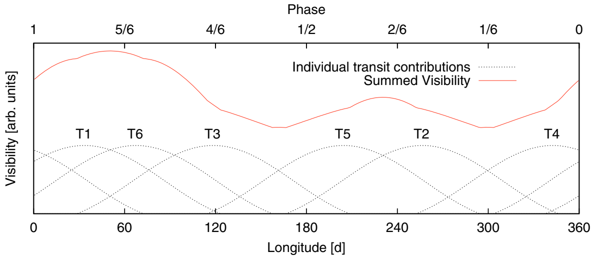

Fig. 2. Visibility of the eclipsed stellar surface during the transits in the selected observation interval. Low visibility means that a stellar feature at the corresponding longitude has a low impact on the transit profiles.

migration of the active longitudes, it results in individual spots showing a retrograde migration with an apparent angular velocity ≈1.3% lower than the stellar rotation.

For our modeling we determine an "effective" period, representing the rotation period of the dominating surface features we are mainly interested in. We use the selected part of the lightcurve, remove the transits, and fold the remaining lightcurve back at a number of periods between 4.4 d and 4.7 d. The best match is obtained using a period of 4.57 d, which also results in the best fits of our models, so we use it throughout our analysis. This period also agrees with the values given by Lanza et al. (2009) assuming a rotation period of 4.5221 d and a mean retrograde migration "slowing down" the spots by 1.06%; however, changes in the rotation period on this scale do not result in significantly different surface reconstructions.

Even though we identified a lightcurve interval with relatively weak surface evolution, and refined the rotation period to account for some evolutionary effects, there is still a remaining modulation. This modulation imposes a fundamental limit on the fit quality that can be achieved by adopting a static model to the lightcurve, because both stellar rotations have to be described by the same model. To estimate this limit, again for the global lightcurve alone, we estimated the quantity

$$\langle\Delta\chi^2\rangle = \frac{1}{N}\sum_{i=1}^{N}\left(\frac{f(p_i) - f(p_i + 1.0)}{2\sigma}\right)^2 \approx 14.2. \qquad (4)$$

Here, $f(p_i)$ is the normalized flux in the ith phase bin, $f(p_i + 1.0)$ is the flux measured at the same phase during the next stellar rotation, and the sum stretches over all phases pertaining to the first rotation. The flux $f(p_i + 1.0)$ was obtained by interpolation, because the phase sampling is not exactly the same in both rotations. Since $\sigma_i \approx \sigma$, the best conceivable common model with respect to χ^2 at phase point p_i is given by $(f(p_i) + f(p_i + 1.0))/2$, so that the sum in Eq. (4) estimates the χ^2 contributions induced by surface evolution for each point. If there was no surface evolution, the expression in Eq. (4) would equate to 0.5, because statistical errors are, of course, still present. Therefore, a limit of $\chi^2 \approx 14.2$ per (global) lightcurve point will not be overcome by any static model. Equivalently, the expectation value, $\langle\Delta f/2\rangle$, for the flux deviation from the best model equals $\langle\Delta f/2\rangle = \langle(f(p_i) - f(p_i + 1.0))/2\rangle = 5.6 \times 10^{-4}$ and cannot be surpassed.

3.5. Model resolution

The parameters N_e and N_n specify the model resolution of the eclipsed and noneclipsed sections. An appropriate choice of these parameters balances fit quality and model ambiguity; this way the largest possible amount of information can be extracted.

To find the optimal value for the number of noneclipsed strips, we carry out fits to only the global lightcurve using an increasing number of global strips. Starting with only 4 strips, we find the reduced χ^2 value, χ^2_R, to decrease rapidly until 8 strips are used. From this point, χ^2_R only responds weakly to an increase in the strip number, but still decreases. Using 12 strips, we find $\chi^2_\mathrm{R} = 16$. With an estimated "socket" contribution of ≈14.4 provided by surface evolution, we attribute a fraction of $\chi^2_\mathrm{R} \approx 1.6$ to statistical noise. This fraction decreases to ≈1 if we use 30 strips, in which case we obtain a longitudinal resolution of 12°, comparable to what is achieved by Lanza et al. (2009). According to our test runs, we obtain reasonably stable results using 12 strips. As the stability of the solutions decreases for larger strip numbers, while χ^2_R only slightly improves, we argue in favor of using 12 global strips in our modeling, to extract the largest possible amount of physically relevant results.

The resolution used on the eclipsed surface band is determined according to the following considerations. The extent of the planetary disk at the center of the stellar disk is about 20° × 20°. All stellar surface elements simultaneously (un)covered by the planet's disk are equivalent in our lightcurve modeling. Individual features can, thus, be located (or smeared out) along the edge of the planetary disk to provide the same effect in the lightcurve. This edge stretches across 10° in longitude (only the "forward" part) and 20° in latitude, which defines a fundamental limit for the resolution. Assuming a particular shape for the features, decreases the degree of ambiguity as was for example shown by Wolter et al. (2009).

A meaningful structure in the transit profile should comprise at least 3 consecutive lightcurve bins corresponding to about 360 s or ≈6° of planet movement across the center of the stellar disk. The extent of individual strips should, therefore, not fall below this limit, but be even larger.

Combining these arguments with the results of our test runs, we decided to use 24 strips on the eclipsed section, so that a longitudinal resolution of 15° is achieved. With this choice, a single strip on the eclipsed band appears about the same size (face-on) as the planetary disk. Additionally, we note that this approximately corresponds to the resolution used by Lanza et al. (2009) in their maximum entropy reconstructions.

3.6. Results of the modeling

In our analysis, we achieve a longitudinal resolution of ≈15° on the eclipsed section making up ≈17% of the stellar surface and 30° for the rest.

In Figs. 3 and 4 we present the results of our modeling. Figure 3 shows the entire subsample of CoRoT data points used in our modeling, along with our lightcurve model in the upper panel. In the lower panel we show the model residuals (see Sect. 3 for the definition of the error). Obviously, the data are matched well; however, there are systematic offsets between the observation and the model. In particular, the model tends to overestimate the observations during the first half of the time span, whereas it underpredicts it in the second half. This effect is related to surface evolution already detectable on timescales below the rotation period (Lanza et al. 2009, also see Sect. 3.4). Within the transits the residuals remain small compared to the rest of the lightcurve. This must be regarded a consequence of both the smaller bin size of 128 s used here and the twice better resolution of the model on the eclipsed section. During the fit the

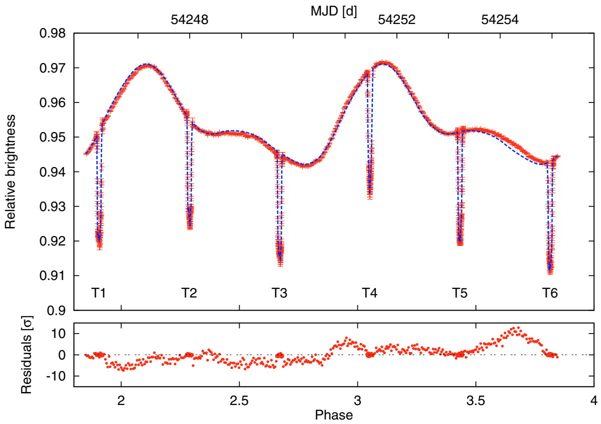

Fig. 3. *Upper panel*: CoRoT data for rotational phases 1.85 to 3.85 (2016 s binning for the global lightcurve and 128 s for the transits, red symbols) and our model lightcurve (dashed blue curve). *Lower panel*: residuals of our model.

transit residuals are "overweighted" by a factor of ten to avoid them to be prevailed by the much larger global residuals. Although, the deviations can be as large as 10σ, the mean deviation of the global lightcurve from the model amounts to 620×10^{-6} not far from the theoretical limit of 560×10^{-6} (cf. Sect. 3.4).

The lightcurve presented in Fig. 3 contains six transits (labeled "T1 – 6"). The associated transit lightcurves are shown in detail with our models in Fig. 4. Each individual panel shows the same transit twice: the lower curve represents a transit reconstruction from the full data sample (phases 1.85–3.85), and the upper curve denotes a reconstruction from only the first ($T1$–3) or second ($T4$–6) half of the sample data (shifted up by 0.03). The dotted lines show the transits as we would observe them without any activity on the eclipsed section of the surface, where we assume a brightness of 1 for the underlying photosphere.

The transit reconstructions obtained from half of the sample data reproduce the transit substructure very accurately. The resulting surface reconstructions are, however, unreliable where the surface is insufficiently covered (cf. Fig. 2, around longitudes of 180° and 320°). Interestingly, those reconstructions based on data from two rotation phases also recover most of the transit substructure and are by no means off the mark. When both rotation periods are used, χ^2 typically increases by 10–20%, a difference hardly visible in Fig. 4. As an exception, the fit quality of the third transit (T3) decreases dramatically, with χ^2 increasing by a factor of ≈2.5. This is, however, mainly a consequence of the observed surface evolution shifting the continuum level. The overall stability of the fit quality indicates that lifetimes of surface features are a few stellar rotations, which agrees with the results of Lanza et al. (2009).

In Fig. 5 (lower and middle panels) we present the strip brightness distribution pertaining to the lightcurve model shown in Figs. 3 and 4, i.e., a 1D-reconstruction of the surface. We estimated mean and errors by recording the distribution of the parameter values obtained from 50 reconstructions with randomized starting points, and the respective distributions are indicated by the color gradients in Fig. 5. The error bars correspond to the associated standard deviations. They reflect the ability of the fitting algorithm to converge to a unique extremum, which is determined by both the characteristics of the algorithm and the structure of the fit statistics. Investigating the brightness distribution of the noneclipsed strips, we notice a slight degeneracy in some of the 12 noneclipsed strips; i.e., a fraction of the brightness may be redistributed without considerable loss of fit quality. The averaging of the 50 reconstructions flattens out such features, thus acting like a regularization of the brightness distribution. No such effect is observed for the eclipsed strips.

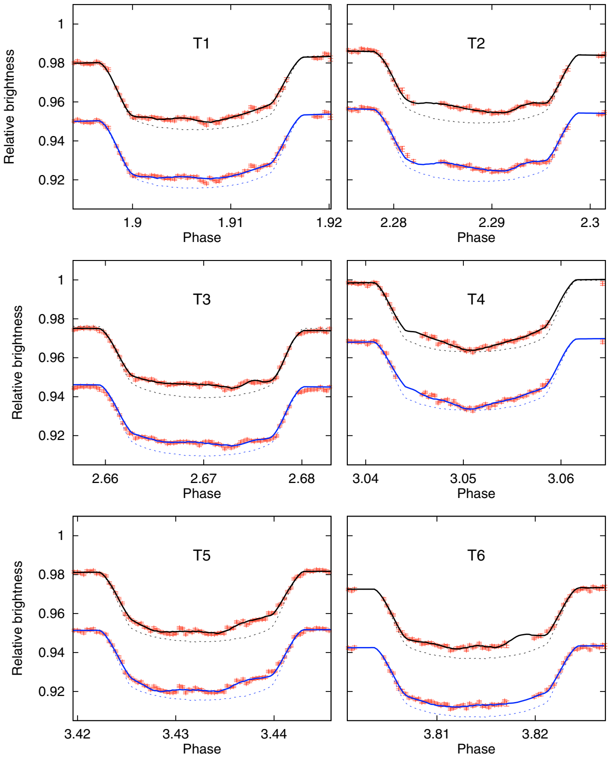

Fig. 4. Close-up of the six individual transits (128 s binning). Observations are drawn as red points (including 1σ errors). The upper curve (black) in each panel shows the fit obtained from 1 rotation (phases 1.85 to 2.85 for $T1$–3 and 2.85 to 3.85 for $T4$–6); the lower curve (blue) gives the fit obtained by modeling both rotations (as seen in Fig. 3). The dashed lines show the undisturbed transit profile for comparison.

We compared our results to the reconstructions given by Lanza et al. (2009, their Fig. 4) and find our longitude scale to be shifted by ≈70° with respect to the Lanza et al. scale. Our reconstructions show the same bright band at a longitude of ≈260° (330° in our work). Tentatively averaging over an appropriate "time band" in their Fig. 4, we also find qualitative agreement for the remaining spot distribution.

Clearly, the flux fraction contributed by the eclipsed strips is less than that of the noneclipsed strips, because the area they cover is smaller by a factor of five. In the upper panel of Fig. 5 we show the lightcurve model contributions provided by the eclipsed and the noneclipsed section with their sum making up the model for the CoRoT data, which is also shown. The median flux level was subtracted from all curves to emphasize the modulation amplitude in favor of flux level. Obviously, the modulation amplitudes induced by the eclipsed and noneclipsed section balance approximately. This indicates that their influence on the stellar variability is about the same despite their large difference in size.

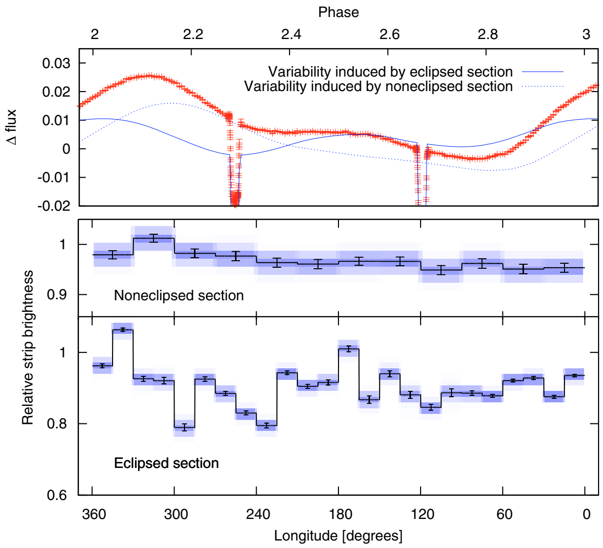

Fig. 5. *Upper panel*: the CoRoT data (red symbols) and the flux modulation contributed in our model by the eclipsed (blue curve) and noneclipsed section (dotted gray curve) individually. All curves are median-subtracted. *Middle and lower panels*: Brightness distribution of the strips located on the eclipsed and noneclipsed sections of the surface. The color gradient renders the distribution obtained from 50 reconstructions with randomized starting points.

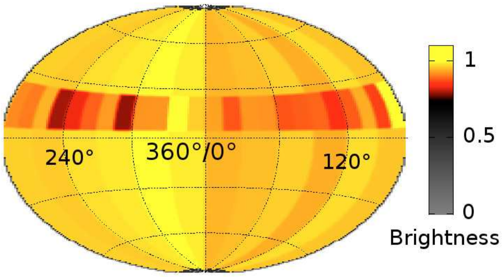

Fig. 6. Surface map of CoRoT-2a showing the reconstructed brightness distribution. Spots located on the noneclipsed surface are blurred over the entire reconstruction strip because of their unknown latitude resulting in the lower contrast compared to the eclipsed section.

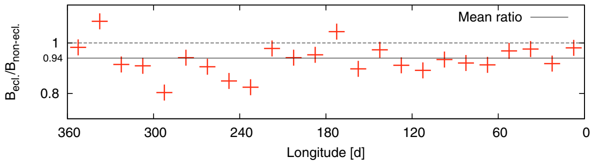

Fig. 7. Ratio of the surface brightness in the eclipsed ($B_{\mathrm{ecl.}}$) and noneclipsed ($B_{\mathrm{non-ecl.}}$) sections.

A visualization of our best-fit surface reconstruction is presented in Fig. 6, showing a Hammer projection of the associated distribution of surface brightnesses. The planet-defined low-latitude band shows especially dark features, e.g. in the range of 200° to 300° in longitude, and is clearly visible. Also the noneclipsed sections of the star show significant variations. Note that our map only shows the average brightness of these regions; since the noneclipsed regions are larger by area, they contribute more flux; however, the “missing” flux in these regions is likely to also be concentrated in spots. In the following section we address the issue of the flux contribution from the eclipsed and noneclipsed sections.

3.6.1. Brightness distribution and spot coverage

Without a very precise absolute flux calibration (as e.g. in Jeffers et al. 2006), lightcurve analyses can usually only investigate the inhomogeneous part of the entire spot coverage. This statement is, however, partially invalidated by a transiting planet because it breaks the symmetry of the problem. Spots eclipsed by the planetary disk distort the transit profiles regardless of whether they belong to a structure that appears symmetric on a global scale or not.

As an example, assume that half the eclipsed section of CoRoT-2a, say longitudes 0–180°, is spotted, while the other half is covered by an undisturbed photosphere. Clearly, the transits will be shallower when the planet eclipses the dark portion of the star, and they will be deeper when the bright section is eclipsed. Also, the lightcurve will be distorted. Assume as well that a comparable section between longitudes 180–360° is dark on the opposite hemisphere of the star outside the eclipsed band. In this case the global spot configuration is perfectly symmetric with respect to longitude and the global lightcurve does not show any trace of activity. Nevertheless, the transits will still be shallower when the planet eclipses the dark band, and they will still be deeper when the bright surface is eclipsed.

If the spots were distributed symmetrically across the stellar surface, we would expect the stellar surface to be homogeneously bright. In Fig. 7 we show the brightness ratio of eclipsed and noneclipsed sections as a function of longitude. Since there are more eclipsed than noneclipsed strips, we always compare strips covering the same longitude. Only in two cases is the eclipsed section brighter than its noneclipsed counterpart, while in 22 cases it is not.

The mean ratio is 0.94 ± 0.01 so that the part of the star passingly covered by the planet is found to be 6% darker than the rest of the surface. The remaining (nontransited) surface is brighter *on average*, but locally it may even be darker.

4. Discussion and conclusions

We present a surface reconstruction for the planet host star CoRoT-2a. Our modeling is based on a CoRoT data interval covering two full stellar rotations, and it treats the entire lightcurve – including the planetary transits – in a consistent way.

We show that a consistent modeling of the lightcurve is possible using a static model, i.e., not including any spot evolution. Although surface evolution on scales of the stellar rotation period is seen in both the reconstruction of the global lightcurve (as already reported by Lanza et al. 2009) and the transit lightcurves, this effect is weak in the context of our analysis. The static model provides reasonable fits to six consecutive transit lightcurves. The associated surface configuration changes little during this period, so the surface evolution must be relatively slow compared to the timescale of ≈9 d under consideration. This timescale is also valid for the lifetimes of spots on the eclipsed surface section.

Our results indicate that the planet-eclipsed band on the stellar surface is – on average – about 6% darker than the remaining part of the surface. Lanza et al. (2009) note that the strength of differential rotation derived from their lightcurve fits seems much lower than the expected values derived from measurements in other systems (Barnes et al. 2005). They speculate that this may indicate a spot distribution limited to a narrow latitude band. If this is true, the latitude band is possibly located at low latitudes, i.e., within ±30° around the equator as observed on the Sun. In this case it covers the eclipsed section where we find a darker surface, i.e., higher spot coverage. We caution that this result may also be influenced by the adopted planetary parameters (mainly the size), which are hard to determine accurately (Czesla et al. 2009).

We checked whether the effect of gravitational darkening could significantly contribute to a darker surface in the vicinity of the equator. For the stellar parameters of CoRoT-2a, we find that the (effective) gravitational accelerations at the poles and at the equator are equal to within 0.07%, so that gravitational darkening does not significantly contribute to the brightness gradient found in our modeling. This result is nearly independent of the assumed coefficient, β_1 ($T_{\rm eff}^4 \propto g^{\beta_1}$ with the effective surface temperature $T_{\rm eff}$ and the surface gravity g), which is approximately 0.3−0.4 for CoRoT-2a (Claret 2000).

The "narrow-band hypothesis", i.e., a higher spot coverage in the planet-eclipsed section compared to the noneclipsed surface, also provides a natural explanation for the fact that both the eclipsed and noneclipsed surface regions account for about the same amplitude of variation in the lightcurve. Using the Sun as an analogy again, we would qualitatively expect the same structure, as seen under the planet path, on the opposite hemisphere as well: two "active belts" that are symmetric with respect to the equator. The noneclipsed activity belt, which would be only observable in the global lightcurve, would then be primarily responsible for the variability of the lightcurve contributed by the noneclipsed surface section.

We conclude that our results support a surface model consisting of active regions north and south of the equator, possibly even bands of spots at low latitudes analogous to the Sun. Further investigations of this system using more sophisticated models (first of all surface evolution) and using the entire observation interval of approximately 140 days have the potential of revealing more information on the constantly changing surface distribution of spots on CoRoT-2a.

Acknowledgements. K.H. is a member of the DFG Graduiertenkolleg 1351 *Extrasolar Planets and their Host Stars*. S.C. and U.W. acknowledge DLR support (50OR0105).

References

Alonso, R., Auvergne, M., Baglin, A., et al. 2008, A&A, 482, L21
Alonso, R., Guillot, T., Mazeh, T., et al. 2009, A&A, 501, L23
Auvergne, M., Bodin, P., Boisnard, L., et al. 2009, A&A, 506, 411
Barnes, J. R., Cameron, A. C., Donati, J.-F., et al. 2005, MNRAS, 357, L1
Bouchy, F., Queloz, D., Deleuil, M., et al. 2008, A&A, 482, L25
Claret, A. 2000, A&A, 359, 289
Czesla, S., Huber, K. F., Wolter, U., Schröter, S., & Schmitt, J. H. M. M. 2009, A&A, accepted
Jeffers, S. V., Barnes, J. R., Cameron, A. C., & Donati, J.-F. 2006, MNRAS, 366, 667
Lanza, A. F., Pagano, I., Leto, G., et al. 2009, A&A, 493, 193
Press, W. H., Teukolsky, S. A., Vetterling, W. T., & Flannery, B. P. 1992, Numerical recipes in C. The art of scientific computing, ed. W. H. Press, S. A. Teukolsky, W. T. Vetterling, & B. P. Flannery (Cambridge University Press)
Skrutskie, M. F., Cutri, R. M., Stiening, R., et al. 2006, AJ, 131, 1163
Vogt, S. S., & Penrod, G. D. 1983, PASP, 95, 565
Wolter, U., Schmitt, J. H. M. M., Huber, K. F., et al. 2009, A&A, 504, 561

6.3 Planetary eclipse mapping of CoRoT-2a. Evolution, differential rotation, and spot migration.

Authors:

K. F. Huber
S. Czesla
U. Wolter
J. H. M. M. Schmitt

Published:

Astronomy & Astrophysics, accepted

Reproduced with permission ©ESO

A&A 514, A39 (2010)
DOI: 10.1051/0004-6361/200913914
© ESO 2010

Astronomy & Astrophysics

Planetary eclipse mapping of CoRoT-2a

Evolution, differential rotation, and spot migration

K. F. Huber, S. Czesla, U. Wolter, and J. H. M. M. Schmitt

Hamburger Sternwarte, Universität Hamburg, Gojenbergsweg 112, 21029 Hamburg, Germany

Received 18 December 2009 / Accepted 17 February 2010

ABSTRACT

The lightcurve of CoRoT-2 shows substantial rotational modulation and deformations of the planet's transit profiles caused by starspots. We consistently model the entire lightcurve, including both rotational modulation and transits, stretching over approximately 30 stellar rotations and 79 transits. The spot distribution and its evolution on the noneclipsed and eclipsed surface sections are presented and analyzed, making use of the high resolution achievable under the transit path.

We measure the average surface brightness on the eclipsed section to be (5 ± 1)% lower than on the noneclipsed section. Adopting a solar spot contrast, the spot coverage on the entire surface reaches up to 19% and a maximum of almost 40% on the eclipsed section. Features under the transit path, i.e. close to the equator, rotate with a period close to 4.55 days. Significantly higher rotation periods are found for features on the noneclipsed section indicating a differential rotation of $\Delta\Omega > 0.1$. Spotted and unspotted regions in both surface sections concentrate on preferred longitudes separated by roughly 180°.

Key words. planetary systems – techniques: photometric – stars: activity – starspots – stars: individual: CoRoT-2a

1. Introduction

The space-based CoRoT mission (e.g. Auvergne et al. 2009), launched in late 2006, provides stellar photometry of unprecedented quality. One of CoRoT's primary tasks is the search for extra-solar planets using the transit method. So far several systems with eclipsing exoplanets were found, one of them CoRoT-2 harboring a giant close-in "hot-jupiter".

The planet CoRoT-2b was discovered by Alonso et al. (2008), who determined the system parameters from transits and follow-up radial velocity (RV) measurements. Bouchy et al. (2008) observed the Rossiter-McLaughlin effect using additional RV measurements and determined the projected angle $\lambda = (7.2 \pm 4.5)^\circ$ between the stellar spin and the planetary orbital axis. Lanza et al. (2009) used the strong rotational modulation of the lightcurve to study the spot distribution and its evolution; they detect a stellar rotation period of $P_{\rm rot} = (4.522 \pm 0.024)$ d and two active longitudes on opposite hemispheres. The secondary eclipse of the planet was first detected by Alonso et al. (2009) in white light. Later the analysis was refined and extended by Snellen et al. (2010), detecting significant thermal emission of the planet; Gillon et al. (2009) repeated this work using additional infrared data. They also find an offset of the secondary transit timing indicating a noncircular orbit.

The determination of the planetary parameters by Alonso et al. (2008) did not account for effects of stellar activity, which is in general not negligible for active stars. Czesla et al. (2009) re-analyze the transits and derive new parameters for the planet radius $R_{\rm p}/R_{\rm s}$ and the orbital inclination i considering the deformation of transit profiles due to spot occultation. This is especially important for attempts to reconstruct active surface regions from transit profiles. An analysis of a single transit by Wolter et al. (2009) shows the potential of eclipse-mapping and yielded constraints on the properties of the detected starspot. Similar approaches to analyze signatures of starspots in transit profiles were also carried out by Pont et al. (2007) (HD 189733) and Rabus et al. (2009) (TrES-1) primarily using data obtained with the Hubble Space Telescope. In a more comprehensive approach, Huber et al. (2009) reconstructed an interval of the CoRoT-2 lightcurve over two stellar rotations including the transits.

This work is based on the paper of Huber et al. (2009). We now analyze the *entire* data set of CoRoT-2, modeling both the rotational modulation of the global lightcurve and transits simultaneously. In this way we derive stellar surface maps for both the noneclipsed and the eclipsed section of the star.

2. Observations and data reduction

The data were obtained in the first *long run* of the CoRoT satellite (May 16 to Oct. 15, 2007). The planetary system CoRoT-2 (Star CorotID 0101206560) consists of an active solar-like G7V star and a large planetary companion on a close orbit. Due to its edge-on view and an orbit period of only about 1.7 days, this lightcurve contains about 80 transits, roughly 3 during each stellar rotation.

The large surface inhomogeneities of this very active star are clearly visible in the rotational modulation of the CoRoT lightcurve taken over approximately 140 days. Although there is surface evolution even on timescales of one stellar rotation, these changes are small compared to the modulation amplitude. Significant deformations of the transit profiles due to spots are also visible throughout the whole time series.

The stellar and planetary parameters used throughout this analysis are given in Table 1. The extensive raw data analysis and reduction follows the descriptions in Czesla et al. (2009) and Huber et al. (2009).

In this paper we only analyze the *alarm mode* data of CoRoT-2, when the satellite switched from a sampling

Table 1. Stellar/planetary parameters of CoRoT-2a/b.

Star[a]	Value ± Error	Ref.
P_s	(4.522 ± 0.024) d	L09
Spectral type	G7V	B08
Planet[b]	Value ± Error	Ref.
P_p	(1.7429964 ± 0.0000017) d	A08
T_c [BJD]	(2 454 237.53562 ± 0.00014) d	A08
i	(87.7 ± 0.2)°	C09
$R_\mathrm{p}/R_\mathrm{s}$	(0.172 ± 0.001)	C09
a/R_s	(6.70 ± 0.03)	A08
u_a, u_b	(0.41 ± 0.03), (0.06 ± 0.03)	A08

References. taken from Lanza et al. (2009) [L09], Alonso et al. (2008) [A08], Bouchy et al. (2008) [B08], or Czesla et al. (2009) [C09].

Notes. [a] P_s - stellar rotation period; [b] P_p – orbital period, T_c – central time of first transit, i – orbital inclination, $R_\mathrm{p}, R_\mathrm{s}$ – planetary and stellar radii, a – semi major axis of planetary orbit, u_a, u_b – linear and quadratic limb darkening coefficients.

rate of $1/512\ \mathrm{s}^{-1}$ to $1/32\ \mathrm{s}^{-1}$ (which started after 3 transits), and use the combination of the three color channels ("white" light). Our analysis starts after one stellar rotation at JD = $T_\mathrm{c} + P_\mathrm{s}$ = 2454242.05562 (see Table 1) or a stellar rotation phase of $\phi_\mathrm{s} = 1.0$, respectively. We use units of stellar rotation phase in our analysis, the last point of our data interval corresponds to $\phi_\mathrm{s} = 31.24$. This leaves us with an observation span of more than 30 stellar rotations containing 79 transits. In the following the first transit inside our data interval is labeled 0, the last 78.

3. Analysis

3.1. The model

The projected axes of the planetary orbit and the stellar rotation are co-aligned (Bouchy et al. 2008), which strongly suggests a 3-dimensional alignment. Hence, the rotation axis of CoRoT-2a is inclined by approximately 88°. While this impedes the reconstruction of latitudinal information of surface features, the existence of a planet crossing the stellar disk allows to access latitudinal information on spots beneath its path. During a planetary passage the surface brightness distribution is mapped onto the lightcurve as deformations of the transit profiles. As a consequence of the co-aligned orientation of the planetary orbit and the stellar spin, the surface band scanned by the planetary disk remains the same: the planet constantly crosses the latitudinal band between 6° and 26°. Accordingly, the stellar surface can be subdivided into two sections: the eclipsed section and the noneclipsed section (cf., Huber et al. 2009).

Our surface model subdivides the two individual sections into a number of "strips"; N_e is the number of strips in the eclipsed and N_n in the noneclipsed section, respectively. Each strip represents a longitudinal interval inside the latitudinal boundaries of the corresponding section. The layout of our surface model is shown in Fig. 1 of Huber et al. (2009).

3.1.1. Model resolution and error estimation

The problem of lightcurve inversion is well known to be ill-posed, so that the parameter space is usually further constraint by a regularization. One such regularization is the maximum entropy approach, applied, for example, by Lanza et al. (2009) in their analysis of CoRoT-2a.

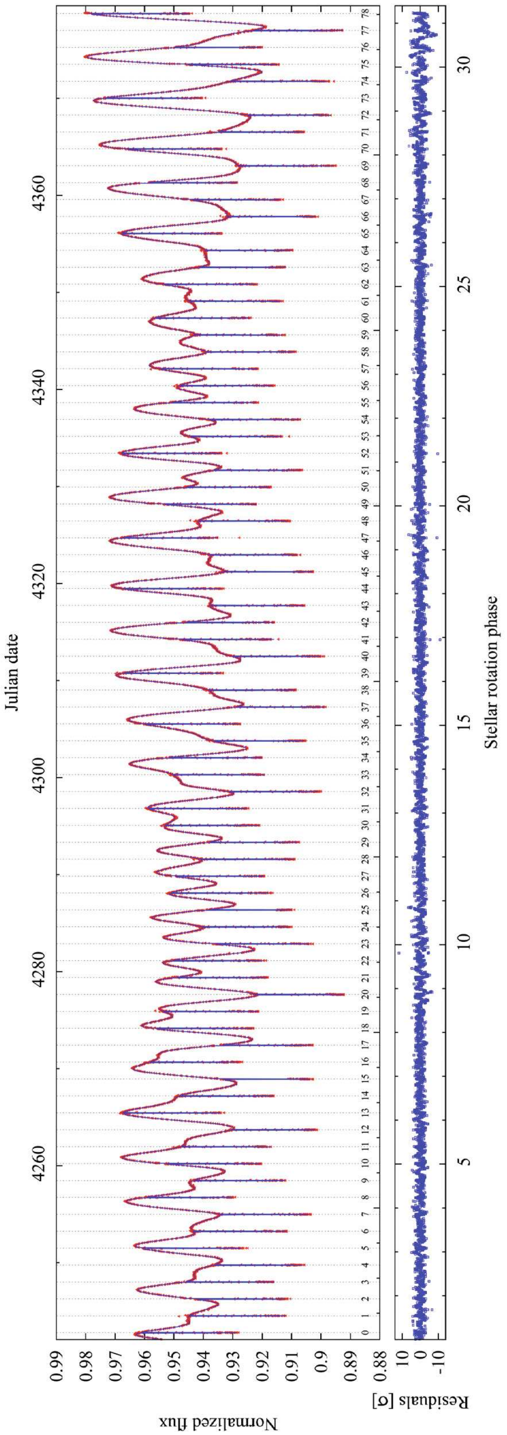

Fig. 1. Observations and best fit model for CoRoT-2. The transit numbers are plotted below the lightcurve; for a detailed presentation of the transits see Fig. 9. See Sect. 3.4 for discussion.

We use a Nelder-Mead (NM) Simplex algorithm for minimization (Press et al. 1992). Our model does not require any regularization because of its relatively small number of parameters. As discussed by Huber et al. (2009), we choose a number of strips balancing the improvement in χ^2 and the deterioration in uniqueness. For higher strip numbers, adjacent strips increasingly influence each other because brightness can be redistributed without significant loss of fit quality. In our error analysis we assume that there is a unique best-fit solution to our problem and that the NM algorithm approaches it to within the limits of its ability to converge. Starting from the yet unknown best-fit solution, brightness can be redistributed among the strips at the expense of fit quality. A set of Nelder-Mead fit runs will, therefore, provide a sequence of solutions with different realizations of this brightness redistribution.

We calculate 50 reconstructions with randomized starting points and adopt the average of all reconstructions as our most appropriate model. As an estimate for the error of the strip brightness, we use the standard deviation of the parameter values, obtained from the set of reconstructions.

We do point out that the averaged solution appears smoother than most individual reconstructions in the sense that the difference between adjacent strip brightnesses is smaller. This can be understood in the picture of brightness redistribution, because the brightening of one strip may preferably be compensated by darkening an adjacent one, which increases their contrast. This effect is largely canceled out by the averaging, which makes it appear much like a regularization of the solutions.

It may be criticized that the brightness error we use is largely determined by the ability of the NM algorithm to converge to a unique solution. We emphasize, however, that the χ^2 range covered by the 50 reconstructions exceeds that required for 'classical' error analysis, and the estimate will, therefore, remain rather conservative from that point of view.

Our test runs indicate that for our purpose the most appropriate number of strips to choose for the noneclipsed section is $N_\text{n} = 12$, which will be used in our analysis. Larger numbers of N_n appear to already oversample the surface significantly. The strip number for the eclipsed section is chosen to be $N_\text{e} = 24$ which approximately reflects the size of features that are resolvable inside of transits (Huber et al. 2009).

3.2. Normalization

The observations are normalized with respect to the ab initio unknown spot-free photospheric flux of the star, which is defined as maximum brightness $b_\text{phot} = 1$. Unfortunately, it is not trivial to obtain this photospheric flux level because spots are likely to be located on the visible disk at all times.

A possible solution for this problem is to adopt the maximum observed flux as photospheric. However, this presumably introduces an error because the brightest part of the lightcurve shows only the flux level of the stellar disk during the minimum observed spot coverage, which needs not be zero. Lanza et al. (2009) determine an average minimum of flux deficit of approximately 2.5%. Tests with slightly varying maximum brightness values in our reconstructions show no qualitative difference in the brightness distribution except for a change in the average *total* spot coverage; however, they show a significant decrease in χ^2 of the lightcurve reconstructions for a maximum brightness 1% to 2% larger than the highest observed flux. As a result we choose a photospheric flux level of 2% higher than the maximum observed flux. The entire lightcurve is normalized with respect to this value.

3.3. Lightcurve modeling

For analysis, the lightcurve is split into equally sized intervals, each covering one stellar rotation and three transits. Due to surface evolution detectable on timescales smaller than one stellar rotation, we choose to define a new interval after each transit. Thus, the resulting intervals overlap. Interval 0 contains the transits number 0 to 2, interval 1 contains the transits number 1 to 3, and so on. This way we end up with 76 lightcurve intervals which are individually reconstructed by our modeling algorithm.

Using fit intervals smaller than one stellar rotation could further reduce the influence of surface evolution. However, we need at least three transits in each interval to sufficiently cover the eclipsed section. Therefore, we always use a complete rotation for each reconstruction interval.

We use the fitting method presented in Huber et al. (2009). Each fit interval is rebinned to $94 \times 32 = 3\,008$ seconds for the global lightcurve and to 128 seconds inside of transits. Transit points are weighted with a factor of 10 higher than global points to give them approximately the same weight in the minimization process. We assume the planet to be a dark sphere without any emission; this seems to be a good approximation considering a secondary transit depth of about $(0.006 \pm 0.002)\%$ (Alonso et al. 2009). All other necessary parameters can be found in Table 1.

We introduce a penalty function to suppress reconstructed brightnesses above the photospheric value of one. Without this boundary the brightness of individual strips exceeds this limit in some reconstructions. Strips with values above unity must be interpreted as regions with a brightness greater than the (defined) photosphere; however, in this approach we want to consider only cool surface features, which was found to be a good approximation by Lanza et al. (2009). Several tests showed that this penalty function does not significantly alter the outcome of our reconstructions; it primarily prevents the minimization process from getting stuck in (local) minima outside the relevant parameter range.

To analyze the transits accurately, we require an "undisturbed transit profile", which means a profile corrected for the effects of stellar activity. This "standard transit profile" was determined by Czesla et al. (2009), where a planet size of $R_\text{p}/R_\text{s} = 0.172$ was found. With the planetary parameters derived by Alonso et al. (2008) no satisfactory fits to the transits and global lightcurve can be produced.

3.4. Results of the modeling

We present our lightcurve reconstruction in Fig. 1. It shows the observed CoRoT-2 lightcurve (red triangles), including the transits, and our reconstruction (blue solid line). The shown reconstructed lightcurve is a combination of all models for the 76 fit intervals; their overlaps were combined using a Gaussian weighting. Each transit is labeled with its number on the lower edge of the graph; a more detailed picture of their fits is given in Fig. 9, where we present all transits in a stacked plot.

Below the lightcurve the residuals $\sigma = (O - C)/\sigma_O$ (O-observed lightcurve, C-reconstructed lightcurve, σ_O-error of observation) are given. The mean values for σ_O are 1.8×10^{-4} outside and 6.9×10^{-4} inside of transits. Maximum values of the residuals are approximately $10\,\sigma$, which corresponds to a deviation of about 0.2% between the observed and reconstructed lightcurves. On average, the absolute values of residuals are $1.12\,\sigma$ or $O - C = 4.4 \times 10^{-4}$, respectively.

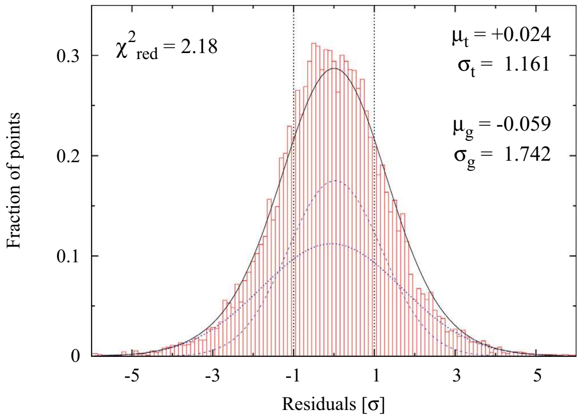

Fig. 2. Distribution of residuals σ between the observations and the best fit model (see Fig. 1). The overall distribution is the sum of two Gaussians, one coming from inside the transits (mean μ_t and width σ_t) and the other coming from outside of them (global, mean μ_g and width σ_g). For details see Sect. 3.4.

Figure 2 shows the distribution of residuals from Fig. 1. It is approximately Gaussian, although the underlying distribution is twofold: one component is a Gaussian distribution of residuals from inside the transits with $\sigma_t = 1.161$, and another broader component is coming from the residuals of the global lightcurve, which is significantly wider with $\sigma_g = 1.742$. The addition of both Gaussians reproduces the overall distribution of residuals accurately. We calculate $\chi^2_{\rm red} = 2.18$ from all residuals of the entire lightcurve.

The interpretation of $\chi^2_{\rm red}$ as an actual goodness-of-fit indicator is not straightforward in this case. An increase of the strip number should lead towards $\chi^2_{\rm red}$ values of 1. Test calculations show that our fit quality cannot be substantially improved beyond a certain level when the number of strips is increased. This level of $\chi^2_{\rm red}$ primarily reflects the evolution of the lightcurve within one stellar rotation, which cannot be improved within our static model, and which is especially visible in the global lightcurve ($\sigma_g \gg \sigma_t$). Unfortunately, it is very hard to quantify this effect.

3.5. Construction of brightness maps

In Fig. 3 we present maps of the temporal evolution of the brightness distributions. The left panel gives the brightness map for the noneclipsed, the right panel for the eclipsed surface section. The rows show the reconstructed brightness distributions for all 76 lightcurve intervals; each interval is labeled by the number of the first transit it contains. Due to the different resolutions in the two surface sections, we linearly interpolate the brightness values in each individual row; there is no interpolation applied between different rows. To generate the combined brightness map shown in Fig. 8 (left panel), the maps of the two separated sections are weighted, corresponding to their disk fraction of 0.79 for the noneclipsed and 0.21 for the eclipsed section, and added. The errors are combined the same way. Adjacent rows in our maps are not independent because the fit interval is only shifted by one transit (≈1/3 stellar rotation) when moving from one row to the next.

The errors are displayed directly below each map. For the brightness values of the global lightcurve fit (Fig. 3, left panel), the mean error is about 1%, for the transits (Fig. 3, right panel) it is approximately 3%. The errors in the latter map are larger (on average) and more inhomogeneously distributed because they also reflect the coverage of the eclipsed section by the transits; areas only marginally visible in transits cannot be reconstructed with high accuracy.

The stellar longitude scale of our maps runs backwards from 360° to 0°. This is due to our retrograde definition of the stellar longitude l compared to stellar phases ϕ_s; their relation is $l = (\phi_N - \phi_s) \cdot 360°$ (with an integer stellar rotation number $\phi_N = [\phi_s] + 1$).

The identification of significant structures in these maps deserves some attention. The brightness information is color coded using black color for the darkest structures and white for photospheric brightness. Considering the approximate mean error of each map, we indicate areas with a brightness significantly below unity with yellow color. Hence, not only black areas of these maps are spots but yellow structures represent a significant decrease in brightness as well.

4. Discussion

In this section we discuss and interpret the spot distributions of our brightness maps and their evolution. This involves quite a few different aspects, which are often difficult to disentangle, and on which we focus on individually in the following subsections.

4.1. Identifying physical processes and detection limits

Our brightness maps allow us to witness the evolution of the stellar surface and, to some degree, to discriminate between individual processes causing changes of the spot distribution: Emergence/dissociation, differential rotation, or migration of surface features leave potentially distinguishable signatures. Unfortunately, the high diversity of CoRoT-2a's surface and a limited resolution complicate the interpretation of these signatures.

On the eclipsed section the position of a feature is fairly well known and it is likely to be physically coherent. On the noneclipsed section it is not clear whether a feature is actually a single connected active region or a superposition of two (or even several) different regions.

Features on the eclipsed section provide a valuable reference point for the detection of differential rotation. Systematic longitudinal movements of spots in the transit map do not indicate differential rotation but rather a difference to the input rotation period. However, a comparison of transit and global maps could reveal different rotation periods on different surface sections.

Systematic longitudinal movements of structures in the global map do not necessarily indicate differential rotation either. A simultaneous decay and growth of two distinct active regions at different longitudes might leave a signature similar to a single differentially rotating active region. Therefore, the processes of differential rotation and spot evolution are hard to discern.

A very interesting scenario is the possibility to find spot migration due to the planet. If a spot moves from the noneclipsed to the eclipsed section, its signature also moves from the global to the transit brightness map. If present, such signatures are detectable in high quality brightness maps.

In the following discussion we attempt to attribute signatures in the brightness maps to the specific *processes* discussed above. Depending on the number of longitudinal strips used, map structures have an estimated error in longitude of about half the strip

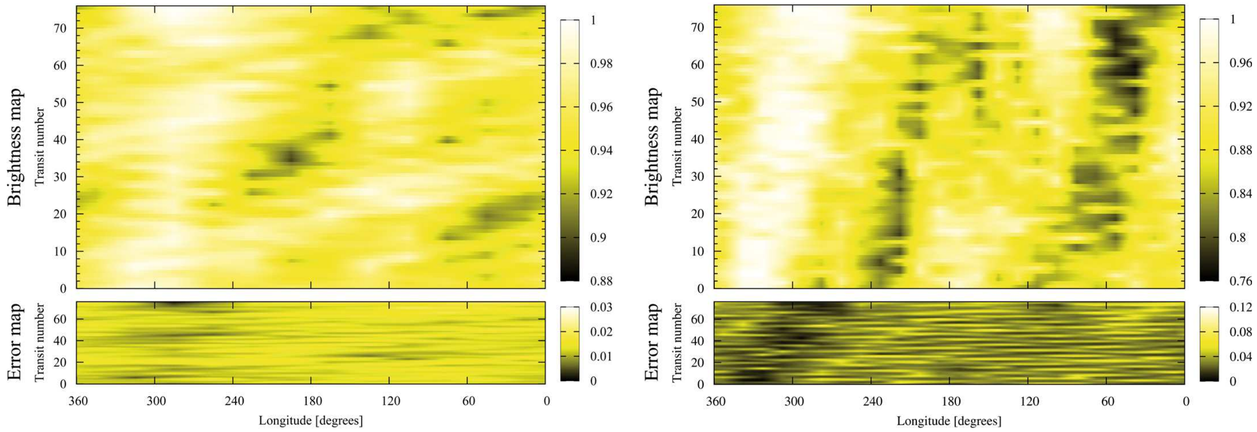

Fig. 3. *Left panel*: brightness map reconstructed from the global lightcurve (noneclipsed surface). *Right panel*: brightness map for the reconstructions of the transits (eclipsed surface). The combination of both maps is presented in Fig. 8. Each row presents the reconstructed brightness distribution of one fit interval; the transit number indicates the number of this interval's first transit. Each step in transit number equals a temporal step of 1.74 days. The brightness is color-coded, the maximum photospheric brightness is unity. The error maps at the bottom of each panel show the estimated reconstruction error. See Sects. 3.3 and 3.5 for details.

width, which is about ±7.5° for the transit and ±15° for the global map, respectively.

4.2. Spot coverage

The brightness maps of Fig. 3 show clear evidence of (a) a coverage of a large fraction of the surface with dark features and (b) a substantial evolution of this spot distribution within the roughly 140 days of observations. Considering the pronounced rotational modulation of the lightcurve, and the persistently changing shape between individual rotations, this result is hardly surprising. The lowest flux of the rotationally-modulated lightcurve is about 0.92 (modulo the uncertainty in lightcurve normalization, see Sect. 3.2); if the starspots were absolutely dark, they would still cover 8% of the disk. The largest peak-to-peak variation during one rotation spans from 0.98 to 0.92 indicating roughly 6% more spots on the darker hemisphere.

Using a spot contrast of $c_s = 0.7$, which is about the average bolometric contrast of sunspots (Beck & Chapman 1993; Chapman et al. 1994), we determine a maximum spot coverage of 37% on the eclipsed and 16% on the noneclipsed section. For the entire stellar surface a maximum and minimum spot coverage of 19% and 16% are derived.

Details on brightness values and spot coverage can be found in Fig. 4. The average brightness B is the mean brightness of each reconstruction interval. The top panel gives the ratio between the mean brightness of the eclipsed and noneclipsed sections, the second and third panel (from top) the eclipsed and noneclipsed brightnesses separately, and the bottom panel shows the variation of the total brightness $B_{\mathrm{Total}} = (1 - A) \cdot B_{\mathrm{ecl.}} + A \cdot B_{\mathrm{non-ecl.}}$ with $A = 0.79$. The associated spot coverage fraction is calculated using $(1 - B)/(1 - c_s)$.

Instead of converting brightness into spot coverage, we can also reverse the process. Assuming the darkest element of the transit map is entirely covered by one spot, the reconstructed brightness represents the spot contrast. One strip on the eclipsed section has a size of about 1% of the entire surface. We obtain a value of 0.76 for the darkest surface element of the transit map, which is not far from the solar spot contrast of 0.7. The minimum brightness of 0.76 can be translated into a temperature contrast of ~400 K between the spot and the photosphere, which is at $T_p = 5625$ K (Bouchy et al. 2008).

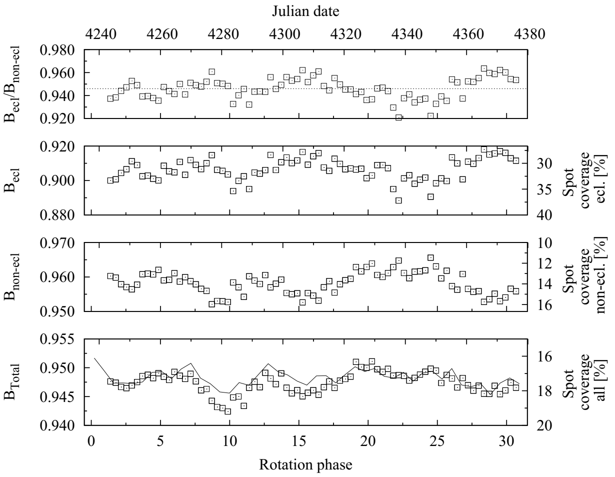

Fig. 4. Average brightness values of the eclipsed ($B_{\mathrm{ecl.}}$) and noneclipsed ($B_{\mathrm{non-ecl.}}$) sections for each reconstruction interval. The y-axes on the right show the corresponding spot coverage for a spot contrast of 0.7. *Top panel*: ratio $B_{\mathrm{ecl.}}/B_{\mathrm{non-ecl.}}$ of the mean brightnesses. *Second panel from top*: mean brightness and spot coverage for the eclipsed section. *Third panel from top*: mean brightness and spot coverage for the noneclipsed section. *Bottom panel*: total brightness B_{Total}; the black curve shows the results of Lanza et al. (2009) shifted by +9% (see Sect. 4.2).

4.3. Rotation period

For CoRoT-2a Lanza et al. (2009) determine a rotation period of (4.52 ± 0.14) d by means of the Lomb-Scargle periodogram, which the authors later refine to be $P_s = (4.522 \pm 0.024)$ days by minimizing the longitudinal migration of their active longitudes. We adopted P_s for our reconstructions. It is almost identical to the largest peak in the Lomb-Scargle periodogram (Fig. 5)

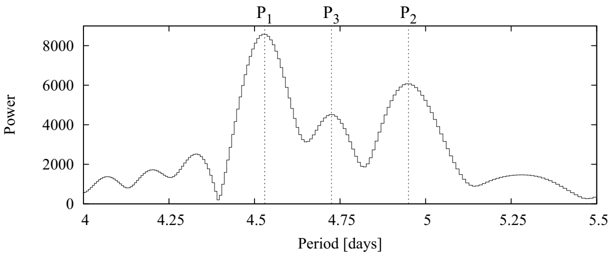

Fig. 5. Section of the Lomb-Scargle periodogram of the CoRoT-2 lightcurve containing the highest peak. The three peaks are labeled P_1 = 4.53, P_2 = 4.95, and P_3 = 4.72 days according to decreasing power. The adopted rotation period of our reconstructions, P_s = 4.522 days (Lanza et al. 2009), is close to P_1.

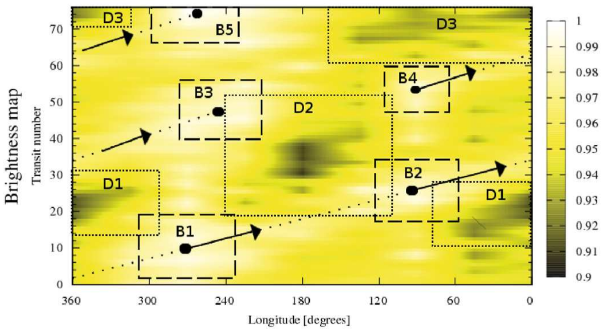

Fig. 6. The global surface map (left panel of Fig. 3) with pronounced dark and bright features marked and labeled D1 – D3 and B1 – B5, respectively. The dash-dotted line and the arrows indicate the tentative movement of bright regions (see Sect. 4.4).

centered at P_1 = 4.53 d. P_1 is accompanied by two other distinguishable peaks at P_2 = 4.95 d and P_3 = 4.72 d, which are related to structures in our surface maps as discussed in Sect. 4.4.

Since the planet crosses the stellar disk in a latitudinal band between 6° and 26°, spots on the eclipsed section must be located close to the equator. The approximate vertical alignment of the darkest features in the transit map indicates that low-latitude features rotate close to the adopted rotation period of 4.522 days used in our reconstructions. In contrast, features on the noneclipsed section do show longitudinal migration, which may be attributed to differential rotation of spot groups at latitudes $\gtrsim$30°. This finding suggests that active regions close to the equator dominate the modulation of the lightcurve.

A closer inspection of the transit map shows a small but constant longitudinal shift of about 60° over the entire 30 rotations. It is not only visible in the dark structures located at ~200° and ~60° longitude, but for the bright region at ~300° as well. As a consequence, these low-latitude features do not rotate exactly with a rotation period of 4.522 days but about 2° per rotation more slowly, which translates into a rotation period of approximately 4.55 days. Lanza et al. (2009) state a retrograde migration of their second active longitude corresponding to this rotation period.

We recalculated the surface reconstructions adopting a rotation period of 4.55 days. As expected the longitudinal shift previously detected in the transit map disappeared, but some features now seem to migrate in the other direction. Therefore, the exact rotation period of features on the eclipsed section is probably slightly smaller than 4.55 days. The global map changes accordingly when using a rotation period of 4.55 days; the brightness distribution reconstructed at larger transit numbers is shifted towards larger longitudes, but remains qualitatively the same, so that these maps are not presented separately.

4.4. Longitudinal movement / differential rotation

Some attributes of the global map suggest a longitudinal movement of surface structures; a labeling of particularly interesting regions is given in Fig. 6. Especially considering the inactive regions, the bright structure B1 at the bottom left appears to move from ~300° to ~100° (B2) within about 4 stellar rotations. It continues moving in the direction of decreasing longitude reaching roughly 240° near transit number 50 (B3). Regions B4 and B5 do not seem to fit well into the line drawn by B1, B2, and B3. However, a line connecting B4 and B5 roughly matches with the previously detected rotation period between 4.8 and 5.0 days. The tilted shape of the dark structure D1 roughly agrees with this range of periods as well. D2 indicates a smaller rotation period consistent with P_3.

Although such surface map characteristics do not necessarily prove differential rotation, they are certainly suggestive of differential rotation. Assuming now this to be correct, we will elaborate on its consequences. The largest rotation periods we obtain from structures of the global map lie between about 4.8 and 5.0 days. We studied the longitudinal movements of these structures on surface maps obtained from lightcurve reconstructions applying different rotation periods and always end up with similar results. An examination of CoRoT-2's periodogram reveals a splitting up of the highest peak into three components: P_1 = 4.53 d, P_2 = 4.95 d, and P_3 = 4.72 d (see Fig. 5). It is striking that P_2 is close to the rotation period determined from tilted structures in our global map.

If these rotation periods do arise from differential rotation, we can estimate a lower limit of its strength. The rotation period of eclipsed spots close to the equator is consistent with the highest peak P_1 = 4.53 days of the periodogram, the largest periods detected in the global map are around P_2 = 4.95 days; therefore, we adopt this period for the most slowly rotating active regions. This way we determine a lower limit of $\Delta\Omega > 0.1$ rad/d or $\alpha > 0.08$. This is consistent with values expected for stars with temperatures and rotation periods similar to that of CoRoT-2 (Barnes et al. 2005). Using a 3-spot model approach, Fröhlich et al. (2009) derive an estimate of $\Delta\Omega > 0.11$ rad/d, which is in good agreement with our result.

Although the peaks in the periodogram fit nicely in with our brightness maps, attributing them to three active regions with associated rotation periods may not be fully adequate. We simulated several lightcurves with differentially rotating spots and examined their periodograms. Although the main peak splits up into different components, the periodogram does not necessarily map the exact rotation periods of the differentially rotating spots to the peak barycenters. An exhaustive analysis of the periodogram is beyond this work's scope, but the above approach may serve as an approximation, and it shows that the characteristics of the periodogram can be aligned with surface map attributes.

As an alternative, or maybe extension, to the interpretation in terms of differential rotation, an evolution of the global activity pattern should be considered, which does not invoke longitudinal movement of individual surface features, but a redistribution of strength between active regions. The spot distribution on the global map suggests sudden longitudinal relocations of the most active feature. For the first ~25 transits the dominant spotted region D1 keeps its position at ~30° showing an apparent movement towards smaller longitudes at the end of this interval. Afterwards the dominant active region is found approximately 180° apart from the previous position in region D2. Such 180°-jumps, or rather "hemisphere-jumps", as the value of 180° should not be taken too seriously here, are found for inactive (bright) regions as well.

An appealing explanation for this apparent shift is a change of the relative strength of two active regions, which does not involve movement of any of the structures themselves. These jumps are possibly a sign for some flip-flop scenario as already claimed for other stars (Jetsu et al. 1993; Korhonen et al. 2001), where the relative strength between two active longitudes is changing suddenly and periodically. The timescale of these "jump periods" derived from our global brightness map is roughly 10 stellar rotations; however, this is not seen in the transit map.

4.5. Lifetimes of features

Both the global and the transit map provide the possibility to measure lifetimes of spotted regions. For the noneclipsed section it is not clear whether a dark structure actually is a single connected active region or a superposition of several individual ones at roughly the same longitude but completely different latitudes.

The transit map shows a high stability of the spot positions. One group of spots is located between 200° and 240°, which is stable up to transit number 35; then the spot coverage seems to decrease for about one stellar rotation. Afterwards the spot distribution becomes more complicated and spreads over a larger area. The left part of this more complex region, at about 210° longitude, is probably a continuation of the preceding active region; however, at about 160° longitude a new, clearly separated group of spots appears. This latter structure appears to have a lifetime of approximately 10 stellar rotations, which would be in good agreement with timescales observed on the global map.

Another group of spots is located between 0° and 100°. At the beginning of the observation these spots are spread over this larger interval of about 100° on the eclipsed section; later, approximately after transit number ~50, they seem to concentrate in a smaller interval. This active region seems to have a significant fine structure in time, which might indicate smaller lifetimes of individual spot groups; however, those structures could also be artifacts of the reconstruction algorithm. We prefer the interpretation that this active region, and the left side of the other active region, are persistent over all 30 rotations, although they probably contain smaller spots undergoing significant evolution on much shorter timescales.

The left side of both maps (around 300° in longitude) shows bright regions which are least covered by spots during all observations, indicating a lifetime of half a year for this "inactive longitude". For the darkest structures of the global map, maximum lifetimes of about 10 to 15 stellar rotations can be estimated. This is in agreement with the results of Lanza et al. (2009), who determine a lifetime of ≈55 days (=12 stellar rotations) for active regions, and identify this time span with the "beat period" visible in the lightcurve.

Although there are some structures in the transit map that suggest smaller lifetimes than half a year for individual spot groups, the lifetimes of features on the two different surface sections seem to be different. A direct comparison of the global and the transit map is shown in Fig. 7. The active regions on the eclipsed section remain active all the time despite their possibly significant fine structure. In contrast, active regions on the noneclipsed section evolve faster showing more pronounced changes and a longitudinal movement compared to the spots on the eclipsed section. The reason for the apparent lifetime difference is not clear. Possibly the darkest structures represent only a superposition of several spotted groups at about the same latitude. If these groups change their mutual longitudinal positions, or a fraction of the spot groups dissolves, the dark structures in our maps would brighten. In this case the darkest structures would only represent special configurations of the spot distribution and their "lifetimes" in our maps would not be directly connected to the lifetimes of individual active regions on the surface.

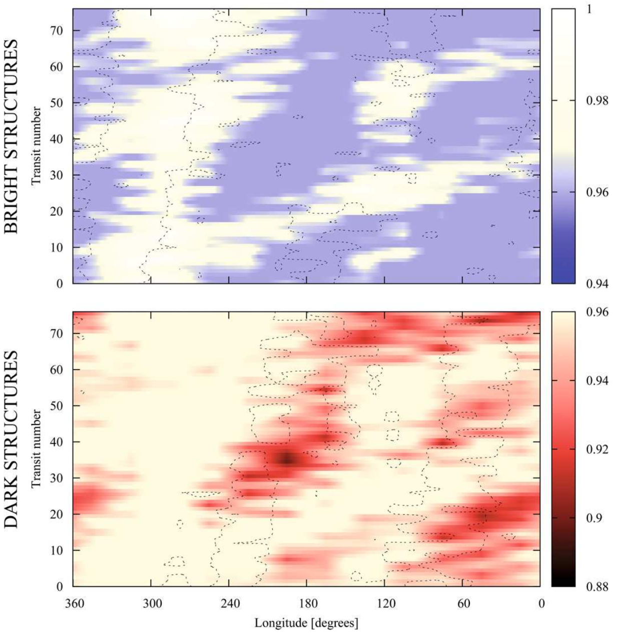

Fig. 7. Direct comparison of the two brightness maps of Fig. 3. The global map is drawn in color, structures of the transit map are shown with contour lines. *Upper panel*: map of bright structures in the global map with $b_{\text{non-ecl.}} > 0.95$. The contour line delimits brightness values of the transit map above $b_{\text{ecl.}} = 0.94$. *Lower panel*: map of dark structures with $b_{\text{non-ecl.}} < 0.95$. Here the contour lines indicate a transit map brightness of $b_{\text{ecl.}} = 0.87$.

The stable vertical alignment of features in our transit map cannot be caused by a systematically incorrect transit profile used in our reconstructions. The transits do not always cover exactly the same part of the eclipsed section, which is also visible in the error distribution of the transit map; dark structures indicate where the coverage is best, bright where it is worst. Thus, an error introduced by the transit profile would be distributed over the entire map.

4.6. Comparing global and transit maps: spot migration?

Finally, there is the possibility of detecting signatures of spot migration – the movement of spots from the equator to the poles or vice-versa – in our brightness maps. Figure 7 presents the direct comparison of the brightest structures (upper panel) and the darkest structures (lower panel) of the global and the transit map. Especially the dark structure D2 (see Fig. 6) in the middle of the lower panel's map suggests that features on the eclipsed

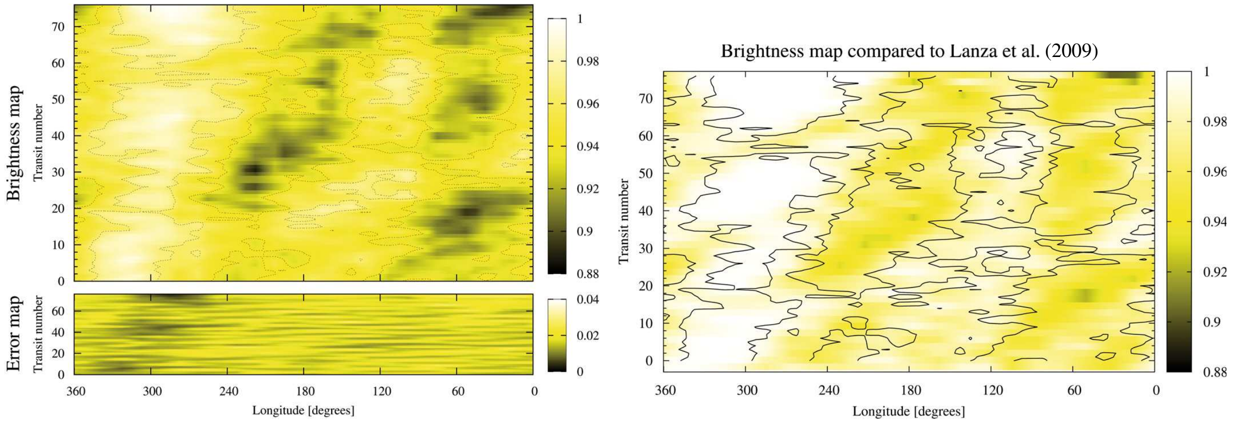

Brightness map compared to Lanza et al. (2009)

Fig. 8. *Left panel*: brightness distribution of the *entire* surface for all reconstructed intervals; it represents a combination of both the global and the transit map. The error for each bin of the brightness map is shown below. *Right panel*: comparison of our brightness distribution (contours) to the reconstruction of Lanza et al. (2009), which are shown in color coding. See Sect. 4.7 for details.

and noneclipsed sections are related. For the first 30 transits there is a dark feature of the transit map at this longitude, then it starts to disappear when D2 becomes darker. This reflects a scenario where a spot group moves from the eclipsed section to the noneclipsed. After transit number 40, D2 starts to disappear while other structures appear on the eclipsed section. If this really represents a case of spot migration, the spot group either moves back onto the eclipsed section, or it stays outside and new spots emerge under the transit path.

A similar observation can be made concerning the bright structures in the upper panel of Fig. 7. The bright structures in the transit map between 60° and 120° alternate with the bright regions B2 and B4. First there is a bright structure on the eclipsed map below region B2, then there is a little bit of both between B2 and B4, and after region B4 a bright structure is emerging in the transit map.

It is impossible to prove whether these signatures really represent spot migration; probably some of them are due to other processes, e.g. short-term evolution of spotted regions. Nevertheless, there is a similarity to what one would expect to see in brightness maps from surfaces showing spot migration. A behavior supporting a shift of spots from the eclipsed to the noneclipsed sections (and vice-versa) can be observed in Fig. 4 (second and third panel). It suggests a correlation between the mean brightnesses of the two sections; when the average brightness of the eclipsed section decreases, it increases on the noneclipsed part. However, this correlation does not necessarily prove a steady motion between the two sections and might as well indicate that vanishing spots just reappear somewhere else.

4.7. Comparison to previous results

Figure 8 (left panel) displays the combined brightness map derived from both the eclipsed (transit map) and noneclipsed sections (global map) of Fig. 3: the single maps are multiplied by their corresponding surface fractions (0.21 for the eclipsed and 0.79 for the noneclipsed) and added.

Lanza et al. (2009) present a map of the surface evolution derived from a fit to the global lightcurve (their Fig. 4) not including the transits. In the right panel of Fig. 8 we present a comparison of their results to ours. Since we do not use filling factors, we translated their map into brightnesses using their spot contrast of 0.665. We take the resulting map (color coding) and superimpose it on our combined map from both the eclipsed and noneclipsed sections (contours). In the left panel of Fig. 8 the same contour lines are drawn to provide a better comparison. Lanza et al.'s and our results show good agreement, although a perfect match in fine-structure is neither found nor expected. Dark and bright structures are located at very similar positions and the shapes are consistent.

Adding up the brightness values of each reconstruction interval of the map in Fig. 8 (left panel), we can study the variations of the mean total brightness B_{Total} of the star. This is presented in Fig. 4 (bottom panel). With a maximum of $B_{\mathrm{Total}} = 0.951$ and a minimum value of 0.942, the maximum difference between the highest and lowest average total brightness is only about 1%, which is much less than the maximum brightness differences within the brightness maps. This implies that the star as a whole does not change its overall spot coverage as dramatically as it redistributes it; when spots disappear, other spots show up. The solid line in the panel gives the comparison to the results of Lanza et al. (2009). We translated their values to our spot contrast of 0.7 and shifted it by a constant spot coverage of +9% to match our points. Our average spot coverage of 17.5% is roughly twice as high. Although, a 9% shift seems to be enormous, about 80% of it (+7%) can be attributed to a different normalization of the lightcurve and, thus, photosphere. While Lanza et al. (2009) define the maximum flux in the lightcurve as their photospheric level, our photosphere is 2% brighter (cf. Sect. 3.2), which has to be compensated by spots. We attribute the remaining 2% to the differences in the adopted models. In particular, we use longitudinal strips and spots can only be distributed homogeneously across a strips, while Lanza et al. (2009) localize the spots in 200 bins on the surface.

Previously, we detected an average brightness under the eclipsed section (6 ± 1)% higher than on the noneclipsed section (Huber et al. 2009). This value is redetermined from the reconstruction of the *entire* lightcurve presented in this paper. It decreases to (5.4 ± 0.9)% (see top panel of Fig. 4).

4.8. Brightness maps and lightcurve modulation

It is striking that the rotational variations of the star are additionally modulated with a beat period about a factor 10 to 15 larger. During the maxima of this large-scale modulation (at about transit numbers 15, 45, and at the end of the lightcurve), the minima

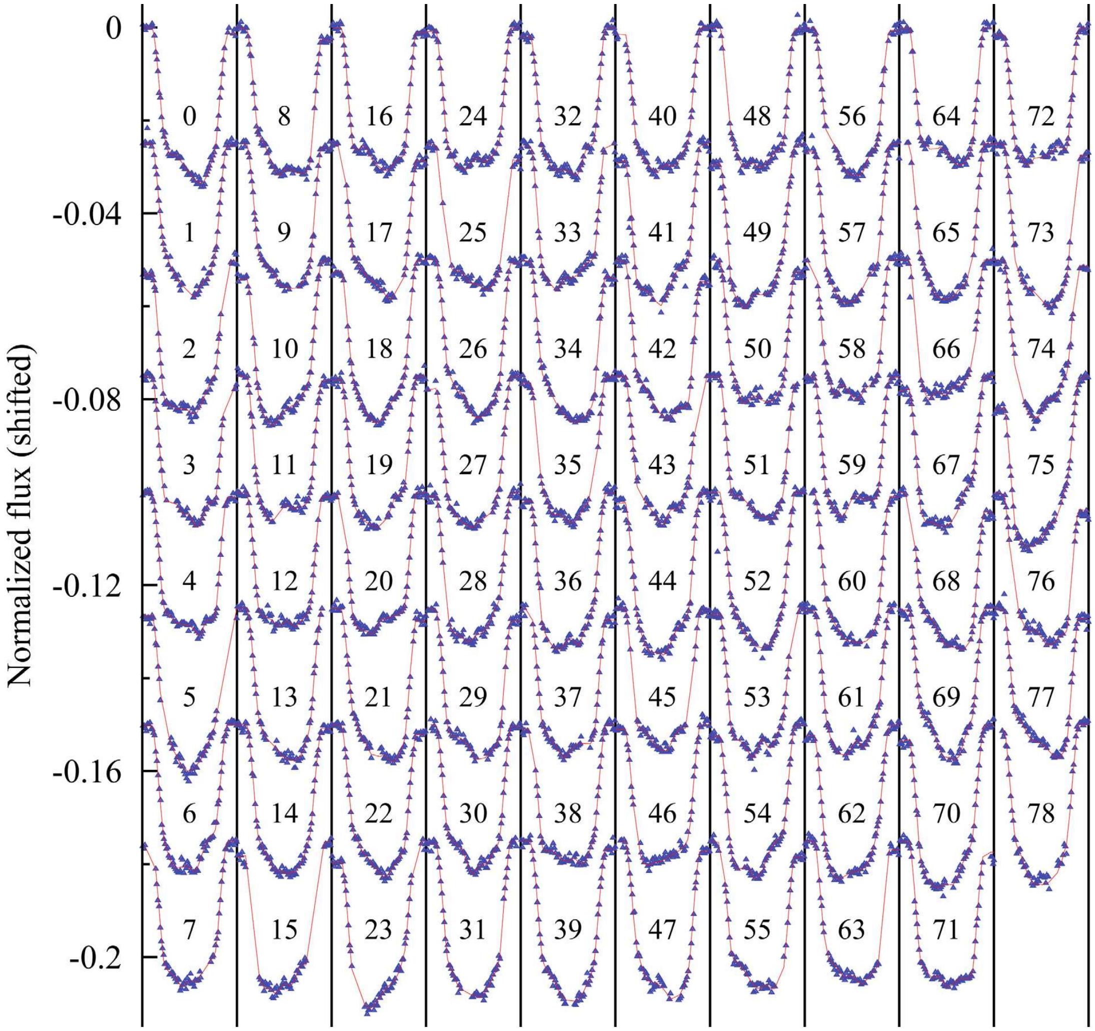

Fig. 9. Observation (blue triangles) and reconstruction (red solid line) of 79 transits from the CoRoT-2 lightcurve. The first transit of each column is shifted to a continuum of zero, each subsequent transit is shifted by −0.025. The number of each transit is annotated inside the plot. See Fig. 1 for the entire lightcurve.

of the stellar rotation are deep and regular, i.e., the lightcurve has only one distinct minimum per rotation. During the minima of this beat period (at about transit numbers 30 and 60), the rotational modulation is flatter and more complex; the minima are split up in two. The beat period maxima indicate the existence of one large active region or longitude dominating the stellar surface. The minima indicate that two smaller active regions at significantly different longitudes imprint their signatures onto the lightcurve leaving double-peaked structures during one stellar rotation. This means dark regions are redistributed on timescales of 10 to 15 stellar rotations from essentially one large feature to at least two smaller, longitudinally separated ones, and then back to a large one.

This is also observable in our brightness maps. Figure 8 shows a change of the dominant surface feature from ~60° to ~220° at about transit number 20. Earlier the lightcurve was dominated by one large active longitude leading to one broad minimum during each rotation. During the transition phase, especially around transit number 25, the lightcurve minima become double-peaked. After transit number 30 the activity center of the active longitude at 220° moves to about 180° and, thus, closer to the other active longitude at about 60°, which has not entirely disappeared and starts to grow stronger again. Because the active longitudes are closer now, the minima grow deeper; additionally, the bright region at 300° becomes larger and the maxima rise.

Again there are double-peak structures between transit numbers 55 and 60 for the same reasons. The decrease of the strong maxima is primarily due to the temporary change of the bright longitude at 300°. Interestingly, the amplitude and width of the minima become even larger at the end of the lightcurve, where the active longitudes first move closer together. In the end, the feature at ~20° becomes dominant spreading over almost 60° in longitude and leading to very low lightcurve minima.

The main reason why the rotation period of the star is so nicely indicated by almost constantly separated maxima of the lightcurve – despite the pronounced surface evolution – is that the on average brightest part of the surface, located on the inactive longitude at 300°, remains stable at its position.

5. Conclusions

We present a reconstruction of the complete CoRoT-2 lightcurve – including transits – covering about 140 days or 30 stellar rotations. In contrast to previous work, both the transit profiles and the rotationally-modulated global lightcurve are fitted simultaneously leading to a *consistent* solution for the entire lightcurve. From the transits the brightness distribution on the eclipsed surface section is recovered, which is the part of the surface between 6° and 26° latitude constantly eclipsed by the planet. The noneclipsed section is reconstructed from the rotational modulation.

The evolution of the spot distributions on both surface sections is presented in two maps showing the surface brightness distribution as a function of time. The composite map, which shows the evolution of the entire surface, is juxtapositioned with previously published results. The results are found to be in agreement taking into account different modeling approaches and assumptions.

The transit map shows two preferred longitudes densely covered with spots and separated by approximately 180°. Both active regions persist for the entire observing time of ~140 days, although they undergo significant evolution in size, structure, and brightness. In the transit map they show a constant retrograde movement indicating that the adopted stellar rotation period of $P_{\rm s} = 4.522$ days does not exactly describe their rotation. We determine that these low-latitude features rotate at a period of approximately 4.55 days, which is also true for the long-lived inactive longitude at ~300°.

The global map is more complex than the transit map presumably because the structures it describes represent a superposition of features at similar longitudes but different latitudes. Usually it shows only one dominant dark feature at a time, which changes position after approximately 10 to 15 stellar rotations. Again these dominant features are separated by about 180° in longitude. A persistent inactive longitude exists at about 300° similar to the one in the transit map and at about the same position. The global map indicates that there are features located on the noneclipsed section with significantly larger rotation periods than 4.522 days. This suggests the presence of differential rotation with spots moving more slowly at high latitudes than at low latitudes. We estimate a differential rotation of $\Delta\Omega > 0.1$ or $\alpha > 0.08$, respectively.

Assuming a spot contrast of 0.7, the spot coverage of the eclipsed section reaches a maximum of 37%, which is more than twice as large as the maximum on the noneclipsed section. *On average* the eclipsed section is (5 ± 1)% darker than its noneclipsed counterpart. Sunspots are located within ±30° around the solar equator. Similarly, our results indicate that spot groups on CoRoT-2 are also concentrated in a low-latitude "active belt".

Acknowledgements. We thank A. F. Lanza for kindly providing us with their results for comparison. K.H. is a member of the DFG Graduiertenkolleg 1351 *Extrasolar Planets and their Host Stars* and acknowledges its support. S.C. and U.W. acknowledge DLR support (50OR0105).

Note added in proof: Late in the review process, we became aware of a paper by Silva (2003, ApJ, 585, L147) where planetary eclipse mapping is modeled using images of the Sun. Contemporaneously to our work, Silva-Valio et al. (2010, A&A, 510, A25) used a very different approach to examine the transits of the CoRoT-2 lightcurve for properties of starspots.

References

Alonso, R., Auvergne, M., Baglin, A., et al. 2008, A&A, 482, L21
Alonso, R., Guillot, T., Mazeh, T., et al. 2009, A&A, 501, L23
Auvergne, M., Bodin, P., Boisnard, L., et al. 2009, A&A, 506, 411
Barnes, J. R., Cameron, A. C., Donati, J.-F., et al. 2005, MNRAS, 357, L1
Beck, J. G., & Chapman, G. A. 1993, Sol. Phys., 146, 49
Bouchy, F., Queloz, D., Deleuil, M., et al. 2008, A&A, 482, L25
Chapman, G. A., Cookson, A. M., & Dobias, J. J. 1994, ApJ, 432, 403
Czesla, S., Huber, K. F., Wolter, U., Schröter, S., & Schmitt, J. H. M. M. 2009, A&A, 505, 1277
Fröhlich, H., Küker, M., Hatzes, A. P., & Strassmeier, K. G. 2009, A&A, 506, 263
Gillon, M., Lanotte, A. A., Barman, T., et al. 2010, A&A, 511, A3
Huber, K. F., Czesla, S., Wolter, U., & Schmitt, J. H. M. M. 2009, A&A, 508, 901
Jetsu, L., Pelt, J., & Tuominen, I. 1993, A&A, 278, 449
Korhonen, H., Berdyugina, S. V., Strassmeier, K. G., & Tuominen, I. 2001, A&A, 379, L30
Lanza, A. F., Pagano, I., Leto, G., et al. 2009, A&A, 493, 193
Pont, F., Gilliland, R. L., Moutou, C., et al. 2007, A&A, 476, 1347
Press, W. H., Teukolsky, S. A., Vetterling, W. T., & Flannery, B. P. 1992, Numerical recipes in C. The art of scientific computing, ed. W. H. Press, S. A. Teukolsky, W. T. Vetterling, & B. P. Flannery (Cambridge University Press)
Rabus, M., Alonso, R., Belmonte, J. A., et al. 2009, A&A, 494, 391
Snellen, I. A. G., de Mooij, E. J. W., & Burrows, A. 2010, A&A, in press
Wolter, U., Schmitt, J. H. M. M., Huber, K. F., et al. 2009, A&A, 504, 561

Part III

Conclusions

Chapter 7

Summary and outlook

"Und dann folgte ein Durcheinander von Hypothesen, man frischte die alten auf, führte unwesentliche Änderungen ein, präzisierte oder verallgemeinerte sie, so dass die bis dahin trotz ihres Umfangs übersichtliche Solaristik immer verworrener wurde und sich in ein Labyrinth voller Sackgassen verwandelte. In einer Atmosphäre allgemeiner Gleichgültigkeit, Stagnation und Lustlosigkeit schien ein zweiter Ozean aus nutzlosem Papier den auf der Solaris durch die Zeit zu begleiten."

Kris Kelvin
Excerpt from the book *Solaris*
written by Stansilaw Lem (1961)
(Deutsche Übersetzung von Kurt Kelm, 3. Auflage 1986, Verlag Volk und Welt, Berlin 1983)

"In light of the lingering uncertainties with a map determined by any one technique and the deficiencies inherent in any one technique, it would help enormously to compare and/or combine information derived from Doppler imaging and light curves and eclipsing binaries, using the same star and data taken contemporaneously."

Douglas S. Hall
Excerpt from his paper *What we don't know about starspots*
(Hall 1996)

7.1 A new era of measurements

Compared to the detection and analysis of extra-solar planets, the analysis of solar and stellar activity is an old discipline. Data of solar activity have been collected for hundreds of years, the numbers of records are still rising enormously, and the quality continues to increase constantly. However, the understanding of these observations is difficult because the related physical processes are very complex.

Few developments in astrophysics had – or rather will have – as much impact on the study of starspots as the new space-based photometry missions CoRoT and Kepler. They assist to identify hundreds, probably even thousands of active stars with a wide range of properties and monitor their brightnesses with high precision for months or even years. Possibly, these instruments will even detect small spots the size of sunspots on solar twins and enable researchers to study the surface features of another Sun.

Until now the details of our models concerning surface inhomogeneities, especially on small scales, are mostly based on data from the Sun. Uninterrupted observations of stars for many consecutive rotations are hardly possible from ground-based observatories. Long-term observations of large samples of stars concerning stellar activity exist, as, e.g., presented in Baliunas et al. (1995) for chromospheric variations in 111 stars, but have been rather rare for starspots so far. These new high-precision data sets will show whether our recent models and ideas about stellar activity – especially about starspots – are supported by a high number and a broad range of stars. They will help us to further understand the bigger concept of activity and, hopefully, reveal the connection between the Sun and the stars.

7.2 Synergetic effects of combining data

In his review 'What we don't know about starspots' (Hall 1996), Hall wrote that a combination of different techniques and *contemporaneous* data would help enormously to precisely analyze starspots (see quote at the beginning of this chapter). One basic idea of my thesis was to take this one step further using the exceptionally accurate data of space-based photometry and ground-based radial velocity measurements. Our understanding of starspots will greatly improve when we combine DI, lightcurve analysis, planetary eclipses, and RV measurements of the same star – with at least some of them taken *simultaneously.*

Especially landmark objects as CoRoT-2 provide the best opportunities to obtain high-resolution surface images of stars. Planetary eclipse mapping is a powerful tool, which will be available more frequently in the near future for several (active) stars. It will give us access to the fine structure of starspots and reveal the distribution and evolution of spots in specific regions on the stellar surface with unprecedented precision. A combination with high-resolution spectra would further boost the amount and accuracy of information retrieved.

Another important aspect of my thesis was the question how much yet unused information lies in already collected data, and data that will be collected for a different purpose in the near future. High-precision photometry of hundreds of thousands of stars is obtained but mainly used for the detection of transiting planets. All transit-based planet detections must be confirmed using the RV technique; there are many high-precision RV measurements of stars primarily used to find or confirm a planet. Lightcurves and RV curves of many stars are already taken and researchers should use them for activity studies as well.

Clearly, our analysis of starspots would even more benefit from these data sets if certain requirements were fulfilled. RV measurements naturally are scheduled to densely cover the planetary orbit and/or the transit (Rossiter-McLaughlin effect). For activity studies, a sufficient coverage of the stellar rotation would be required as well. Simultaneous observations of lightcurves and RV curves allow us to identify spots in both data sets and increase our accuracy.

Such observations are not only important for the study of stellar activity itself, but are also important for the detection of planets and the precise determination of planetary parameters – at least around active stars.

When the accuracy is limited by signatures of activity in the data, which is already the case for many stars that are excluded from planetary search programs for exactly that reason, the activity must be modeled and removed from the data. Then planets around very active stars – and, probably even more important, small Earth-like planets around moderately active stars like our own Sun – can be found. A co-operation between these scientific communities will not only result in interesting collateral discoveries, but it will be indispensable for planet searches around active stars.

7.3 Summary

The results of my PhD thesis are summarized in the following paragraphs.

1 The example of V889 Her shows that solar-type, fast rotating stars can have extremely large and long-lasting active regions. Doppler images, which are snap-shots of the spot distribution, are used to compute the expected activity-induced RV signal, which is compared to long-term high-accuracy RV measurements. The active regions are clearly identified in the RV measurements, which significantly improves their understanding. This showed that the combination of different data sets – in this case Doppler Imaging, photometry, and RV measurements – indeed yields synergetic effects.

2 Effects of stellar activity should generally *not* be neglected in the analysis of planetary transits for stars showing pronounced activity signatures. In the case of CoRoT-2, spots significantly influence the determination of planetary parameters as, e.g., the size of the planet R_p. Furthermore, the correct treatment of activity improves the understanding of the true errors of derived planetary parameters, which are much higher than suggested by the statistical errors. Finally, an undisturbed transit profile – where the stellar activity is mainly removed – is essential for the reconstruction of spots from the lightcurve.

3 A consistent *simultaneous* reconstruction of rotational modulation and transit deformations of a complex lightcurve as that of CoRoT-2 is possible. This novel technique, which had not been applied before, considers the effects of spots both under the eclipsed section of the star and outside of it. The reconstructed spot distribution and its temporal evolution on the noneclipsed (global map) and the eclipsed section (transit map) is presented in Fig. 7.1.

4 The resolution of the eclipsed section of CoRoT-2, which is scanned by the planet, is much higher than on the noneclipsed section. Because the planet crosses the stellar disk close to the equator, and its exact path is known accurately, low-latitude spots are localized with high precision. Individual spots are detected, their exact positions are determined, and their evolution is traced for almost half a year. From two persistent active longitudes, and one inactive longitude, a rotation period for low-latitude spots

of $P = 4.55$ d is determined. A periodogram of the lightcurve suggests a significantly smaller value of $P = 4.53$ d.

5 The temporal evolution of spots on the noneclipsed section of CoRoT-2 is reconstructed as well, showing a behavior different from the eclipsed section. Active regions located there seem to have shorter lifetimes. Additionally, the relative strengths of active regions switches periodically from one active longitude to the other; this is sometimes referred to as *flip-flop scenario.* The active regions show larger rotation periods than on the eclipsed section indicating the presence of differential rotation with a strength of $\Delta\Omega \gtrsim 0.1$ rad/d or $\alpha \gtrsim 0.08$, respectively.

6 On average, the spot density on the eclipsed section of CoRoT-2 is (5 ± 1) % higher than on the noneclipsed section. This indicates the existence of an 'active belt' close to the equator similar to the active region around ±40° latitude on the Sun. At maximum, 37 % of the eclipsed section is covered by spots. Compared to the solar spot brightness $\mathrm{b} = 0.7$, we determined a similar spot brightness of $\mathrm{b} = 0.76$ on CoRoT-2.

7.4 Outlook

Many new ideas came to my mind during the course of this thesis, and some tasks were left unfinished. This section summarizes a few of these ideas and tasks, and shows how this work could be continued in the near future.

7.4.1 Starspots

1 The lightcurves obtained by the CoRoT satellite show many CoRoT-2-like stars with similar brightness variations. This is certainly also true for many objects in the Kepler field of view. A detailed analysis of individual stars of this 'type' or a statistical approach on a high number of these stars will give important insights into their characteristics. Possibly, it even turns out that they indeed form a special class of stars.

2 The analysis of RV variations for signatures of activity is still neglected. Primarily, this is seen as a nuisance when other interests are pursued, but the potential for activity studies – maybe even reconstructions of surfaces maps from high-precision RV measurements – is high.

3 A combination of RV curves and lightcurves leads to significantly better surface reconstructions than using only one of them. Some tests showed that we can recover the latitude of spots from simultaneous RV and lightcurve data set whereas this was not possible for the lightcurve alone. RV measurements simultaneous to CoRoT lightcurves are difficult, because CoRoT changes its field of view every half a year; however, this is possible for targets of the Kepler mission.

4 Using RV measurements to study starspots is certainly not the best way to recover information, although it is simple and practicable. To retrieve the maximum of information from the spectral lines, their exact deformation – and not just their apparent

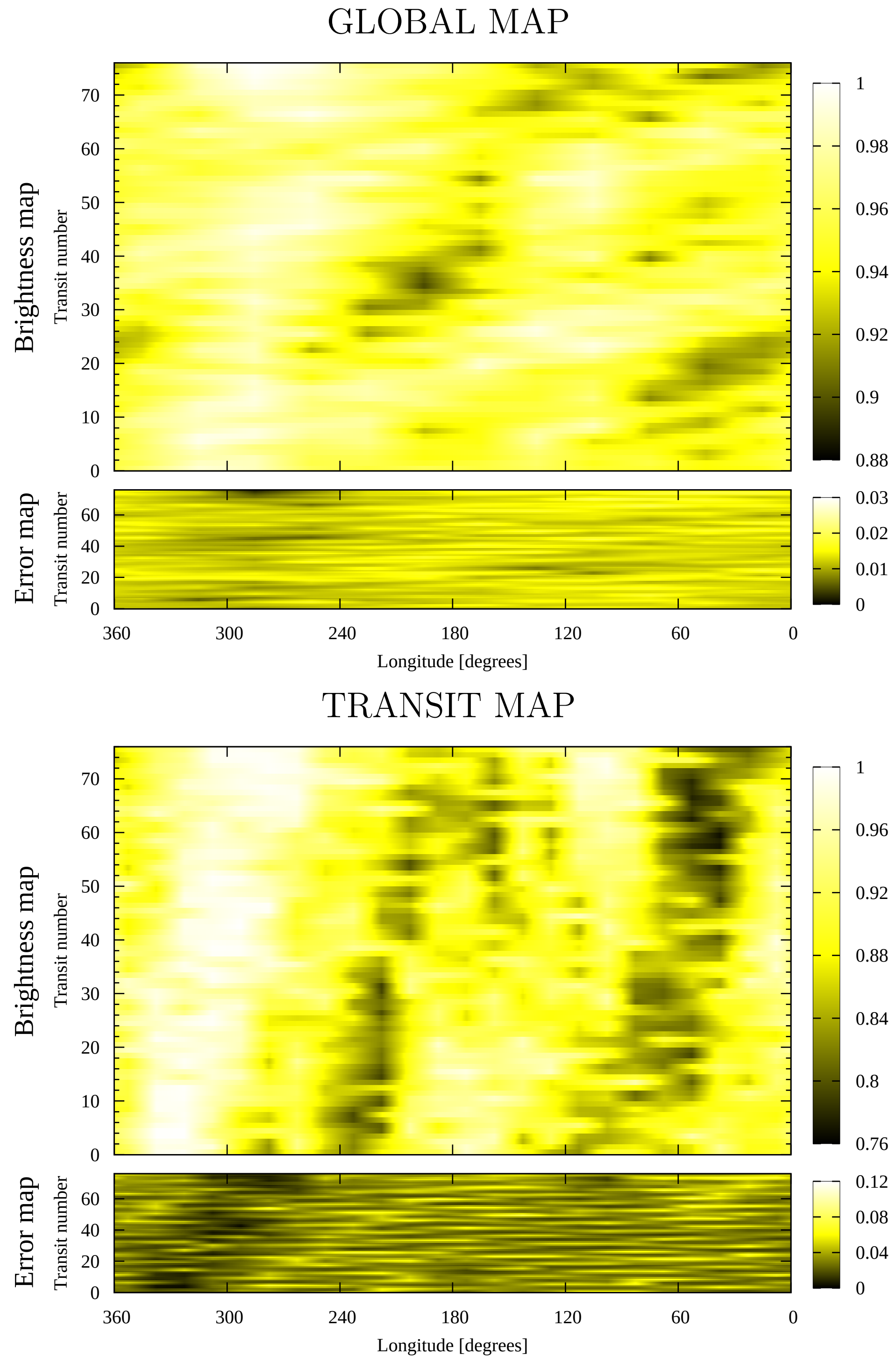

Figure 7.1: Brightness maps of CoRoT-2 showing the temporal evolution of the surface. *Upper panel*: Map reconstructed from the global lightcurve (noneclipsed surface). *Lower panel*: Map for the reconstructions of the transits (eclipsed surface). Each step in transit number equals a time step of 1.74 days. For further information see the publication in Sect. 6.3.

line shift – must be modeled using Doppler Imaging. However, DI on data taken for RV measurements is virtually impossible because either the S/N is too low, the spectral resolution is not high enough, the spectrum is contaminated by, e.g., a superimposed Iodine spectrum, etc. Furthermore, most targets of RV measurements are slow rotators, because in these cases the precision is high, whereas DI requires fast rotators.
To use Iodine spectra of stars with $v \sin(i) \gtrsim 20$ km/s for DI, it is necessary to develop a DI code that can handle the superimposed Iodine spectrum.

5 Because DI requires rapidly rotating stars, high-resolution surface images of slow rotators are extremely rare. In the case of CoRoT-2, the low rotation velocity seems to prevent the reconstruction of high-resolution surface maps with DI. Techniques to recover spots of slow rotators are required. Possible methods are planetary eclipse mapping and the combination of lightcurves and RV curves. Kepler and CoRoT should provide at least a few candidates where this is feasible.

6 DI of targets can be significantly improved when combining it with additional simultaneous information, e.g., (multi-band) lightcurves. CoRoT and Kepler will certainly identify many objects worth imaging and obtain long-term photometry; therefore, contemporaneous DI of such objects would be advantageous.

7 DI of a transiting system – *planetary eclipse Doppler Imaging* – would be a novel technique. The line deformations caused by the planet during the transit could provide an extremely high resolution of spots on the eclipsed section and their precise localization.

8 The CoRoT mission offers the possibility to use multi-band photometry, which is of high interest for starspot analysis. It would provide additional temperature information on a star's surface. Although there seem to be significant technical problems with the three color channels, the applicability of using this multi-band information should be explored and its advantages taken.

7.4.2 Extra-solar planets

1 The Rossiter-McLaughlin effect of transiting planets uses the apparent shift of spectral lines due to their deformed profiles. This approach would be improved when the line profile deformations are modeled similar to the DI technique. However, it requires stars rotating fast enough to be Doppler imaged.

2 The detection of planets around active stars requires to understand and to remove spot signatures in lightcurves and RV measurements. This is important for highly active stars where even the detection of close-in Jupiter-mass planets is difficult, as well as for moderately active stars where the detection of small planets is complicated. Starspots should be modeled in lightcurves and RV curves with the goal of substantially reducing their signal. A promising approach is to use simultaneous high-precision lightcurves, reconstruct the surface distribution, use it to calculate the expected RV variations, and subtract this model from the high-precision RV measurements. A success would immensely increase the chance to detect planets that never would have been found before.

3 A precise determination of planetary parameters around active stars requires the consideration of starspots. Ignoring them likely leads to wrong planetary parameters, e.g., the radius. Although a significant removal of starspot signatures might not be possible in some cases, the consideration of activity will result in a much higher – and more realistic – error estimate for planetary parameters than just the regular statistical error of standard fitting routines. Some planets found by the CoRoT mission orbit around active stars and in most cases the influence of starspots has been ignored. In RV measurements of active stars, especially when the Rossiter-McLaughlin effect is observed, activity is usually not modeled or corrected for. However, a successful modeling and removal of starspots in RV measurements would certainly improve the precision of determined planetary parameters. This approach should be tried out with some of the many available high-precision radial velocity curves.

Acknowledgments

> *“Nullum enim officium referenda gratia magis necessarium est.”*
>
> *“There is no duty more obligatory than the repayment of kindness.”*
>
> *“Keine Schuld ist dringender, als die, Dank zu sagen.”*

Marcus Tullius Cicero
Quote from his essay *De Officiis*
Book I., 15, 47-, 44 BC

For those I really have to thank so much, I switch back to German language.

Für all diejenigen, denen ich so sehr zu Dank verpflichtet bin, verfasse ich diese Zeilen in deutscher Sprache. Ich bin überwältigt von der Vielzahl von Menschen, die mir während dieser Doktorarbeit, und auch auf dem Weg dorthin, mit Rat und Tat zur Seite gestanden haben. Im einzelnen möchte ich mich ganz besonders bedanken bei

- meinen Eltern **Felix und Elisabeth Huber**, deren liebevolle und unendliche Unterstützung es mir überhaupt erst ermöglicht hat diesen Weg zu gehen.
- meiner gesamten **Familie** für ihr Interesse und ihre Ermutigung; besonders bei meiner Schwester **Ulrike** und meinem Bruder **Thomas**, und meiner hamburgischen ‘Ersatzfamilie’ **Achim** und **Gisi Priebe**.
- meinem Doktorvater Professor **Jürgen Schmitt**, für seine hervorragende Betreuung, die Freiheit mich zwanglos und kreativ zu entfalten, sein Vertrauen und seine Bestätigung.
- meinem Betreuer und Kollegen **Uwe Wolter**, dessen Faszination für sein Gebiet mich angesteckt und beflügelt hat, und von dessen Zusammenarbeit und Fachkenntnis ich immens profitieren konnte.
- meinem Kollegen und Freund **Stefan Czesla**, ohne dessen unzählige Hilfestellungen, Kommentare, Ideen und Diskussionen, ohne dessen Mitarbeit und Eigeninitiative, viele Fortschritte und Ergebnisse nicht realisierbar gewesen wären.
- meinen Freunden, die es auch in schwierigen Zeiten immer wieder geschafft haben mich aufzurichten.

Selbstverständlich bedanke ich mich auch bei der Universität Hamburg und der Sternwarte Hamburg für die Möglichkeit meine Doktorarbeit im Rahmen des Graduiertenkollegs 1351 *Extrasolar Planets and their Host Stars* schreiben zu können, und für die damit verbundene Unterstützung durch die Deutsche Forschungsgesellschaft (DFG).

List of Figures

1.1 Sunspot maps drawn by Scheiner in his book *Tres Epistolae* (Scheiner 1612). 14

1.2 Sunspot maps drawn by Scheiner in his book *Rosa Ursina* (Scheiner 1626). 14

1.6 Variations of the total irradiance of the Sun (black curve). The electromagnetic radiation per unit area W/m^2 is given over years. This picture is part of the public domain. 15

1.3 Butterfly diagram of the Sun. The vertical axis gives the latitude of the spots. Larger spots have lighter color. This picture is part of the *public domain*. . 15

1.4 The biggest sunspots observed in the 20th century. Spot sizes are often measured by their area compared to the total area of the solar disk, which is the unit of the vertical axis. The largest spot was observed in the year 1947. This picture was taken from `http://spaceweather.com/sunspots/history.html`. 16

1.5 Solar differential rotation from Beck (2000). *Left panel:* Different measurements using the Doppler shift of photospheric spectral lines. *Right panel:* Different measurements using tracers (sunspots, magnetograms, supergranules). 17

1.7 Size distribution of a total number of 24 615 sunspots taken from Bogdan et al. (1988). Smaller spots are much more frequent than larger ones 18

1.8 *Upper panel:* Largest group of sunspots yet observed with SOHO in March 2001. *Lower panel:* Huge loop of plasma caught in magnetic field lines. This prominence was observed at 14th September, 1999. Both pictures are taken from the SOHO homepage at `http://sohowww.nascom.nasa.gov/gallery/bestofsoho.html`. 20

1.9 Magnetogram of the solar surface observed with the Michelson Doppler Imager on board of the SOHO satellite. The black and white structures show magnetic fields with opposite polarization. The picture is taken from the SOHO homepage at `http://sohowww.nascom.nasa.gov/gallery/bestofsoho.html`. . 21

1.10 Tilt angle of bipolar spots on the Sun (Howard 1991). Shown is the angle between the line connecting the centers of the bipolar spot and the equator. 22

1.11 Tilt angle of bipolar spots on the Sun versus latitude (Howard 1991). Low-latitude spots have smaller tilts than spots closer to the poles. 22

1.12 The magnetic butterfly diagram of the Sun. The field strength is color coded, blue and yellow colors indicate the two different polarities of the magnetic field. Every solar cycle the polarity of the poles switches. The polarity of neighboring spots can be opposite. This picture was taken from `http://solarscience.msfc.nasa.gov/dynamo.shtml`. 23

1.13 Sketch of the transformation of the poloidal magnetic field (panel a) to the toroidal field (panel b) by differential rotation (Choudhuri 2007). This mechanism is called the Ω-effect in dynamo theory. 26

1.14 Interior rotation rate of the Sun over radius and latitude (Schou et al. 1998). Shown are solutions for four different inversion methods of the used helioseismic data. The dashed line indicates the position of the tachocline. 26

1.15 Sketch from Parker (1955b) showing the toroidal magnetic field lines rising in the convection zone and penetrating the surface. *Panel a:* Magnetic buoyancy. *Panel b:* Concentration of field lines. *Panel c:* Splitting of flux tubes. . . . 26

1.16 Illustration of the α-effect (Parker 1970). Uprising (toroidal) flux tubes get twisted by the Coriolis force and build up the poloidal magnetic field. . . . 27

2.1 Activity-rotation relation from chromospheric emission (Mamajek & Hillenbrand 2008). A larger CaII H and K emission index R_{HK} indicates higher chromospheric activity. A smaller Rossby Number R_0 indicates shorter rotation periods of the star. The data show the clear increase of activity with faster rotation. 30

2.2 Activity-rotation relation from coronal emission (Mamajek & Hillenbrand 2008). The X-ray emission R_X indicates coronal activity. Stars with higher Rossby Numbers also show higher activity. 31

2.3 Simulated transit profiles of CoRoT-2 b deformed by the occultation of a spot. The red curve shows the signature of a spot with radius $R_{\mathrm{sp}} = 8°$, the black curve presents the calculation for $R_{\mathrm{sp}} = 15°$. Both curves are normalized to a continuum of unity. The dashed vertical lines indicate that the radii of the spot R_{sp} and the planet R_{P} can be determined from the bump in the transit profile; this is only illustrated for the black curve (large spot). 33

2.4 Simulated lightcurve of CoRoT-2 with one spot at 180° longitude and a radius of $R_{\mathrm{sp}} = 15°$. To illustrate the effect of the different longitudinal positions of the spot during the stellar rotation on the transit profiles of the planet CoRoT-2 b, transits for an orbital rotation period of $P_{\mathrm{P}} = P_{\mathrm{Star}}/10$ are calculated. The upper panel shows the entire lightcurve, the lower panels show close-ups of six individual transits. The series of transits visualizes nicely how the deformation caused by the spot moves through the profile. 34

2.5 Activity-induced RV variations due to spots. The red curve illustrates one spot the size of 0.5 % of the stellar disk, the black line is for one spot size of 0.1 %. The used stellar parameters are that of CoRoT-2 ($v \sin(i) = 12$ km/s). 35

2.6 Values of Table 2.1 including a linear regression. This graph illustrates the relation between the amplitude K of the activity-induced RV variations and properties of the spot and the star; T_{sp} and T_{ph} are the temperatures of spot and undisturbed photosphere, A_{sp} and A_{disk} are the areas of spot and stellar disk, and $v \sin(i)$ is the projected rotation velocity of the star. 35

2.7 Simulation of the reconstruction of latitudinal positions of two spots (upper and lower panel). The black arrows indicate the correct value. The red bars show the reconstructed value from only lightcurve inversion, the green bars from only RV curve inversion, and the blue bars for a combined fit. 37

2.8 Simulation of the Rossiter-McLaughlin effect for CoRoT-2 b. The red curve illustrates the effect if no spots are on the eclipsed section, the black line shows what effect spots have on the shape of the curve. One spot with a size of 0.5 % of the disk is located at 300° longitude, the other one with 0.1 % size is placed at 30° longitude. The planet crosses the disk at stellar phase zero. An asymmetric distribution of starspots shifts the entire RV curve; thus, the black curve was corrected by adding a constant RV value of 35 m/s. 37

2.9 Deformation of a spectral line by a dark spot, as employed by Doppler Imaging (Vogt & Penrod 1983). The spot appears as a bump in the line profile. With rotation this bump moves through the profile. 38

2.10 Temperature difference between starspots and the undisturbed photosphere (Berdyugina 2005). Squares symbolize active giants, circles stand for active dwarfs. Thin lines connect different measurements of the same star. The two dots within circles roughly indicate umbral and penumbral values of the Sun. 40

2.11 Differential rotation $\Delta\Omega$ over surface temperature for a sample of 10 stars of spectral types G2 to M2 (Barnes et al. 2005). A stronger differential rotation with increasing temperature is indicated. The Sun represented by the circle does not obey this correlation. 43

2.12 Butterfly diagram of HR 1099 (Berdyugina & Henry 2007). Shown are mean latitudes reconstructed for two large spots in separate active longitudes (panel a and b). Different symbols indicate different reconstruction techniques. . . 44

3.1 Picture of β Pictoris in near-infrared taken with the ESO 3.6 m telescope (outer part) and with the VLT (inner part). It shows an edge-on view onto the circumstellar disk and the inner planet candidate β Pic b (Lagrange et al. 2009). The picture is taken from `http://www.eso.org/public/images/eso0842a/`. 46

3.2 Radial velocity measurements of 51 Peg (Mayor & Queloz 1995). The dots are the measurements with errors, the continuous line is the model for a $\mathrm{M}\sin(i) = 0.468\ \mathrm{M}_{\mathrm{Jupiter}}$ companion with a period of about $P = 4.2$ days. 46

3.3 Mass distribution of extra-solar planets and brown dwarfs (Hatzes 2010). The number of detected exoplanets is much higher than that of brown dwarfs. The 'brown dwarf desert' is marked, indicating that these objects either are not found or exist only occasionally. 47

3.4 The number of extra-solar planets over stellar mass taken from the 'Extrasolar Planets Encyclopedia' (`http://exoplanet.eu`). Most planets are found around late-type stars. This distribution reveals a bias introduced by planet detection techniques (see Sect. 3.3). 48
3.5 Definition of the angle λ (Ohta et al. 2005). It is the projected angle between the orbital inclination of the planet and the stellar inclination. 49
3.6 Measurement of the Rossiter-McLaughlin effect for CoRoT-2 (Bouchy et al. 2008) with the spectrographs SOPHIE (dots) and HARPS (circles). The continuous dark line is the best model indicating $\lambda = 7.2 \pm 4.5$ deg. 49
3.7 Transit of the planet HD 209458 b (Charbonneau et al. 2000). It was the first planet ever observed with the transit method. The continuous line indicates the best model referring to a planet of $\mathrm{M} = 0.685\ \mathrm{M}_{\mathrm{Jupiter}}$ and an orbital period of $P = 3.5$ days. 50
3.8 Lightcurve of the active star Corot-7 (upper panel) and the phase-folded transit of Corot-7 b (lower panel) with a drop in brightness of only about $3{\cdot}10^{-4}$ (Léger et al. 2009). 51
3.9 Transit of Kepler-4 b illustrating the high-precision of the Kepler photometry (Borucki et al. 2010). 51
3.10 Lightcurve of the previously detected transiting planet HAT-P7 b observed with Kepler (Borucki et al. 2009). The high precision does not only allow to detect the planet's transit, but also the secondary transit and the modulation of the lightcurve due to the planet's reflection of starlight can be seen. . . . 52
3.11 The number of of extra-solar planets plotted over the year of discovery taken from the 'Extrasolar Planets Encyclopedia' (`http://exoplanet.eu`). The detection rate of planets increases rapidly. 52

7.1 Brightness maps of CoRoT-2 showing the temporal evolution of the surface. *Upper panel*: Map reconstructed from the global lightcurve (noneclipsed surface). *Lower panel*: Map for the reconstructions of the transits (eclipsed surface). Each step in transit number equals a time step of 1.74 days. For further information see the publication in Sect. 6.3. 107

List of Tables

2.1 Illustration of the influence of spots on lightcurves and RV measurements for some selected stars. The columns give the projected rotation velocity $v\sin(i)$, the effective temperature of the star $T_\star$ and the spot $T_\bullet$, the ratio between spot and disk area $A_\bullet/A_{\mathrm{disk}}$, the RV amplitude K caused by the spot, and the rotation period of the star P. Note that $A_\bullet/A_{\mathrm{disk}} \approx \Delta I/I$ for spots with low temperature ($T_\bullet^4/T_\star^4 \ll 1$). 36

3.1 Table of detection requirements and probabilities of the transit method for a selected sample of objects. Quantity $\Delta I/I$ is the drop in observed brightness during a transit, p(transit) is the probability that the orbital plane is viewed edge-on so that a transit occurs, N is the number of stars that has to be observed to find such a planet if *all* stars had one, t is the transit duration, and P is the orbital period. Additionally, the amplitude K of the planet is given that would have to be measured in radial velocities to find it. The CoRoT mission reaches precisions of about 10^{-4} in $\Delta I/I$, Kepler of about 10^{-5}. High-precision RV measurements deliver accuracies of below 1 m/s. . 53

Bibliography

Alfvén, H. 1943, Arkiv for Astronomi, 29, 1

Babcock, H. W. 1961, Astrophysical Journal, 133, 572

Baliunas, S. L., Donahue, R. A., Soon, W. H., et al. 1995, Astrophysical Journal, 438, 269

Barnes, J. R. 2005, Monthly Notices of the Royal Astronomical Society, 364, 137

Barnes, J. R., Cameron, A. C., Donati, J., et al. 2005, Monthly Notices of the Royal Astronomical Society, 357, L1

Beck, J. G. 2000, Solar Physics, 191, 47

Beck, J. G. & Chapman, G. A. 1993, Solar Physics, 146, 49

Berdyugina, S. V. 2005, Living Reviews in Solar Physics, 2, 8

Berdyugina, S. V. & Henry, G. W. 2007, Astrophysical Journal, 659, L157

Berdyugina, S. V., Pelt, J., & Tuominen, I. 2002, Astronomy and Astrophysics, 394, 505

Berdyugina, S. V. & Tuominen, I. 1998, Astronomy and Astrophysics, 336, L25

Bogdan, T. J., Gilman, P. A., Lerche, I., & Howard, R. 1988, Astrophysical Journal, 327, 451

Bopp, B. W. & Evans, D. S. 1973, Monthly Notices of the Royal Astronomical Society, 164, 343

Borucki, W. J., Koch, D., Jenkins, J., et al. 2009, Science, 325, 709

Borucki, W. J., Koch, D. G., Brown, T. M., et al. 2010, Astrophysical Journal Letters, 713, L126

Bouchy, F., Queloz, D., Deleuil, M., et al. 2008, Astronomy and Astrophysics, 482, L25

Bray, R. J. & Loughhead, R. E. 1964, Sunspots, ed. Bray, R. J. & Loughhead, R. E.

Bruls, J. H. M. J., Schüssler, M., & Solanki, S. K. 1999, in Astronomical Society of the Pacific Conference Series, Vol. 158, Solar and Stellar Activity: Similarities and Differences, ed. C. J. Butler & J. G. Doyle, 182–+

Butler, R. P., Marcy, G. W., Williams, E., et al. 1996, Publications of the Astronomical Society of the Pacific, 108, 500

Carrington, R. C. 1858, MNRAS, 19, 1

Carrington, R. C. 1859, MNRAS, 19, 81

Chapman, G. A., Cookson, A. M., & Dobias, J. J. 1994, Astrophysical Journal, 432, 403

Charbonneau, D., Brown, T. M., Latham, D. W., & Mayor, M. 2000, Astrophysical Journal Letters, 529, L45

Choudhuri, A. R. 1998, The physics of fluids and plasmas : an introduction for astrophysicists /, ed. Choudhuri, A. R.

Choudhuri, A. R. 2007, in American Institute of Physics Conference Series, Vol. 919, Kodai School on Solar Physics, ed. S. S. Hasan & D. Banerjee, 49–73

Christensen-Dalsgaard, J. 2000, in Astronomical Society of the Pacific Conference Series, Vol. 210, Delta Scuti and Related Stars, ed. M. Breger & M. Montgomery, 187–+

Chugainov, P. F. 1966, Information Bulletin on Variable Stars, 172, 1

Cowling, T. G. 1934, Monthly Notices of the Royal Astronomical Society, 94, 768

Czesla, S., Huber, K. F., Wolter, U., Schröter, S., & Schmitt, J. H. M. M. 2009, Astronomy and Astrophysics, 505, 1277

Deutsch, A. J. 1958, in IAU Symposium, Vol. 6, Electromagnetic Phenomena in Cosmical Physics, ed. B. Lehnert, 209–+

Donati, J., Cameron, A. C., Semel, M., et al. 2003, Monthly Notices of the Royal Astronomical Society, 345, 1145

Donati, J., Semel, M., & Praderie, F. 1989, Astronomy and Astrophysics, 225, 467

Eddy, J. A., Gilman, P. A., & Trotter, D. E. 1976, Solar Physics, 46, 3

Fabricius, J. 1611, Narratio de maculis in sole observatis et apparente earum cum sole conversione, ed. I. I. B. Senioris & E. Rehifeldii (Wittenbergae)

Galilei, G. 1613, Istoria e Dimostrazioni Intorno Alle Macchie Solari e Loro Accidenti Rome

Gnevyshev, M. N. 1938, Izvestiya Glavnoj Astronomicheskoj Observatorii v Pulkove, 16, 36

Goncharskii, A. V., Stepanov, V. V., Kokhlova, V. L., & Yagola, A. G. 1977, Soviet Astronomy Letters, 3, 147

Gray, D. F. & Johanson, H. L. 1991, Publications of the Astronomical Society of the Pacific, 103, 439

Hale, G. E. 1908, Astrophysical Journal, 28, 315

Hale, G. E., Ellerman, F., Nicholson, S. B., & Joy, A. H. 1919, Astrophysical Journal, 49, 153

Hall, D. S. 1972, Publications of the Astronomical Society of the Pacific, 84, 323

Hall, D. S. 1996, in IAU Symposium, Vol. 176, Stellar Surface Structure, ed. K. G. Strassmeier & J. L. Linsky, 217–+

Hall, D. S. & Henry, G. W. 1994, International Amateur-Professional Photoelectric Photometry Communications, 55, 51

Hatzes, A. 2010, lectures on extra-solar planets at the Hamburger Sternwarte

Hatzes, A. P. 1995, Astrophysical Journal, 451, 784

Hatzes, A. P. 2002, Astronomische Nachrichten, 323, 392

Hempelmann, A., Schmitt, J. H. M. M., Schultz, M., Ruediger, G., & Stepien, K. 1995, Astronomy and Astrophysics, 294, 515

Henry, G. W., Marcy, G., Butler, R. P., & Vogt, S. S. 1999, IAU Circ., 7307, 1

Henry, G. W., Marcy, G. W., Butler, R. P., & Vogt, S. S. 2000, Astrophysical Journal Letters, 529, L41

Hoffmeister, C. 1965, Veroeffentlichungen der Sternwarte Sonneberg, 6, 97

Holzwarth, V., Mackay, D. H., & Jardine, M. 2006, Monthly Notices of the Royal Astronomical Society, 369, 1703

Howard, R. F. 1991, Solar Physics, 136, 251

Huber, K. F., Czesla, S., Wolter, U., & Schmitt, J. H. M. M. 2009a, Astronomy and Astrophysics, 508, 901

Huber, K. F., Czesla, S., Wolter, U., & Schmitt, J. H. M. M. 2010, ArXiv e-prints

Huber, K. F., Wolter, U., Czesla, S., et al. 2009b, Astronomy and Astrophysics, 501, 715

Huygens, C. 1698, Cosmotheoros. The Celestial Worlds Discover'd Or, Conjectures Concerning The Inhabitants, Plants AND Productions Of The Worlds In The Planets, (Timothy Childe), 159–150

Jeffers, S. V., Cameron, A. C., Barnes, J. R., & Aufdenberg, J. P. 2006, Astrophysics and Space Science, 304, 371

Jetsu, L., Pelt, J., & Tuominen, I. 1993, Astronomy and Astrophysics, 278, 449

Jetsu, L., Pelt, J., Tuominen, I., & Nations, H. 1991, in Lecture Notes in Physics, Berlin Springer Verlag, Vol. 380, IAU Colloq. 130: The Sun and Cool Stars. Activity, Magnetism, Dynamos, ed. I. Tuominen, D. Moss, & G. Rüdiger, 381–+

Katsova, M. M., Livshits, M. A., & Belvedere, G. 2003, Solar Physics, 216, 353

Kron, G. E. 1947, Publications of the Astronomical Society of the Pacific, 59, 261

Kürster, M. 1993, Astronomy and Astrophysics, 274, 851

Kürster, M., Schmitt, J. H. M. M., & Cutispoto, G. 1994, Astronomy and Astrophysics, 289, 899

Kurucz, R. L. 1992, Revista Mexicana de Astronomia y Astrofisica, vol. 23, 23, 181

Lagrange, A., Gratadour, D., Chauvin, G., et al. 2009, Astronomy and Astrophysics, 493, L21

Latham, D. W., Stefanik, R. P., Mazeh, T., Mayor, M., & Burki, G. 1989, Nature, 339, 38

Léger, A., Rouan, D., Schneider, J., et al. 2009, Astronomy and Astrophysics, 506, 287

Leigh, C., Cameron, A. C., Horne, K., Penny, A., & James, D. 2003, Monthly Notices of the Royal Astronomical Society, 344, 1271

Leighton, R. B. 1969, Astrophysical Journal, 156, 1

Linsky, J. 2007, lectures on stellar activity at the Hamburger Sternwarte

Livshits, M. A., Alekseev, I. Y., & Katsova, M. M. 2003, Astronomy Reports, 47, 562

Mamajek, E. E. & Hillenbrand, L. A. 2008, Astrophysical Journal, 687, 1264

Marcy, G. W. & Butler, R. P. 1992, Publications of the Astronomical Society of the Pacific, 104, 270

Marsden, S. C., Donati, J., Semel, M., Petit, P., & Carter, B. D. 2006, Monthly Notices of the Royal Astronomical Society, 370, 468

Mayor, M. & Queloz, D. 1995, Nature, 378, 355

McLaughlin, D. B. 1924, Astrophysical Journal, 60, 22

Messina, S. & Guinan, E. F. 2003, Astronomy and Astrophysics, 409, 1017

Mestel, L. 1999, Stellar magnetism, ed. Mestel, L.

Noyes, R. W., Hartmann, L. W., Baliunas, S. L., Duncan, D. K., & Vaughan, A. H. 1984, Astrophysical Journal, 279, 763

Ohta, Y., Taruya, A., & Suto, Y. 2005, Astrophysical Journal, 622, 1118

Oláh, K., Kolláth, Z., Granzer, T., et al. 2009, Astronomy and Astrophysics, 501, 703

O'Neal, D., Neff, J. E., Saar, S. H., & Mines, J. K. 2001, Astrophysical Journal, 122, 1954

O'Neal, D., Saar, S. H., & Neff, J. E. 1996, Astrophysical Journal, 463, 766

Parker, E. N. 1955a, Astrophysical Journal, 122, 293

Parker, E. N. 1955b, Astrophysical Journal, 121, 491

Parker, E. N. 1970, Astrophysical Journal, 162, 665

Petrovay, K. & van Driel-Gesztelyi, L. 1997, Solar Physics, 176, 249

Piskunov, N. E. 1991, in Lecture Notes in Physics, Berlin Springer Verlag, Vol. 380, IAU Colloq. 130: The Sun and Cool Stars. Activity, Magnetism, Dynamos, ed. I. Tuominen, D. Moss, & G. Rüdiger, 309–+

Piskunov, N. E., Tuominen, I., & Vilhu, O. 1990, Astronomy and Astrophysics, 230, 363

Poe, C. H. & Eaton, J. A. 1985, Astrophysical Journal, 289, 644

Pont, F., Gilliland, R. L., Moutou, C., et al. 2007, Astronomy and Astrophysics, 476, 1347

Queloz, D., Eggenberger, A., Mayor, M., et al. 2000, Astronomy and Astrophysics, 359, L13

Rabus, M., Alonso, R., Belmonte, J. A., et al. 2009, Astronomy and Astrophysics, 494, 391

Reiners, A., Bean, J. L., Huber, K. F., et al. 2010, Astrophysical Journal, 710, 432

Reiners, A. & Schmitt, J. H. M. M. 2003a, Astronomy and Astrophysics, 412, 813

Reiners, A. & Schmitt, J. H. M. M. 2003b, Astronomy and Astrophysics, 398, 647

Rice, J. B. 2002, Astronomische Nachrichten, 323, 220

Rice, J. B., Wehlau, W. H., & Khokhlova, V. L. 1989, Astronomy and Astrophysics, 208, 179

Rodono, M., Lanza, A. F., & Catalano, S. 1995, Astronomy and Astrophysics, 301, 75

Rossiter, R. A. 1924, Astrophysical Journal, 60, 15

Saar, S. H. & Donahue, R. A. 1997, Astrophysical Journal, 485, 319

Scheiner, C. 1612, Tres Epistolae de Maculis Solaribus Scriptae ad Marcum Welserum

Scheiner, C. 1626, Rosa Ursina, sive Sol ex admirando facularum et macularum suarum phoenomenon varius necnon circa centrum suum et axem fixum ab occasu in ortum annua, circaque alium axem mobilem ab ortu in occasum conversione quasi menstrua, super polos proprios libris quatuor mobilis ostensus (Bracciani : apud Andream Phaeum)

Schou, J., Antia, H. M., Basu, S., et al. 1998, Astrophysical Journal, 505, 390

Schrijver, C. J. & Title, A. M. 2001, Astrophysical Journal, 551, 1099

Schüssler, M. & Solanki, S. K. 1992, Astronomy and Astrophysics, 264, L13

Semel, M. 1989, Astronomy and Astrophysics, 225, 456

Simon, T., Ayres, T. R., Redfield, S., & Linsky, J. L. 2002, Astrophysical Journal, 579, 800

Smith, B. A. & Terrile, R. J. 1984, Science, 226, 1421

Snodgrass, H. B. & Ulrich, R. K. 1990, Astrophysical Journal, 351, 309

Solanki, S. K. 2003, Astronomy and Astrophysics Review, 11, 153

Solanki, S. K. & Unruh, Y. C. 2004, Monthly Notices of the Royal Astronomical Society, 348, 307

Strassmeier, K. G. 1999, Astronomy and Astrophysics, 347, 225

Strassmeier, K. G. 2009, The Astronomy and Astrophysics Review, 17, 251

Strassmeier, K. G., Bartus, J., Cutispoto, G., & Rodono, M. 1997, Astronomy and Astrophysics Supplement Series, 125, 11

Strassmeier, K. G., Hall, D. S., & Henry, G. W. 1994, Astronomy and Astrophysics, 282, 535

Strassmeier, K. G. & Rice, J. B. 1998, Astronomy and Astrophysics, 330, 685

Strassmeier, K. G. & Rice, J. B. 2003, Astronomy and Astrophysics, 399, 315

Torres, C. A. O. & Ferraz Mello, S. 1973, Astronomy and Astrophysics, 27, 231

Vincent, A., Piskunov, N. E., & Tuominen, I. 1993, Astronomy and Astrophysics, 278, 523

Vogt, S. S., Hatzes, A. P., Misch, A. A., & Kürster, M. 1999, The Astrophysical Journal Supplement Series, 121, 547

Vogt, S. S. & Penrod, G. D. 1983, Publications of the Astronomical Society of the Pacific, 95, 565

Vogt, S. S., Penrod, G. D., & Hatzes, A. P. 1987, Astrophysical Journal, 321, 496

Waldmeier, M. 1955, Ergebnisse und Probleme der Sonnenforschung., ed. Waldmeier, M.

Weiss, N. O. 1981, Journal of Geophysical Research, 86, 11689

Wilson, E. R. 1917, Popular Astronomy, 25, 88

Wolszczan, A. & Frail, D. A. 1992, Nature, 355, 145

Wolter, U., Schmitt, J. H. M. M., Huber, K. F., et al. 2009, Astronomy and Astrophysics, 504, 561

Wolter, U., Schmitt, J. H. M. M., & van Wyk, F. 2005, Astronomy and Astrophysics, 435, 261

Zappala, R. A. & Zuccarello, F. 1991, Astronomy and Astrophysics, 242, 480